A Finite Element Analysis of Elastic-Plastic Sliding of Hemispherical Contacts

A thesis
Presented to
The Academic Faculty

By

John Moody

In Partial Fulfillment
Of the Requirements for the Degree
Master of Science in Mechanical Engineering

Georgia Institute of Technology

August 2007

A Finite Element Analysis of Elastic-Plastic Sliding of Hemispherical Contacts

Approved by:

Dr. Itzhak Green, Advisor
G. W. W. School of Mechanical Engineering
Georgia Institute of Technology

Dr. Richard Neu
G. W. W. School of Mechanical Engineering
Georgia Institute of Technology

Dr. Jeffrey Streator
G. W. W. School of Mechanical Engineering
Georgia Institute of Technology

Date Approved:

ACKNOLEDGEMENTS

I am grateful to Dr. Itzhak Green for his unstinting support and guidance throughout my stay at Georgia Tech. I am also thankful to the graduate students in the Tribology research group for all their help. Last but not least, I would like to thank my wife, Katherine Moody, for her unending support in this endeavor.

This research is supported in part through the Department of Defense Multidisciplinary Research Program of the University Research Initiative as Office of Naval Research Grant N00014-04-1-0601, entitled "Friction & Wear under Very High Electromagnetic Stress." Dr. P. Peter Schmidt serves as Program Officer. Information conveyed in this manuscript does not necessarily reflect the position or policy of the Government, and no official endorsement should be inferred.

TABLE OF CONTENTS

LIST OF TABLES

LIST OF FIGURES

SUMMARY

This work presents a three dimensional (3D) elastic-plastic model for two hemispherical bodies sliding across each other under various preset vertical interferences with both no imposed friction coefficient imposed and a coefficient of 0.3 imposed. In particular, steel-on-steel and aluminum-on-copper contact situations are investigated. A finite element analysis (FEA) is used for the model and the results to investigate include stresses, deformations, contact areas, and energy loss in sliding. This analysis indicates that these results are dependent on not only the interference, but also on the materials involved. The model presented here has been normalized in order to apply to both macro and micro scale geometries. Hence, the results may be applied to macro contacts such as rolling element bearings and micro contacts such as interfering asperities in sliding. The FEA provides trends in the deformations, reaction forces, stresses, and net energy losses as a function of sliding distance. All these results are found to be related to the magnitude of vertical interference. Contour plots of the von Mises stresses are presented to show the formation and distribution of stresses with increasing plastic deformation as sliding progresses. This work also presents empirical equations that relate the net energy loss during sliding and the residual deformations, both as a function of the preset interference. The values of the contact area are obtained for different vertical interferences as sliding progresses.

CHAPTER I: INTRODUCTION

This work presents results from a three dimensional (3D) finite element analysis (FEA) of an elastic-plastic asperity contact model for two hemispherical bodies sliding across each other with various preset vertical interferences. Sliding contact is an important phenomenon in both the macro and micro scales. In the macro scale, it is important to consider friction, wear, and residual deformation that result when rough surfaces slide across one another as well as contact in situations such as rolling element bearings. In the micro scale, it is known that nominally smooth surfaces do indeed have undulations in their surface profile and the true area of contact is just a small fraction of the nominal area of contact. These high points, or asperities, are known to deform plastically during sliding. Three dimensional sliding of a pair of asperities provides the kernel of the solution for any stochastically distributed rough surface. Thus, it is important to know how the deformed geometry, residual stresses, and surface condition affect the sliding process between a pair of asperities. The model presented here has been normalized in order to apply the results to both macro and micro scale geometries.

There have been many works over the years dealing with elastic and elastic-plastic contact. Many works have analyzed the contact of rough surfaces as reviewed by Liu et al. [1]. These works are based on the contact behavior of a single asperity in a statistical model of multiple asperity contact. All of these works share the common methodology of Thomas [2] and Greenwood [3]. Some of these works are restricted to the elastic regime, such as the landmark work by Greenwood and Williamson [4]. Other works [5-9] extend the Greenwood and Williamson model in the elastic regime to a variety of geometries and different basic assumptions. While other works concentrate on

purely plastic deformation, and are based on the models of Abbott and Firestone [10] and Tsukizoe and Hisakado [8].

Normal spherical contacts are considered in the elastic-plastic regime by Evseev et al. [11], Chang [12], and Zhao [13]. FEA has been used by Vu-Quoc et al. [14] to analyze normal contact between two spheres, which by symmetry is equivalent to that of one sphere in contact with a rigid flat. Adams and Nosonovsky [15] provide a review of contact modeling with an emphasis on the forces of contact and their relationship to the geometrical, material, and mechanical properties of the contacting bodies. Recently, Jackson and Green [16], Wang and Keer [17], and Nelias et al. [18], have explored hemispherical elastic-plastic contact in a normal loading situation. However, the characteristics of normal contact as opposed to sliding contact are quite different, and thus the latter is explored in this work.

Though work has been done in the area of sliding spherical contact, in most cases either simplifying assumptions have ignored important phenomena or less than satisfactory results have been produced. There have been many works, mainly based on Green [19, 20], which analyzed friction and adhesion of triangular shaped contact geometries that have analyzed fully plastic contact interfaces taking into account the adhesion forces present. In reality though, the contact junctions are more realistically be modeled as spherical in shape. Faulkner and Arnell [21] present the first work that models sphere-on-sphere sliding contact using an FEA approach. No general results are presented in this work and the method resulted in extremely long execution times (over 960 hours).

Hertzian theory suggests an elliptical contact can be modeled as an equivalent sphere on a rigid flat. Such an equivalent model has no physical grounds or mathematical proof once plasticity takes place, certainly not when the two sliding bodies have distinct material properties. In this work, individual elastic-plastic hemispheres sliding over each other are treated, and not as a part of a statistically generated surface. Sliding is simulated by means of FEA wherein the two interfering bodies are both fully modeled, without resorting to the common model of an equivalent body against a flat. This is particularly important when sliding takes place between dissimilar materials. This work is then compared to a semi-analytical technique developed by Boucly et al [22].

In the elastic domain and up to the onset of plasticity, the Hertzian solution [23] is used to obtain critical values of load, contact half-width, and strain energy as defined in Green [24]. As explained in [24], hardness is not implemented as a unique material property as it varies with the deformation itself as well as with other material properties such as yield strength, Poisson's ratio, and the elastic modulus. Instead, the critical vertical interference, ω_c, as derived in [24] for hemispherical contact, is employed. This quantity is derived by using the distortion energy yield criterion at the site of maximum von Mises stress by comparing the stress value with the yield strength, S_y. The critical values of force, P_c, contact area, A_c, and interference, ω_c, are:

$$P_c = \frac{(\pi C S_y)^3 \mathrm{R}^2}{6E'^2} \;;\; A_c = \frac{\pi^3 \left(C S_y R\right)^2}{\left(2E'\right)^2} \;;\; \omega_c = \left(\frac{C S_y}{2E'}\right)^2 R \tag{1}$$

$$\frac{\sigma_e}{p_o} = \frac{1}{2}\sqrt{\frac{((1-2\nu-2\zeta^2(1+\nu)+2(\zeta+\zeta^3)(1+\nu)ArcCot\left[\zeta\right])^2}{(1+\zeta^2)^2}} \tag{2}$$

Where:

$$\frac{1}{R} = \frac{1}{R_1} + \frac{1}{R_2} \tag{3}$$

$$\frac{1}{E'} = \frac{1-\nu_1^{\,2}}{E_1} + \frac{1-\nu_2^{\,2}}{E_2} \tag{4}$$

$$\zeta_c = 0.38167 + 0.33136\nu \tag{5}$$

$$C = 1.30075 + 0.87825\nu + 0.54373\nu^2 \tag{6}$$

The value of ζ_c is the depth at which yielding first occurs, normalized by the contact radius. The product of CS_y to be used in Eq. (1) depends on which material yields first and is determined by:

$$CS_y = \min(CS_{y1}, CS_{y2}) \tag{7}$$

The value of C itself is obtained from elasticity considerations, and the critical parameters are obtained at the point of yielding onset. The maximum elastic energy that can possibly be stored (up to the point of yielding onset) is used to normalize the net energy loss due to plastic deformation after sliding, and is given by [24] as:

$$U_c = \frac{\pi\left(CS_y\right)^5 R^3}{60E'^4} \tag{8}$$

Since all the quantities are subsequently being normalized by the critical parameters in Eq. (1), the ensuing results apply for any geometry scale as long as continuum mechanics is assumed to prevail; therefore, the radii for the hemispheres in the FE model are subjectively chosen to be $R_1 = R_2 = 1m$.

This analysis considers both steel-on-steel and aluminum-on-copper contact. The critical values are calculated for a steel material with properties as follows: $\mathrm{E}_1 = \mathrm{E}_2 = 200\,\mathrm{GPa}$, $\nu_1 = \nu_2 = 0.32$, and $S_y = 0.9115\,\mathrm{GPa}$. This material has been tested by Jackson et al.[25], and its yield strength lies in the middle of the range of the five steel materials investigated in that work. The results obtained in this work are thus not representative of all steel materials, but only of that tested by Jackson et al.[25]. The aluminum-on-copper hemispheres are modeled by sliding of a Glidcop hemisphere (99.63% Cu, 0.16% Al, 0.0016% Fe, 0.0005% Pb, 0.020% B) over an Al 6061-T651 hemisphere (97.5% Al, 0.3% Cr, 0.15% Cu, 0.7% Fe, 0.8% Mg, 0.15% Mn, 0.4% Si). These particular materials are chosen for analysis because of their use in the EML under investigation. While the rail in the EML is made of Glidcop, the armature that serves to propel the projectile is an Aluminum alloy Al 6061-T651. Table 1 presents the material properties used in this analysis, and Table 2 presents the critical values calculated from the above equations. Table 3 presents the interferences for all the cases studied in this analysis for both steel-on-steel and aluminum-on-copper.

In this analysis the material is regarded as elastic-perfectly plastic, but in order to help convergence, a material model with a 2% strain hardening based on the elastic modulus is used. This small amount of strain hardening has been verified to not significantly affect the forthcoming results yet drastically improves upon convergence time.

Table 1: Material properties for the two hemispheres

Property	Steel	Aluminum	Copper
E	200 GPa	68.0 GPa	130 GPa
Sy	911.5	310 MPa	331 MPa
υ	0.32	0.326	0.33

Table 2: Critical values of parameters at the onset of plasticity for sliding between two hemispherical contacts

Parameter	Steel-on-Steel	Al-on-Cu*
CSy	1.493 GPa	509.9 MPa
ω_c	0.2214 mm	0.1261 mm
P_c	346.1 kN	67.32 kN
A_c	347.8 mm^2	198 mm^2
U_c	30.65 J	3.395 J

*Aluminum yields first

Table 3: The interferences for all cases presented in this analysis.

	Interference [m]					
ω^*	2	4	6	9	12	15
Steel-on-Steel	4.428E-04	8.856E-04	1.328E-03	1.993E-03	2.657E-03	3.321E-03
Aluminum-on-Copper	2.522E-04	5.044E-04	7.566E-04	1.135E-03	1.513E-03	1.892E-03

CHAPTER II: MODELING METHOD

Figure 1 shows a schematic representation of the sliding process. The modeling method is similar to the method presented to model cylinders in sliding in Vijaywargiya and Green [26]. In this analysis a displacement, Δx is applied to the top surface of the top hemisphere where the bottom surface of the bottom hemisphere is held stationary. This Δx represents the total horizontal sliding distance that a hemisphere must slide in order end in a single-point contact when starting from a single-point contact. The total sliding distance is calculated from geometry and it is a function of the vertical interference, ω, where Δx increases with the preset interference ω. That total distance is divided into n equal load steps, $\delta x = \Delta x / n$. Hence, at load step i the horizontal location of the center of the moving hemisphere relative to the center of the stationary hemisphere is:

$$x = i \cdot \delta x - \frac{\Delta x}{2}; \quad i = 0, n + m$$

Because of material tugging m load steps are added to ensure exit from sliding contact. Normalizing x by R, the loading phase is defined by the region $x/R<0$, where the top hemisphere is pressed horizontally against the bottom one before passing the vertical axis of alignment ($x/R=0$). The unloading phase is defined in the region $x/R>0$, where the top hemisphere has passed the vertical axis of alignment, and where the hemispheres are expected to repel each other, and ultimately disengage.

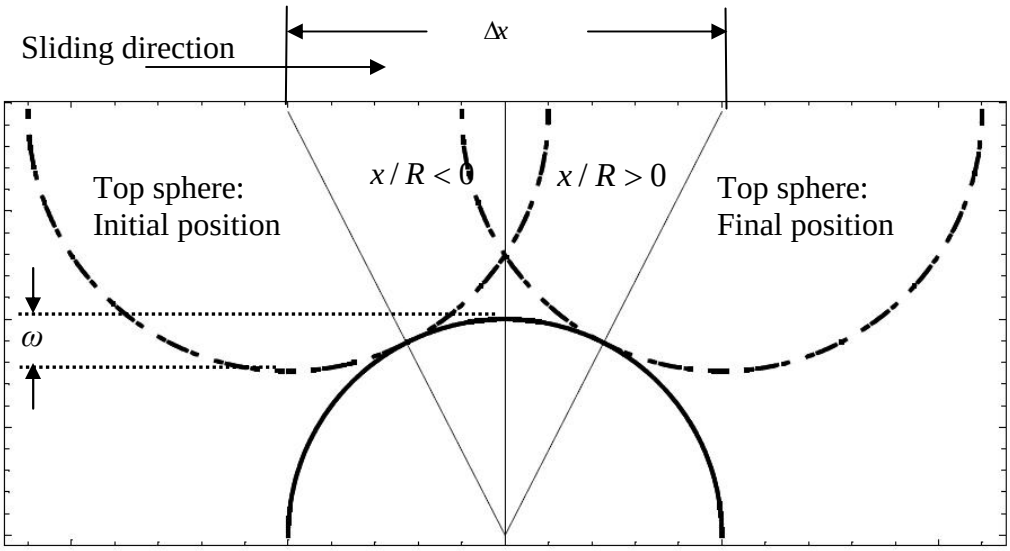

Figure 1: A schematic of the sliding process

Assumptions

Following are the assumptions that are used to simplify the problem:

1) At first sliding is assumed to be a frictionless process, and hence no coefficient of friction is input in the FE model. This is done in order to isolate the effect of plasticity during sliding. Subsequently this is relaxed and frictional sliding is investigated.
2) It is assumed that the mesh validated up to the onset of plasticity is also robust for analysis of the elastic-plastic regime, since no closed form solution is available beyond that point for this purpose.
3) Deformations in the bulk area are assumed not to have a significant bearing on the effects of sliding in the contact region. This work concentrates on the area close to the contact surfaces and far field bulk deformation effects are assumed not to have a significant effect on the region close to the contact surfaces.

4) Sliding is simulated as a quasi-static process, i.e., time-dependent phenomena are not analyzed. Hence, dynamic effects are ignored and material properties used do not depend on the strain rate. Likewise, adhesion and stick-slip phenomena are not accounted for.
5) Temperature effects that occur due to sliding are not considered, and the material properties used are assumed to be at room temperature.

This analysis is done using ABAQUS, a commercial FEA software package using linear brick (8-node) elements. A representative model is presented in Figure 2. In order to take advantage of the symmetry of the problem, each sphere is cut in half along the vertical plane. There is no displacement normal to this cut plane because the spheres are constrained to slide peak-over-peak. Therefore, a roller boundary condition is imposed along this vertically cut plane for both spheres. Also, an assumption is made, and later confirmed, that under the interferences considered here there is insignificant stress or deformation in areas far from the contact region (half-space assumption). This assumption is reasonable if one considers the fact that the contact half-width is much smaller than the radius of the sphere and as such, the stress distribution near the contact region cannot be strongly influenced by the conditions in the bulk of the material. This is also in agreement with the fact that deformations decay as $1/r$, where r is the distance from contact [23]. To take advantage of this each sphere is cut in half in the horizontal plane. A roller boundary condition is imposed along the top surface of the top hemisphere and the bottom surface of the bottom hemisphere is completely constrained. The end result is the hemisphere model shown in Figure 2(a).

In order to capture the deformations and stresses in the region near the contact, the mesh refinement scheme shown in Figure 2(b) is used. This high level of refinement yielded meshes with many elements. Each hemisphere consists of from about 20,000 to 50,000 elements, depending on the applied interference. As interference increases a finer mesh is generated in a larger volume near contact because higher stresses develop deeper into the hemispheres. Depending on the interference and with this many nodes and elements each simulation in this study takes from 2 days to over a week on a workstation computer with 8 GB of physical memory and a 2.6 GHz dual-core processor.

As discussed earlier, the total sliding distance is broken into n equal steps. This is done in order monitor the phenomena of interest as sliding progresses as well as to help convergence. Generally, the cases in this analysis are run with 40 equal load steps (n=40) with 4 steps added to the end for frictionless sliding and 8 steps added to the end for frictional sliding (m=4 or 8). However, for the higher interference steel-on-steel cases as many as 120 load steps are used. This is a trial-and-error process as the code will run, usually to just before or after the hemispheres are vertically aligned then a load step will fail to converge. The code can then be restarted at the last successful increment and continued with a smaller load step sizing.

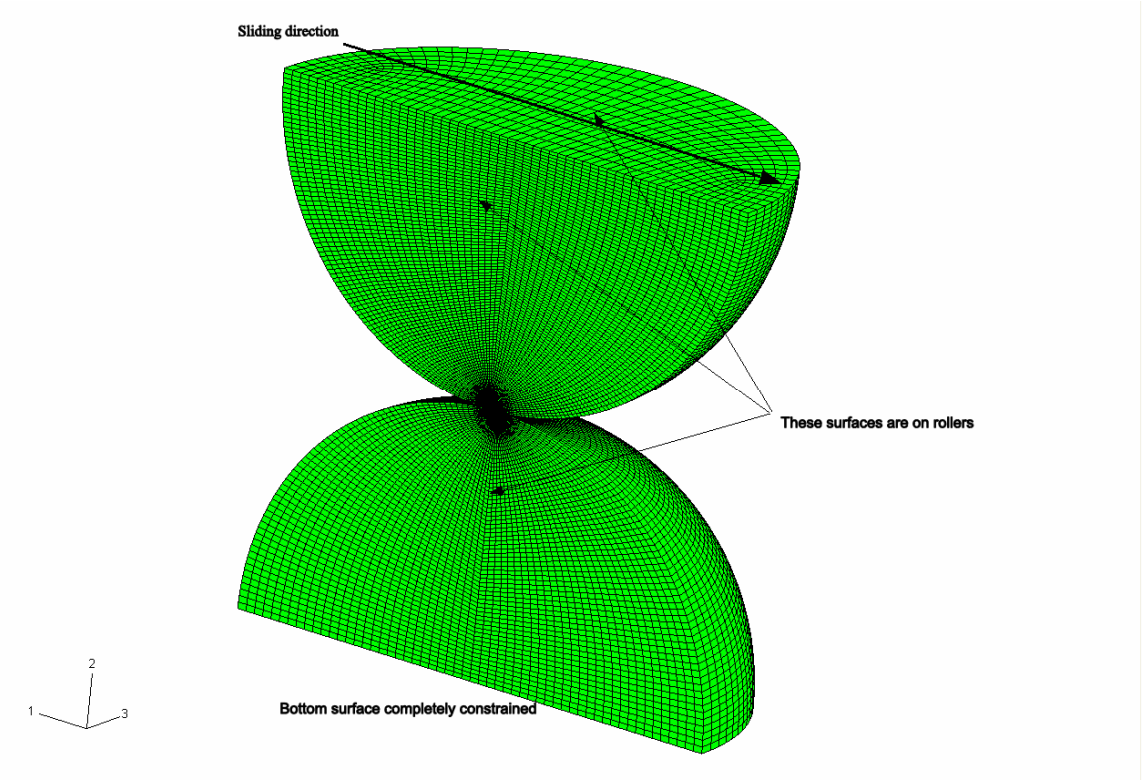

(a)

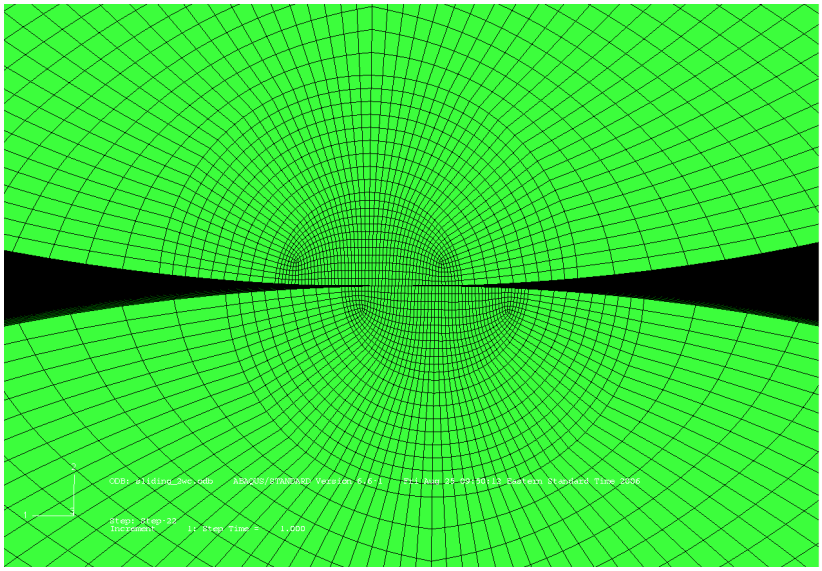

(b)

Figure 2: (a) Model geometry indicating the boundary conditions and sliding direction (b) a zoomed view of the contact region showing the mesh refinement

Mesh Convergence

The mesh is validated first for a vertically aligned normal elastic contact (non-sliding) with the properties for steel from Table 1 and results are compared against the analytical solution obtained by Green [24]. The FE model is then run past the elastic limit and compared to the results in Jackson and Green [27]. In this analysis, a downward displacement is applied to the top hemisphere and the load, P, is monitored. Table 4 presents the loads, normalized by P_c, for the models and FEA and the percent errors at a given downward displacement normalized by the critical displacement, ω_c, where both normalized values are from Eq. (1). As shown in Table 4, the theoretical and FEA values agree very well with a maximum percent error of 3.2% en the elastic regime and a maximum error of less than 2% for the plastic regime.

Table 4: Validation of the meshing scheme employed

ω^*	P^* Model	P^* FEA	% Error
0.2	0.089	0.087	-2.7
0.6	0.465	0.450	-3.2
1	1.000	0.989	-1.1
1.4	1.657	1.635	-1.3
1.8	2.415	2.377	-1.6
2.2	3.223	3.180	-1.3
2.6	4.075	4.012	-1.6
3	4.978	4.923	-1.1

Quadrilateral-faced and triangular-faced element meshes are compared. It is found that the quadrilateral-faced elements yields better results with a coarser mesh and are therefore used in order to reduce run time. Also, the results are compared to a semi-analytical method (SAM) as developed by Boucly [22] to validate the mesh. The FEA

results compare very well to the SAM results. A detailed comparison is presented later in a subsequent chapter.

Finally, results for frictionless steel-on-steel sliding contact with an interference equal to the critical interference are compared to the normal loading results presented above. The percent difference is 2.3% between the model results for normal loading at the critical interference and the sliding results when the hemispheres are vertically aligned. These two situations should be equivalent. This, coupled with the fact that the results for the sliding case are perfectly symmetric in the elastic regime, also suggest the results can be given in confidence.

CHAPTER III: RESULTS—FRICTIONLESS

3.1. Stresses

As part of this analysis, the stress profile throughout the progression of frictionless sliding is monitored. Figures 3 and 4 present the von Mises stress in the two hemispheres at the point of vertical alignment ($x/R = 0$) for preset vertical interferences of $2\omega_c$ and $15\omega_c$ for steel-on-steel and aluminum-on-copper sliding, respectively. The results are smooth and symmetric about the contact plane for the steel-on-steel case suggesting the mesh resolution is adequate. In order to show the stress pattern with adequate detail, each image is a close-up of the area near contact. It can be seen, based on the curvature, that the stressed volume penetrates deeper into the hemisphere for the $15\omega_c$ case while maximum values appear at the contact surface (see Figures 3(b) and 4(b)). For the $2\omega_c$ case, the hemispheres have deformed plastically, i.e. the stresses have surpassed their respective yield strength, yet the yielded regions still lie below the surface (see Figures 3(a) and 4(a)). In the aluminum-on-copper sliding with an interference of $15\omega_c$ both hemispheres show a large volume with more significant plastic flow compared to the steel-on-steel sliding case.

It can be seen in Figures 3 and 4 that the stress values are slightly above the yield strength. This is due to the strain hardening implemented in this analysis. As stated previously, strain hardening of 2% of the elastic modulus is added to the material definition in order to improve convergence.

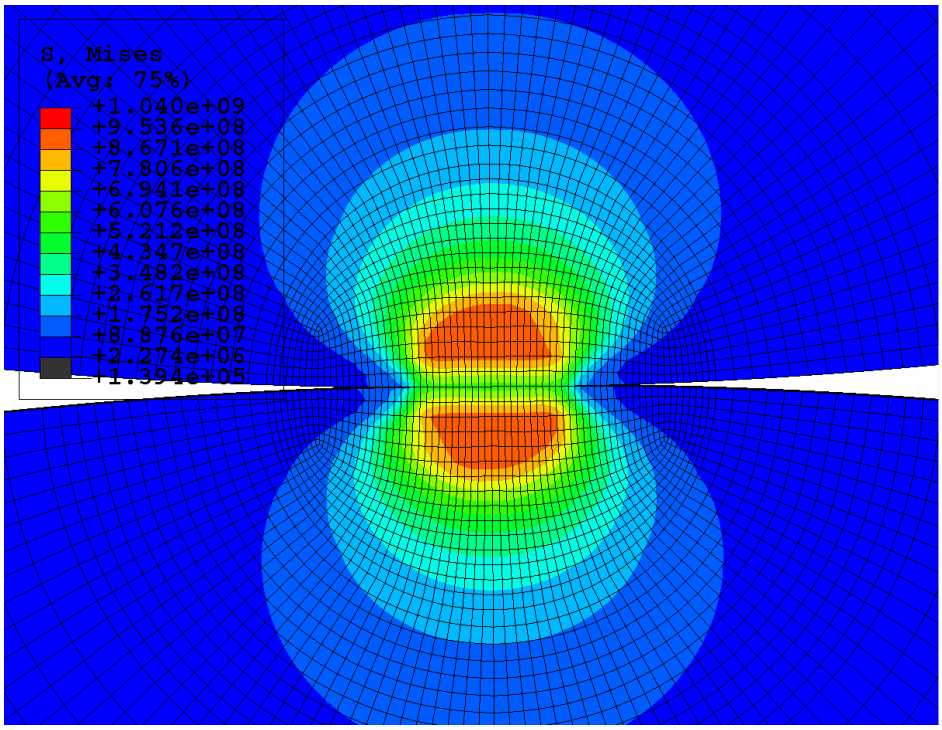

(a)

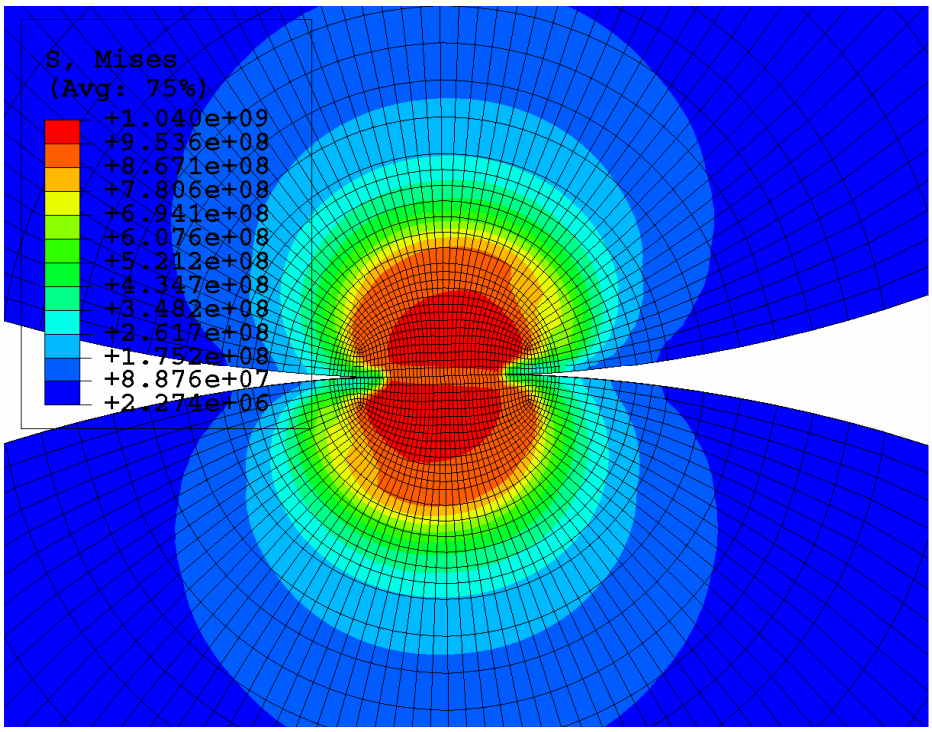

(b)

Figure 3: Von Mises stresses at the point of vertical alignment for steel-on-steel contact for (a)$2\omega_c$ and (b)$15\omega_c$.

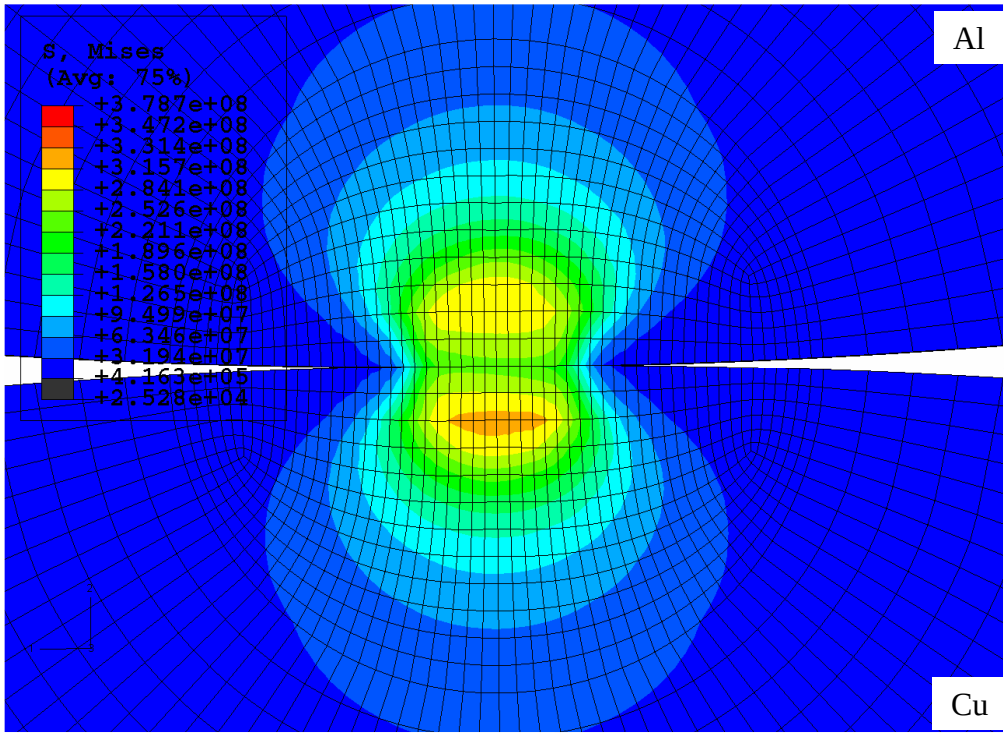

(a)

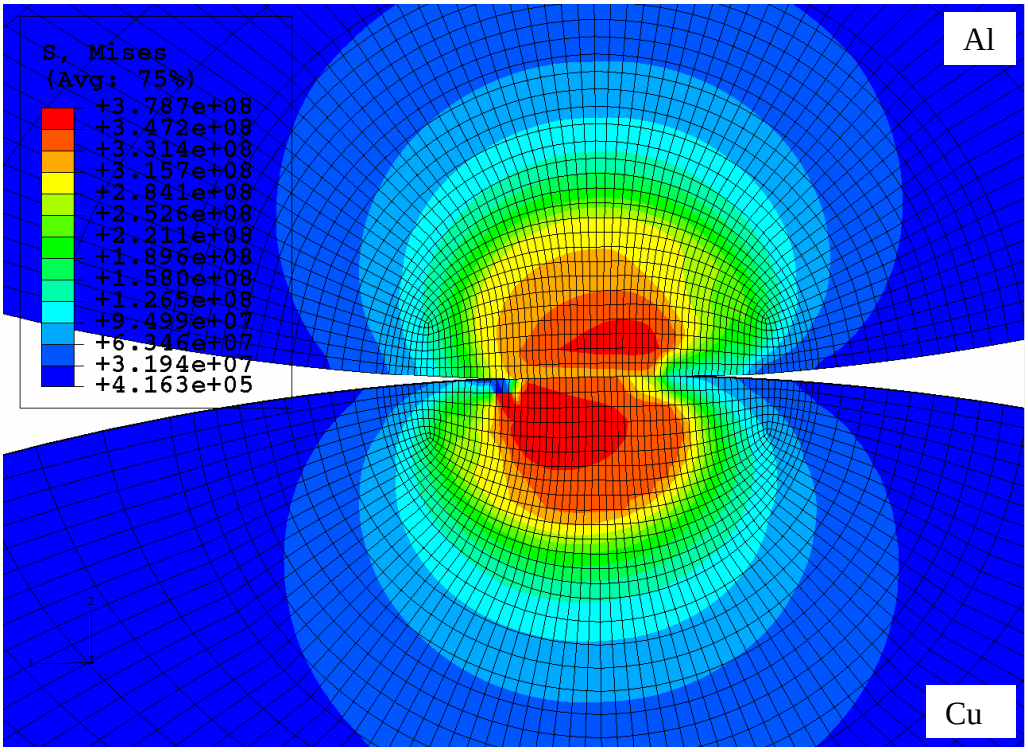

(b)

Figure 4: Von Mises stresses at the point of vertical alignment for aluminum-on-copper contact for (a)$2\omega_c$ and (b)$15\omega_c$.

As sliding progresses the stresses reach a peak value, which is near the point of vertical alignment, as shown in Figures 3 and 4, and then the stress magnitude decreases as the hemispheres move away from each other. Figures 5 and 6 present the residual von Mises stresses in the hemispheres once they have come out of contact for steel-on-steel and aluminum-on-copper sliding, respectively. For the $2\omega_c$ cases shown in Figures 5(a) and 6(a), the residual stresses reduced well below the yield strength indicating that the hemispheres have relaxed and would be able to carry more load before yielding. On the other hand, for the $15\omega_c$ steel-on-steel case, shown in Figure 5(b), the maximum residual stresses are very close to the yield strength. As shown in the figure, the maximum residual von Mises stress is shown to be 911.1 MPa and displays a 0.04% difference to the defined yield strength of 911.5 MPa, which is probably an insignificant difference. It is interesting to note that for the higher interference case, $15\omega_c$, the highest residual stress regions are at the surface while in the lower interference case, $2\omega_c$, the region of highest residual stresses are still below the surface. In the beginning of the sliding process, the hemispheres first yield plastically below the surface, but as sliding progresses the plastic region expands and eventually reaches the surface. One might expect the highest residual stresses to be in the region where the hemisphere first yielded plastically, but as shown by comparing Figures 3 and 5, this is not the case. These residual stresses could be important if one considers shakedown, which, upon successive reloading, the material is subjected to the combined loading of the contact stresses as well as the residual stresses. These residual stresses are protective because they make yielding less likely to occur on subsequent passes. [23]

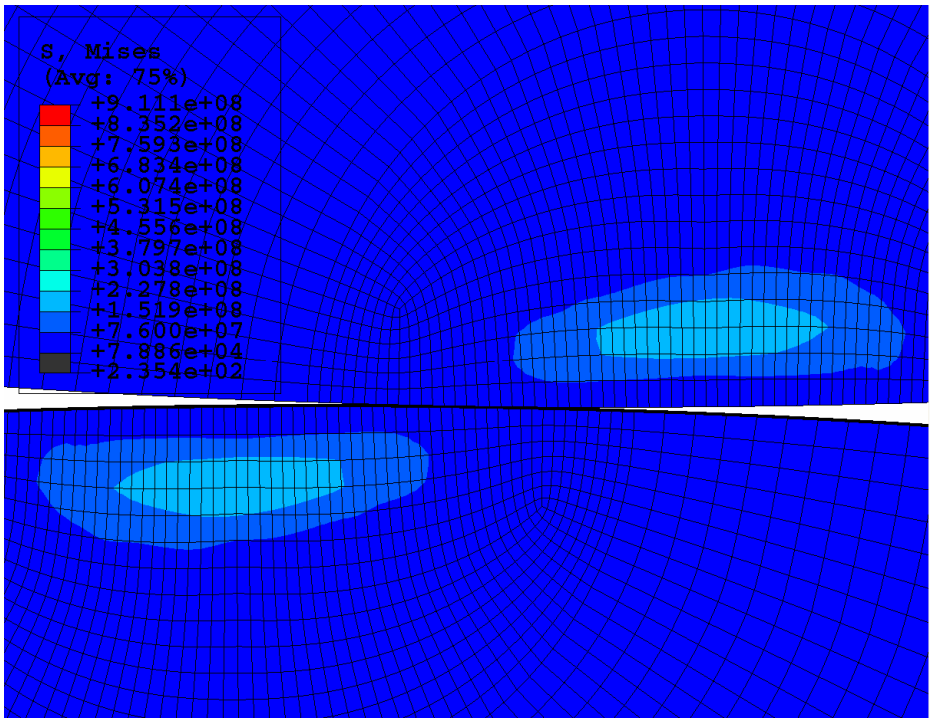

(a)

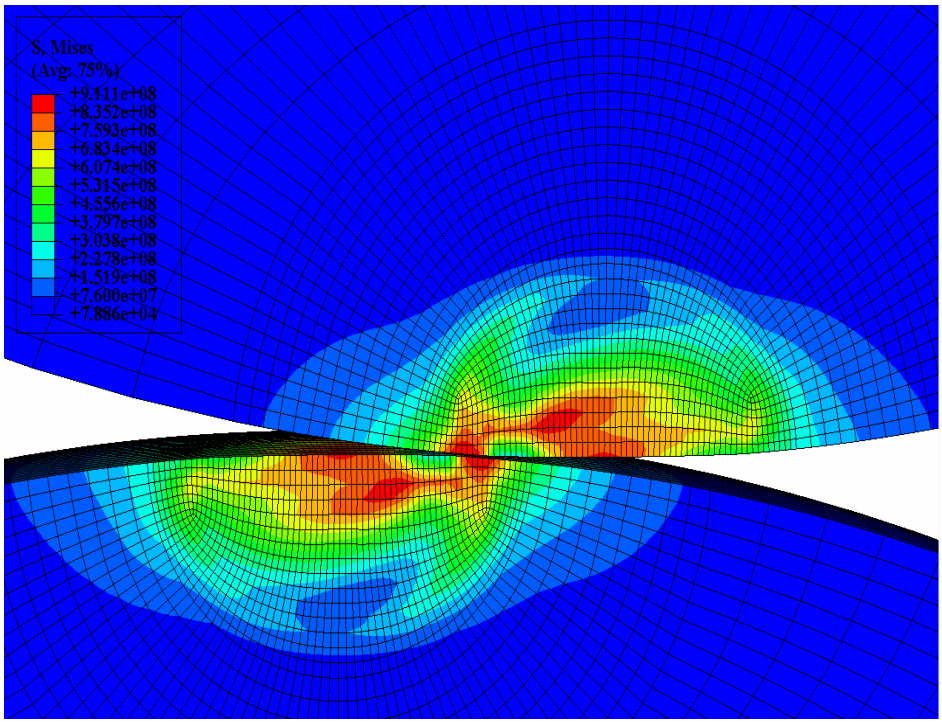

(b)

Figure 5: Residual von Mises stresses at the completion of sliding for steel-on-steel contact for (a)$2\omega_c$ and (b)$15\omega_c$.

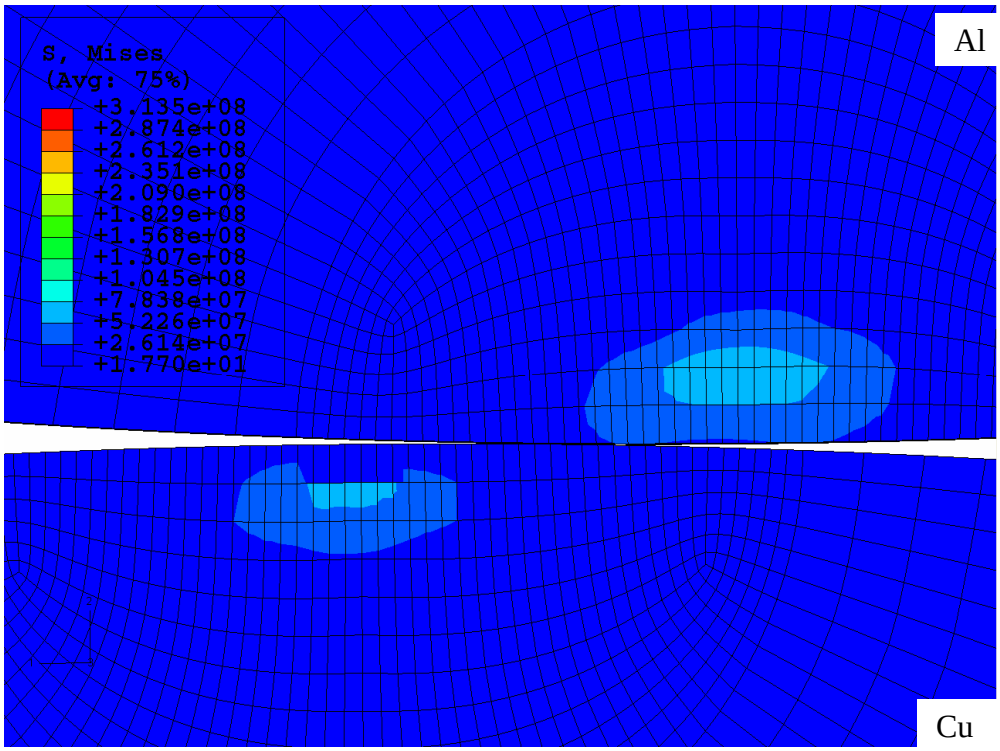

(a)

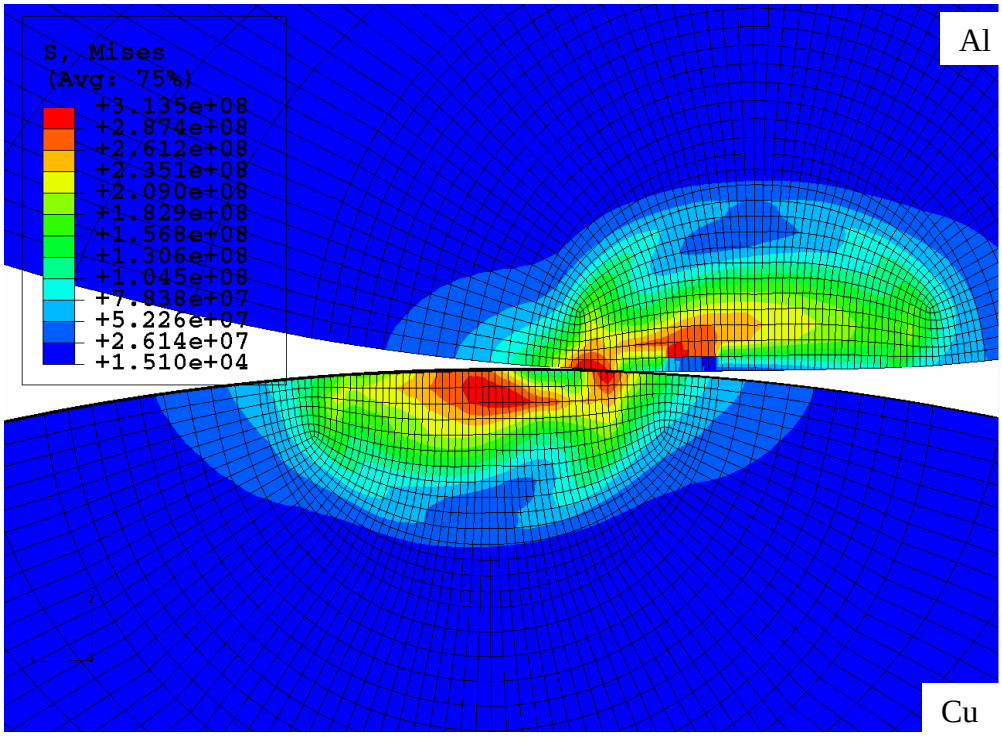

(b)

Figure 6: Residual von Mises stresses at the completion of sliding for aluminum-on-copper contact for (a)$2\omega_c$ and (b)$15\omega_c$.

It is interesting to compare the residual plastic strains in the hemispheres for the material combinations in this analysis. Figures 7 and 8 present the residual plastic strains for steel-on-steel and aluminum-on-copper sliding contact, respectively. As shown in Figure 7, the residual plastic strains are identical in each hemisphere. This is expected as they are identical materials. The lower interference cases, as Figure 7(a) is representative, are nearly symmetric about the center line of the hemispheres and below the surface. As the interference increases, plastic strains reach the surface and the maximum value shifts toward the trailing edge of contact as material is displaced in that direction.

Figure 8 displays the residual plastic strains for aluminum-on-copper sliding contact. As shown in the figure, there is significantly more plastic residual strain in the aluminum hemisphere. Similar to the steel-on-steel cases, as interference increases, the residual plastic strains become less symmetric and shift toward the contact interface.

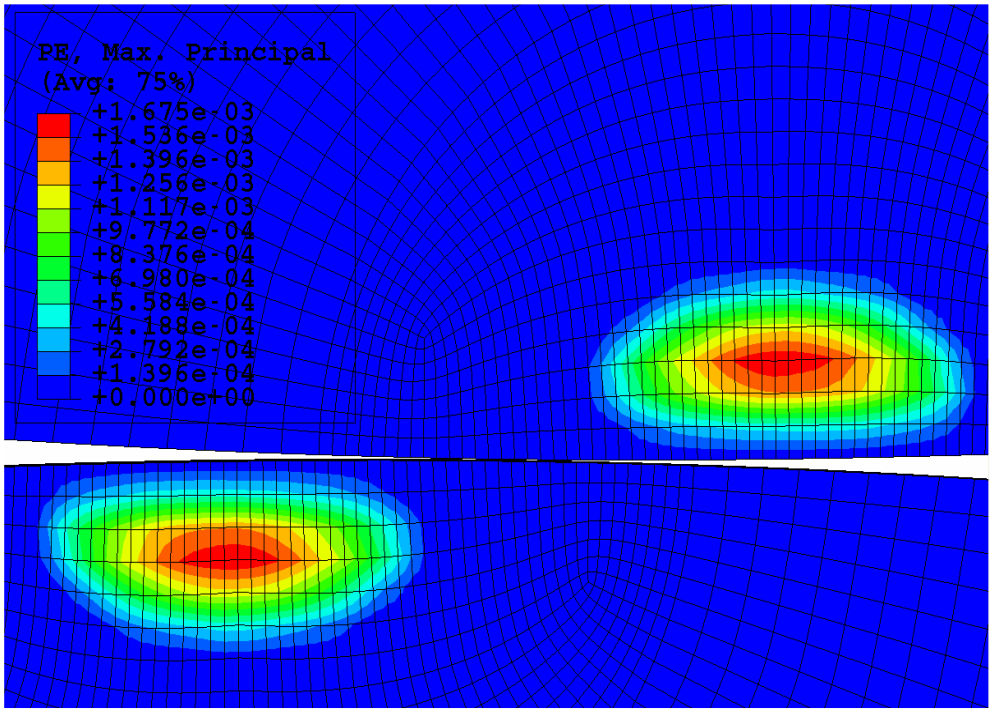

(a)

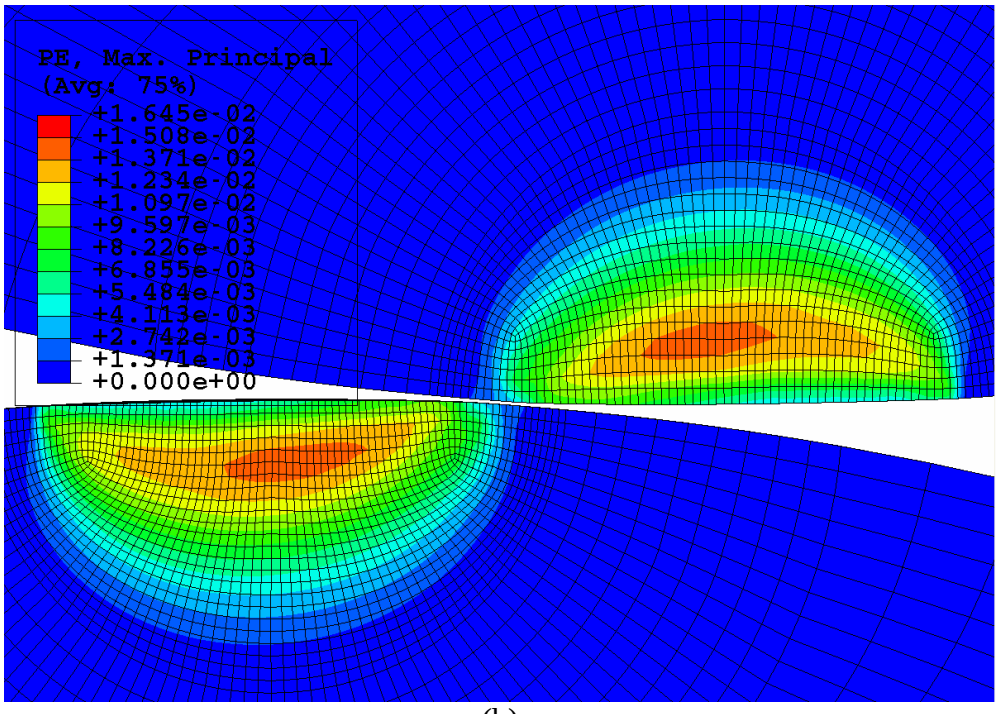

(b)

Figure 7: Residual plastic strains at the completion of sliding for steel-on-steel contact for (a)$2\omega_c$ and (b)$15\omega_c$.

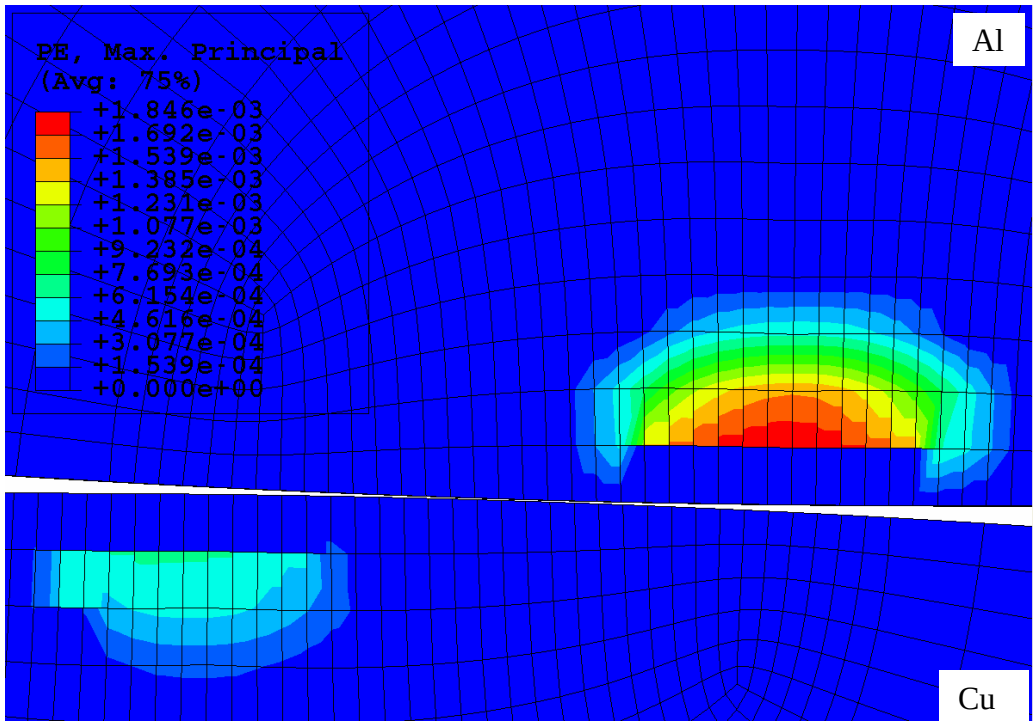

(a)

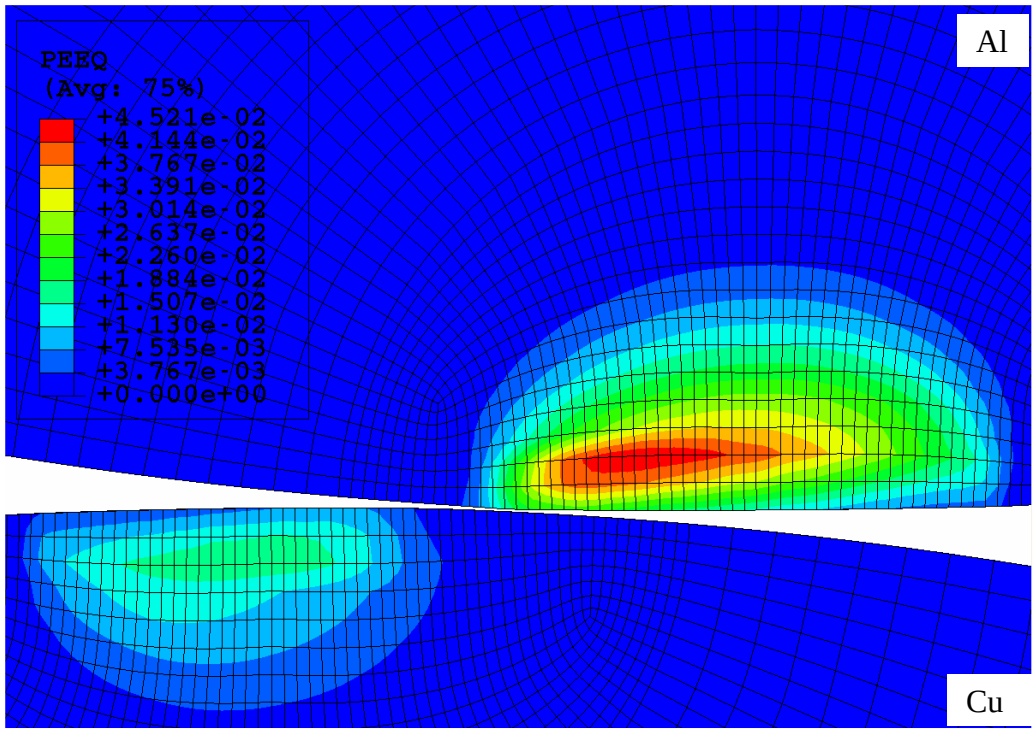

(b)

Figure 8: Residual plastic strains at the completion of sliding for aluminum-on-copper contact for (a)$2\omega_c$ and (b)$15\omega_c$.

Figure 9 presents an oblique view of the von Mises stresses with the upper hemisphere removed at various points in the progression of sliding for a representative and intermediate case of steel-on-steel sliding ($6\omega_c$). The lighter regions in the top of the figures are the top of the hemisphere where contact occurs and the darker regions along the bottom of the figures are the vertically cut face as shown in Figures 3 through 6. This is presented to better visualize how the stress develops along the contacting surface of the hemispheres. Before the hemispheres are vertically aligned, Figure 9(a), a pocket of lower stress surrounded by a high stress ring begins to develop in the contacting region. As sliding progresses further, Figures 9(b) and 9(c), this pocket of lower stress diminishes and a yielded core propagates along the surface where the hemispheres are in contact. Past vertical alignment, Figures 9(c) and 9(d), a pocket of very low stress develops near the high stress core which trails the contact. This low stress pocket continually expands as the hemispheres come out of contact. Figure 9(d) presents the residual stress in the hemisphere with a much expanded low stress pocket.

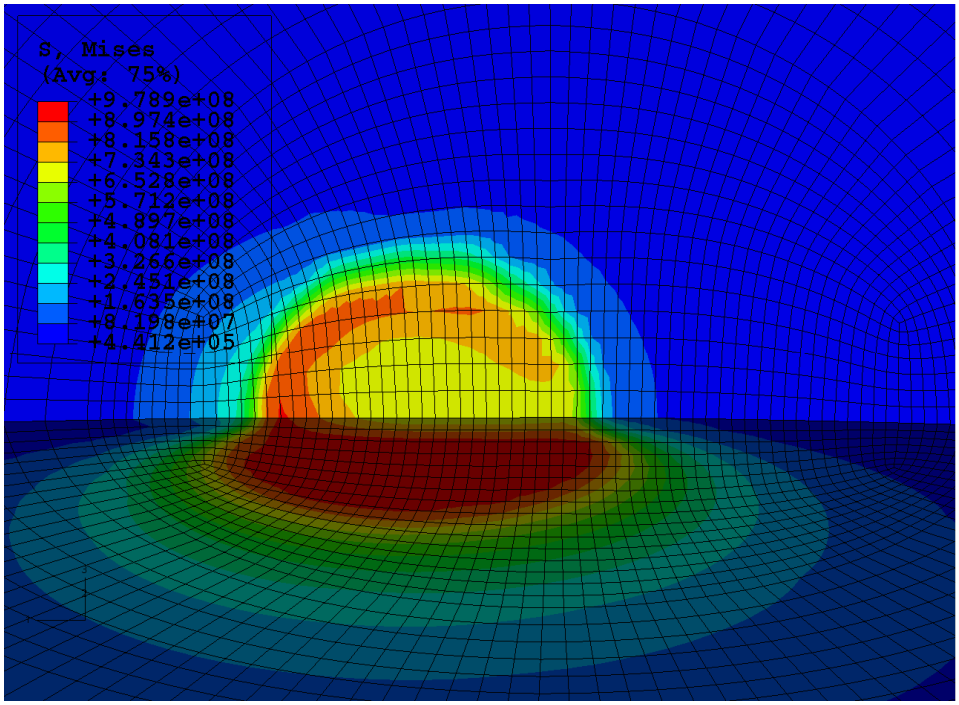

(a)

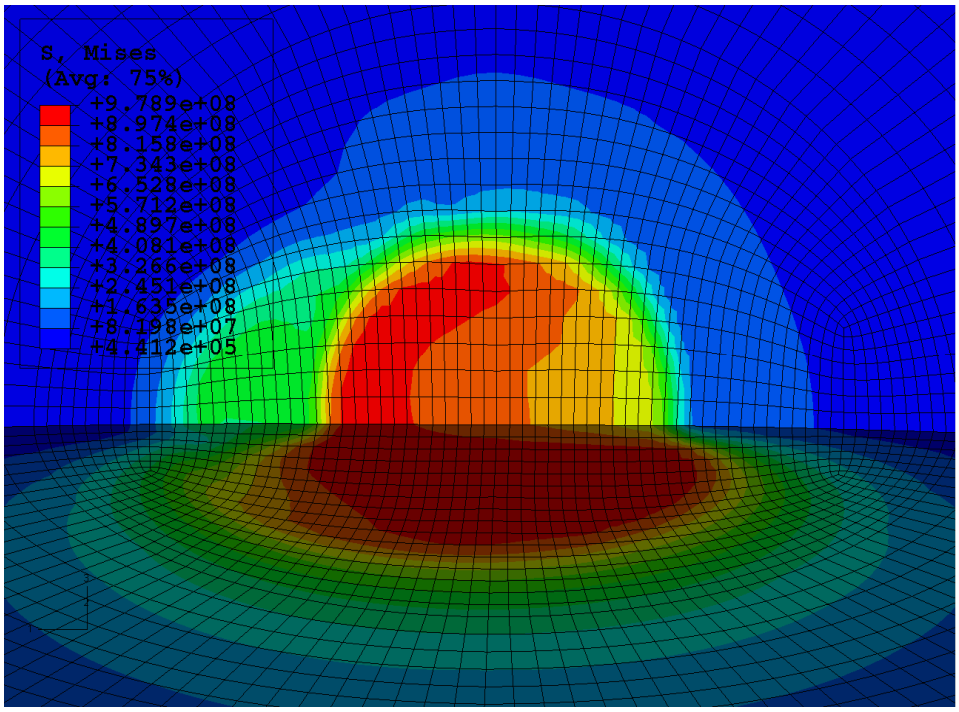

(b)

Figure 9: An oblique view of the von Mises stress in one hemisphere for steel-on-steel contact at an interference of $6\omega_c$ at (a) one-fourth and (b) half of the sliding distance.

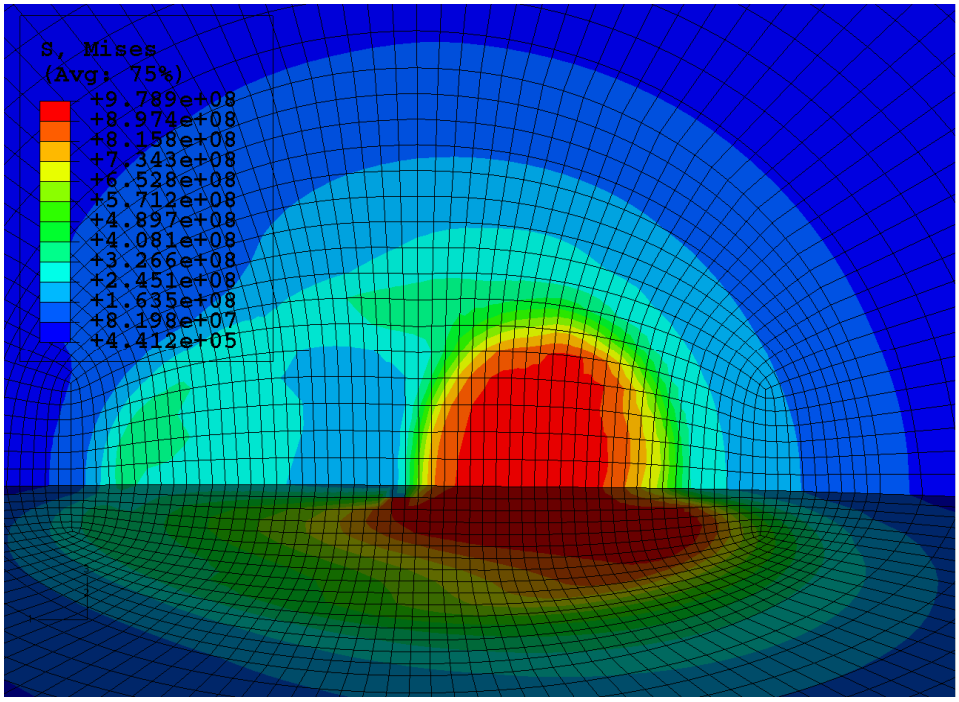

(c)

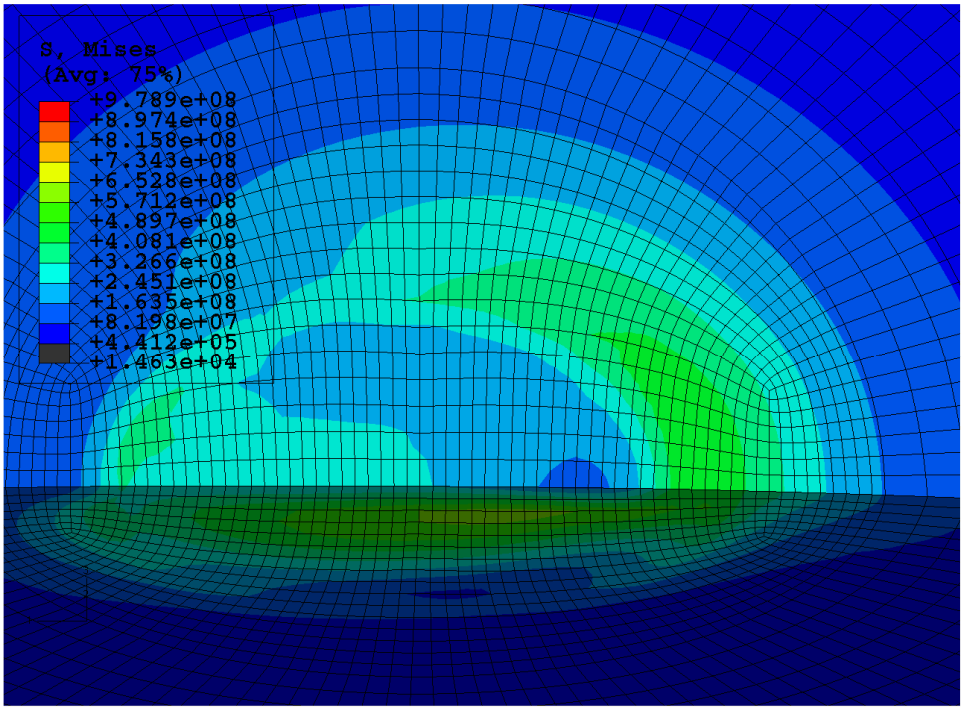

(d)

Figure 9 continued: An oblique view of the von Mises stress in one hemisphere for steel-on-steel contact at an interference of $6\omega_c$ at (c) three fourths and (d) the completion of the sliding distance.

3.2. Forces

The reaction forces on the bottom hemisphere as sliding progresses are also monitored in this study. The action-reaction principle indicates that the reaction forces on the top hemisphere should be identical to that on the bottom hemisphere but in the opposite direction in order to maintain equilibrium. As such, the reaction forces at the base nodes of the bottom hemisphere are summed for each load step and plotted against the normalized horizontal sliding distance, x/R. Figures 10 and 11 present the normalized horizontal reaction forces, F_x/P_c, for the various preset vertical interferences for steel-on-steel contact, and aluminum-on-copper contact, respectively. The normalized vertical reaction forces, F_y/P_c, for steel-on-steel contact, and aluminum-on-copper contact are presented in Figures 10 and 11, respectively. These reaction forces are normalized by the critical load, P_c, as defined previously in Eq. (1).

As sliding begins the horizontal forces start from zero and increase in magnitude to a maximum value then begin to decrease before the hemispheres are vertically aligned ($x/R = 0$). As shown in Figures 10 and 11, the lower interference cases show a nearly anti-symmetric pattern about the x/R axis indicating that very little plastic deformation and, although not shown in the figures, cases run at the critical interference display a perfectly anti-symmetric pattern. As the interference increases, more plastic deformation occurs. This can be seen by the larger magnitude of the negative forces as the hemispheres slide toward vertical alignment compared to the smaller positive force values as the hemispheres come out of contact. As can be seen, the horizontal force is not zero at the point of vertical alignment. This can be attributed to material being

displaced in the direction of sliding impeding the sliding progress even after the hemispheres are vertically aligned.

The normalized vertical reaction force, F_y/P_c, as shown in Figures 12 and 13, show a nearly symmetric pattern about the x/R axis (vertical alignment). As interference increases the maximum forces occur earlier in the sliding progression. This can be attributed to the fact that plasticity is initiated earlier as interference increases. As the material model is nearly elastic-perfectly plastic there is little increase in load carrying capacity in the yielded portion of the hemisphere due to the plastic region just expanding, or flowing under increased load. It can be seen, when comparing Figures 12 and 13, that the curves are nearly identical on a case-by-case basis. This implies that the vertical reaction force, F_y, is normalized well by the critical load, P_c for both steel-on-steel and aluminum-on-copper contact.

It should also be noted, by comparing Figures 12 and 13, how well P_c normalized the reaction force. For instance, if one compares the maximum normalized vertical reaction force of both material combinations for the same normalized vertical interference, they are nearly identical.

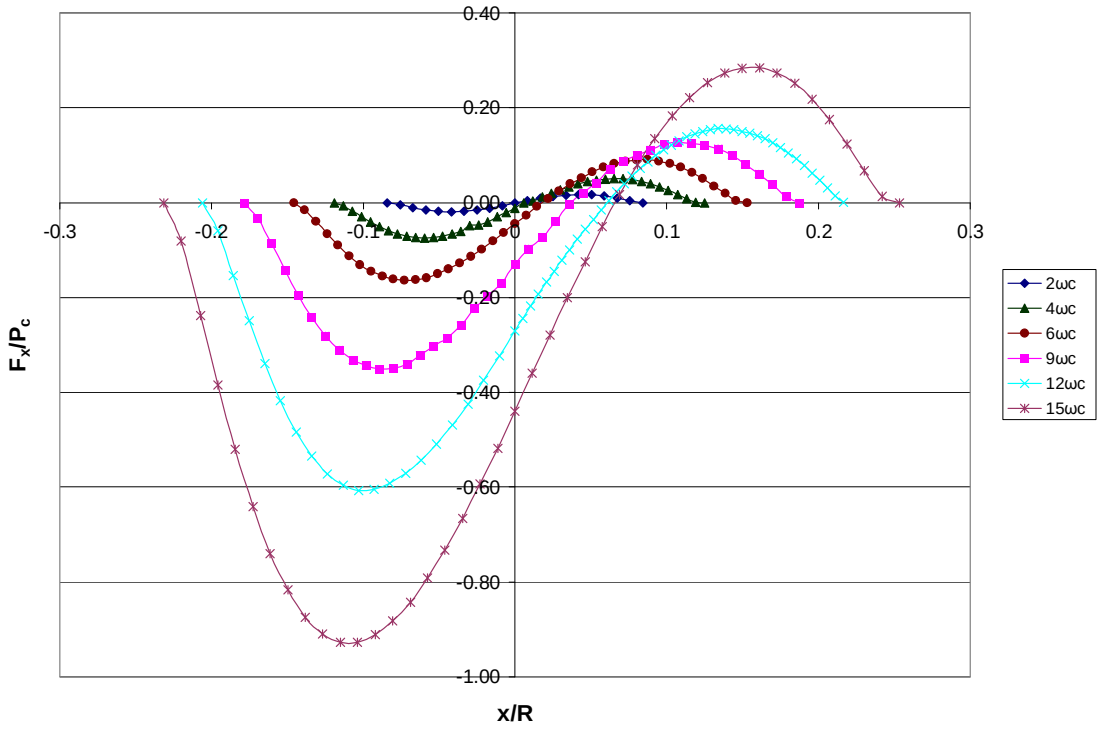

Figure 10: Normalized horizontal reaction forces for $2\omega_c$ through $15\omega_c$ for steel-on-steel contact.

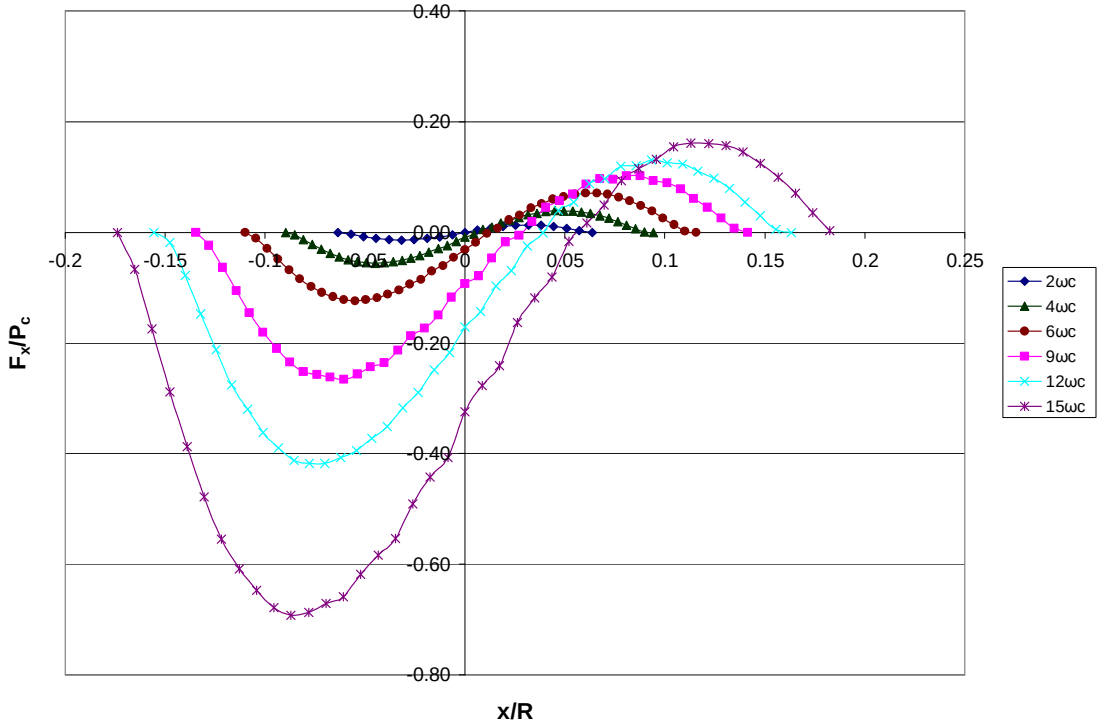

Figure 11: Normalized horizontal reaction forces for $2\omega_c$ through $15\omega_c$ for aluminum-on-copper contact.

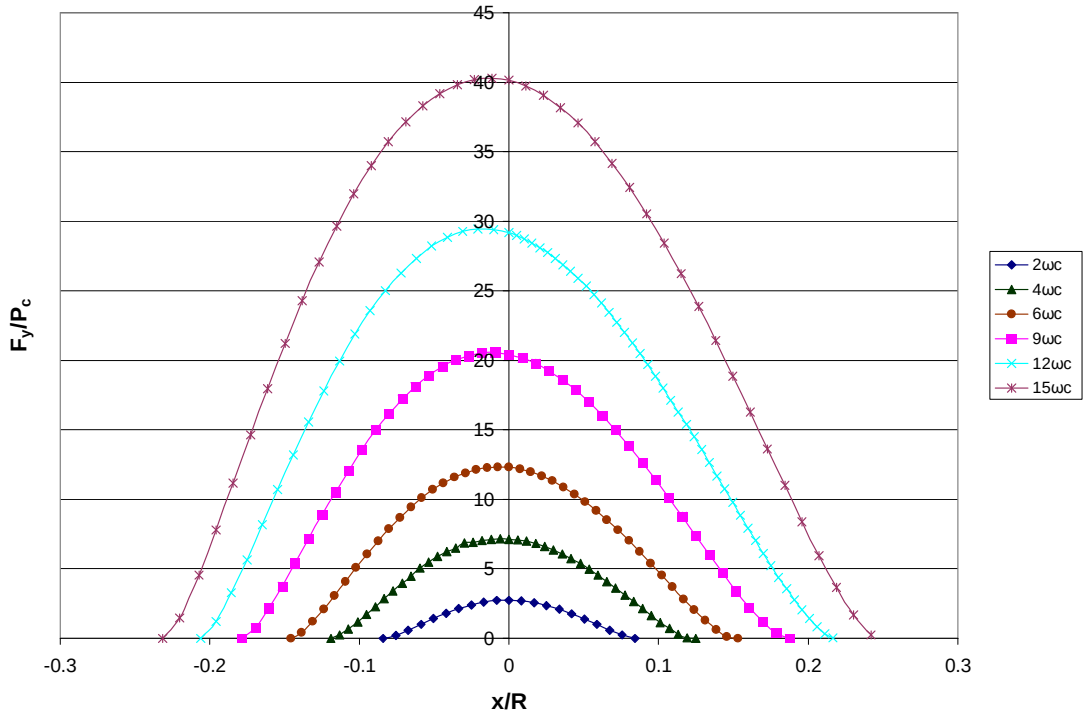

Figure 12: Normalized vertical reaction forces for $2\omega_c$ through $15\omega_c$ for steel-on-steel contact.

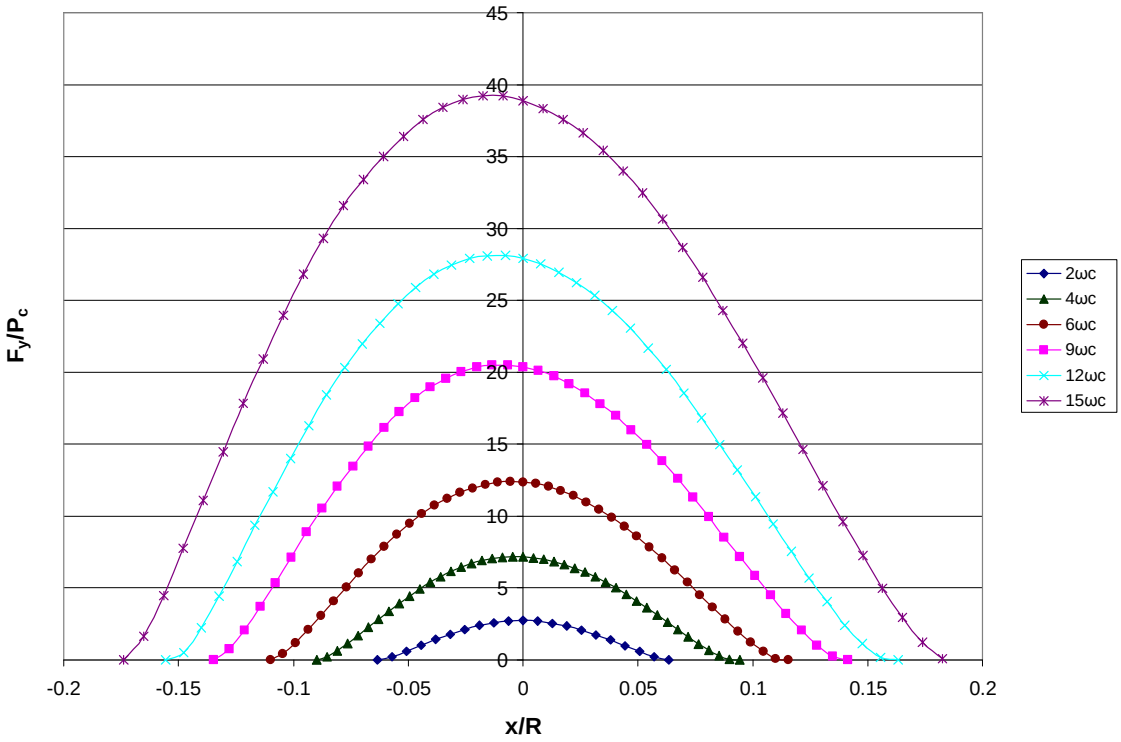

Figure 13: Normalized vertical reaction forces for $2\omega_c$ through $15\omega_c$ for aluminum-on-copper contact.

As there is no friction coefficient imposed in this analysis a “load ratio” is defined as F_x/F_y, being the ratio of the horizontal reaction force with respect to the vertical reaction force in order to better understand the resistance to sliding due to the mechanical interference. While each of the data points on these curves can be thought of as qualitatively similar to the instantaneous local coefficient of friction, it is emphasized that this is not a coefficient of friction in the traditional sense since other effects (e.g., adhesion, surface contamination) are not accounted for. Moreover, in the region where the hemispheres repel each other, the positive “load ratio” does not indicate a negative coefficient of friction. This ratio is generated and plotted versus the normalized sliding distance as shown in Figures 14 and 15 for steel-on-steel and aluminum-on-copper, respectively.

It can be seen that the maximum magnitude of the “load ratio” increases steadily as the preset vertical interference increases. In addition, the plot clearly shows that for all vertical interferences, the maximum magnitude of the “load ratio” during loading is always greater than the maximum magnitude during unloading. It is also clear from the plot that the ratio of the horizontal to the vertical reaction force is not zero at the point where the hemispheres are vertically aligned. This is due to material being displaced in the direction of sliding further opposing the motion. Also of note is the trend of a sharply increasing load ratio as the hemispheres are coming out of contact that occurs for increasing preset vertical interference cases. This is due to the increasing plastic deformation as interference increases. This increase in plastic deformation results in more flattening of the hemispheres in the region of contact, which subsequently reduces the vertical reaction force required to maintain straight line contact.

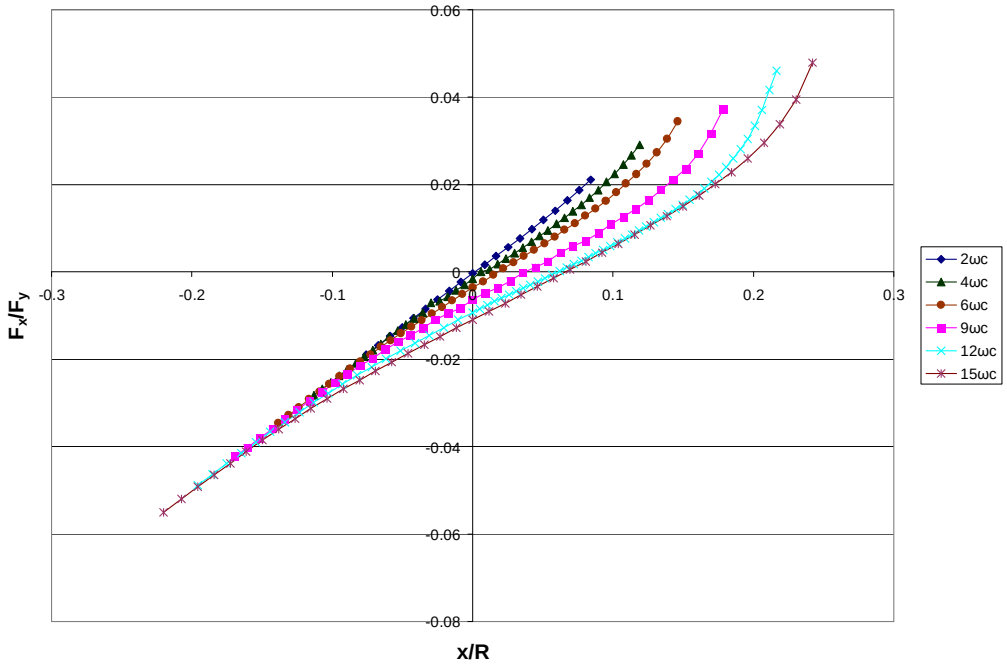

Figure 14: The "load ratio" as sliding progresses for $2\omega_c$ through $15\omega_c$ for steel-on-steel contact.

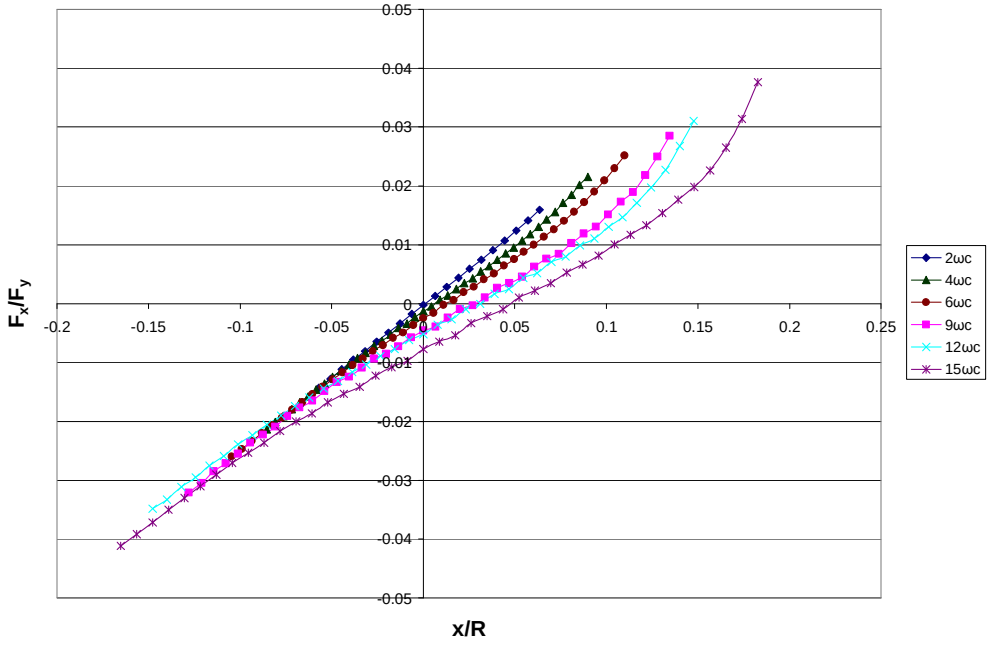

Figure 15: The "load ratio" as sliding progresses for $2\omega_c$ through $15\omega_c$ for aluminum-on-copper contact.

3.3. Energy Loss

Since there is no vertical displacement allowed along the top and bottom boundaries of the hemispheres, the net energy loss in sliding can be defined as

$$U_{net} = \int_{x_1}^{x_2} F_x dx \tag{9}$$

where x_1 and x_2 respectively represent the starting and ending sliding positions of the top hemisphere. This equation is used to quantify the work done when sliding the top hemisphere over the bottom hemisphere. Thus, energy loss in sliding, U_{net}, for individual preset vertical interference cases is essentially the area under the horizontal reaction curves given in Figures 10 and 11. The net energy loss is normalized by U_c from Table 2 and these values are plotted against the normalized preset interference, ω^*, defined as the preset interference divided by the critical interference, ω_c. These values are shown in Figure 16 for steel-on-steel and aluminum-on-copper sliding.

For both steel-on-steel and aluminum-on-copper sliding the energy loss increases drastically as the preset interference increases. In a completely elastic case the work invested in sliding the hemispheres into alignment will be equal to the energy restored as the hemispheres slide out of alignment. The work required to slide the hemispheres to vertical alignment can be thought of as a loading effect similar to a spring being compressed. Past the point of vertical alignment the hemispheres repel each other, similar to a spring expanding.

As the preset interference increases, more of the material becomes plastically deformed as sliding progresses. The portions of the hemispheres that are still elastic once the they are past vertical alignment still do work as they are separating. However, this elastic rebound work will be smaller than the work invested to slide to vertical alignment

and beyond due to the plastic deformation. These effects can also be seen in horizontal reaction force curves shown in Figures 10 and 11. As the interference increases, the work invested (negative portion of the curve) increases faster than the elastic rebound work (positive portion of the curve) resulting in progressively more net energy loss.

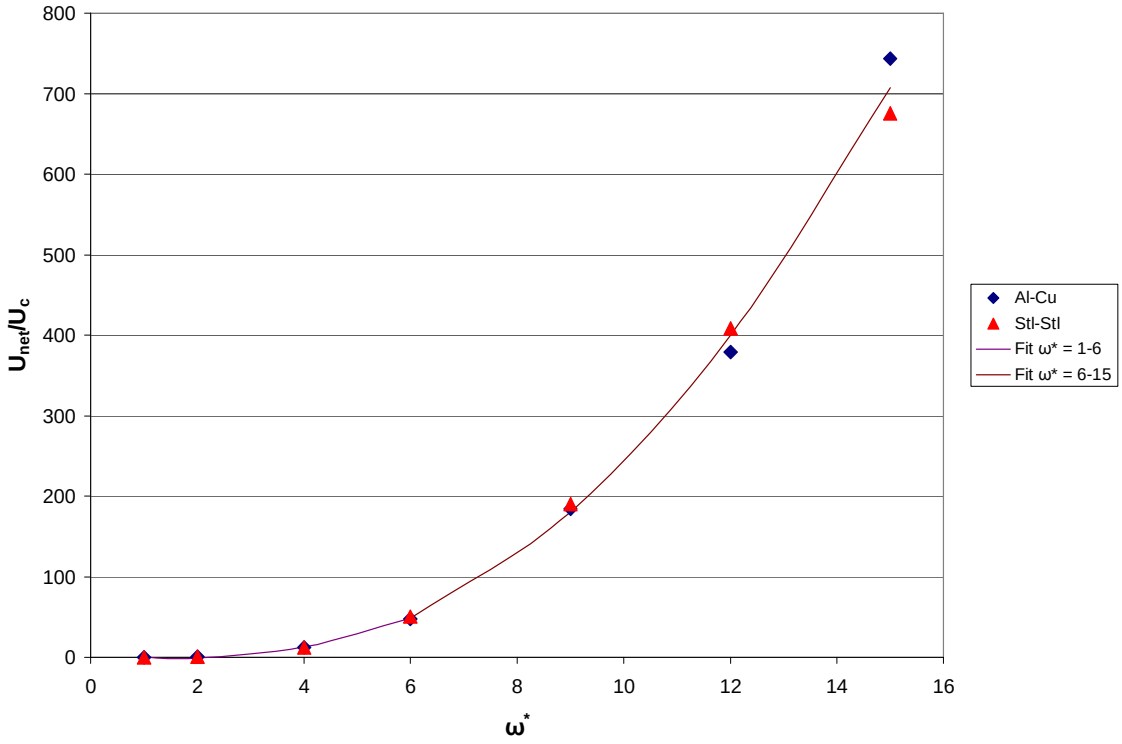

Figure 16: Normalized net energy loss versus preset interference.

As shown in Figure 16, the results for the normalized net energy loss os very close for both aluminum-on-copper sliding and steel-on-steel sliding at a given vertical interference, indicating that U_c normalizes the two cases well. Therefore, a single set of second order polynomial curves are then fitted to the numerical data. They represent the trend followed by energy loss for different ranges of the applied vertical interference, ω^*,

and are found to closely capture the increasing energy loss with increasingly elastic-plastic loading. The fitted equations are as follows:

$$\frac{U_{net}}{U_c} = 0 \qquad \omega^* \le 1$$

$$\frac{U_{net}}{U_c} = -3.594(\omega^* - 1) + 2.661(\omega^* - 1)^2 \qquad 1 \le \omega^* \le 6 \qquad (10)$$

$$\frac{U_{net}}{U_c} = 48.56 + 29.464(\omega^* - 6) + 4.855(\omega^* - 6)^2 \qquad 6 \le \omega^* \le 15$$

These equations are continuous at $\omega^* = 1$ and $\omega^* = 6$.

3.4. Effective Coefficient of Friction

An effective coefficient of friction, $\overline{\mu}$, is introduced as an alternative way to characterize the net energy loss in sliding. A fundamental model is introduced in Figure 17 to help explain this concept. The figure depicts a block, with a normal force, F_y, acting downwards and being pushed across a flat surface by a force, F_x. It is well known that under the conditions depicted in the figure the force required to slide the block across the surface is given by:

$$F_x = \mu F_y \qquad (11)$$

where μ is the coefficient of friction (no distinction is made whether it is a "static" or "kinetic" coefficient of friction). Combining this expression with the definition of work done in sliding results in:

$$W = \int_{x_1}^{x_2} F_x dx = \int_{x_1}^{x_2} \mu F_y dx \qquad (12)$$

Upon rearrangement of this equation one can define the new expression, the effective coefficient of friction, $\overline{\mu}$, given by:

$$\overline{\mu} = \frac{W}{\int_{x_1}^{x_2} F_y \, dy} \tag{13}$$

where $\overline{\mu}$ is an effective coefficient for the entire sliding process.

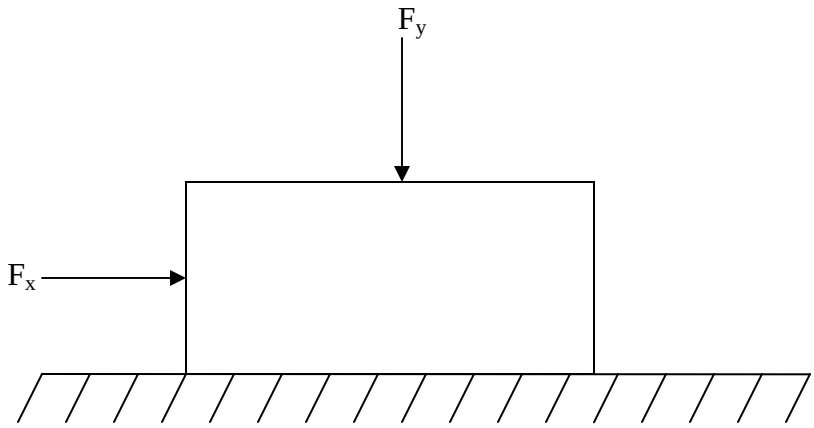

Figure 17: A fundamental schematic of a sliding process.

It has been shown in this analysis that there is resistance to sliding without an imposed friction coefficient due to the mechanical interference. As such, an effective coefficient of friction can be defined as:

$$\overline{\mu} = \frac{U_{net}}{\int_{x_1}^{x_2} F_y \, dx} \tag{14}$$

where U_{net} is defined in Eq. (9). Figure 18 presents the effective coefficient of friction for the various preset vertical interferences. As shown in the figure, both steel-on-steel and aluminum-on-copper start with $\overline{\mu}$=0 for ω^*<1 and then $\overline{\mu}$ for the two material

combinations begins to diverge with increasing interference. The effective coefficient of friction tends to flatten out slightly as interference increases due to an increasing amount of flattening of the hemispheres, thus reducing the resistance to sliding.

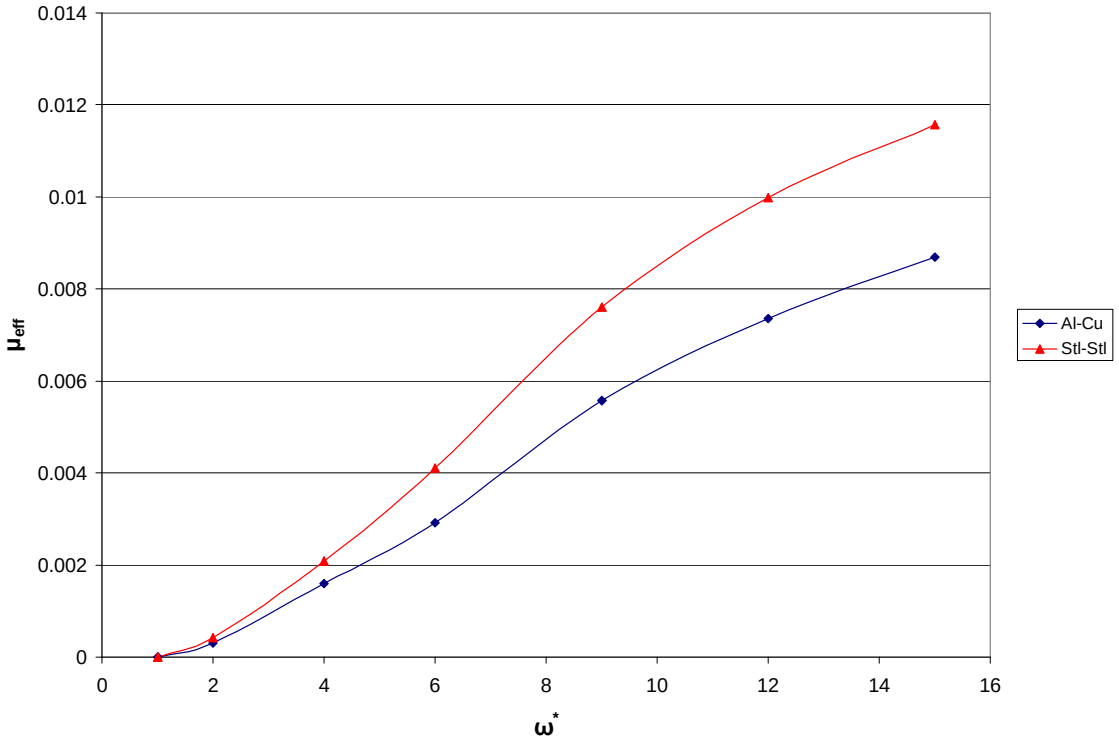

Figure 18: The effective coefficient of friction versus vertical interference.

The effective coefficient of friction in frictionless sliding can be thought of as the contribution of mechanical deformation to the resistance to sliding, or friction coefficient. Since these values are much smaller than friction coefficients measured in practice (an order of magnitude), it must be concluded that friction has a strong interfacial component that is not accounted for in this analysis.

3.5. Contact Area

The real contact area throughout sliding is also investigated in this analysis. The real area of contact is important in many instances. For example, electrical and thermal contact resistance is a function of the real area of contact, which changes depending on the loading condition. Figures 19 and 20 present a plot of the contact area, normalized by the critical contact area, A_c (in Eq. (1)), and defined here as A^*, versus normalized sliding distance, *x/R*. For small vertical interferences the contact area shows a nearly symmetric pattern. As interference increases, the location of maximum contact area occurs progressively earlier in the progression of sliding, similar to the vertical reaction force as presented in Figures 12 and 13. Also, the aluminum-on-copper contact situation shows a larger normalized contact area than the steel-on-steel contact situation for a given preset vertical interference. It is also of note that the contact area snaps down to a smaller value at the point of vertical alignment.

The jaggedness of the contact area curves can be attributed to the resolution of the model. The contact area can only be calculated based on nodal coordinates. The model is composed of discrete elements so even if the contact area extends past the element boundary just slightly, ABAQUS will only recognize the whole element as being in contact. Even with this resolution issue Figures 19 and 20 do present the general trend seen in the contact area for different vertical interferences as sliding progresses for both cases studied.

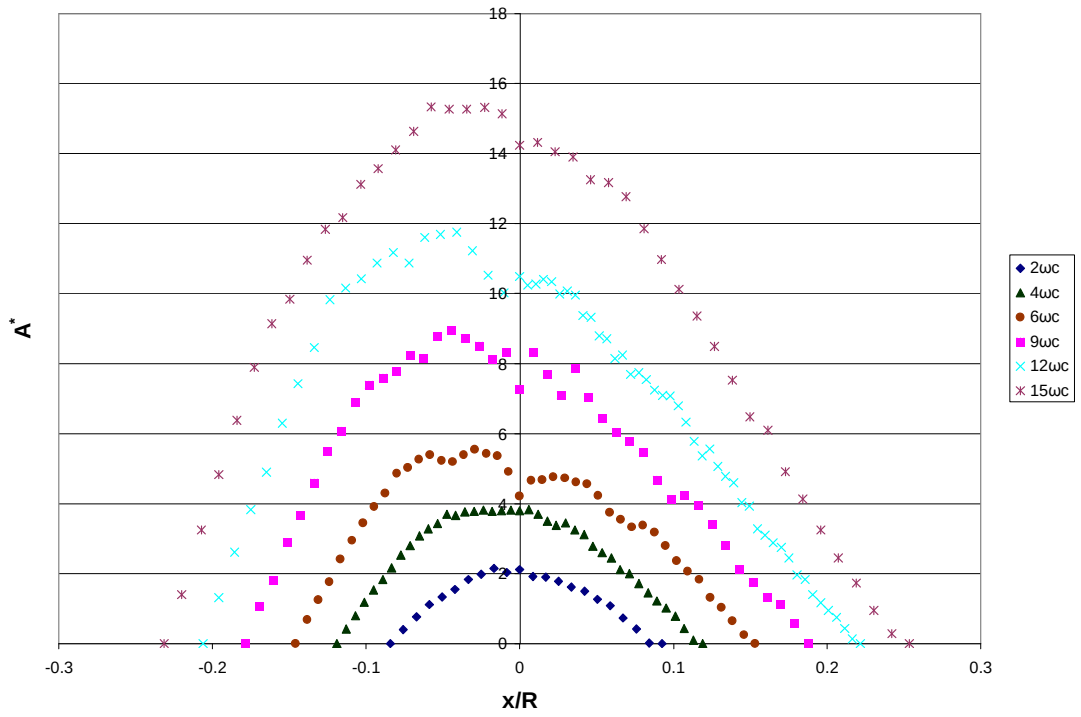

Figure 19: Normalized contact areas for $2\omega_c$ through $15\omega_c$ for steel-on-steel contact.

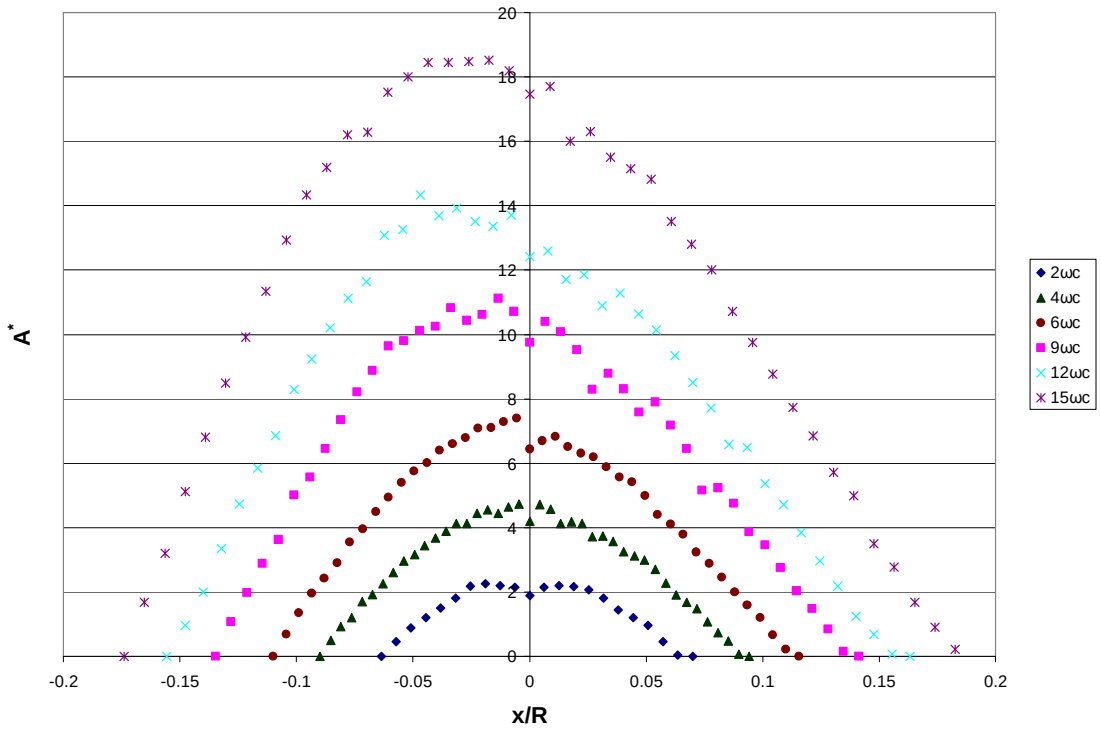

Figure 20: Normalized contact areas for $2\omega_c$ through $15\omega_c$ for aluminum-on-copper contact.

3.6. Deformations

The resulting deformations in the hemispheres as sliding progresses are studied in this analysis as well. Figure 21 presents the maximum normalized vertical deformation, u_{max}/ω_c, in the hemispheres versus normalized sliding distance, x/R, for steel-on-steel contact. As shown in the figure, the deformation increases to a maximum value past the point of vertical alignment and then decreases until the hemispheres come out of contact.

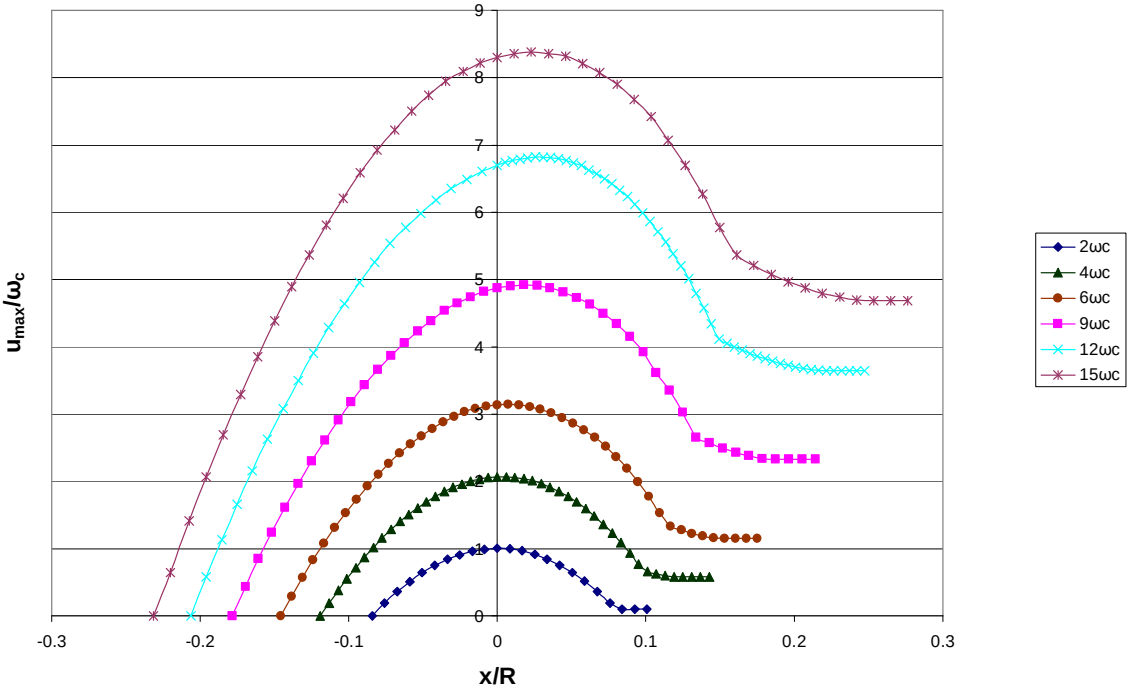

Figure 21: Deformation as sliding progresses for steel-on-steel contact.

Since in the aluminum-on-copper cases, the contact is between two different materials, the upper and lower hemispheres deform differently. Figures 22 and 23 present the normalized deformation in aluminum and copper as sliding progresses for the interferences studied. As shown in the figures, the aluminum deforms much more than the copper due to its much lower elastic modulus and somewhat lower yield strength (see

Table 1). Qualitatively, though they show a similar trend to each other as well as the steel.

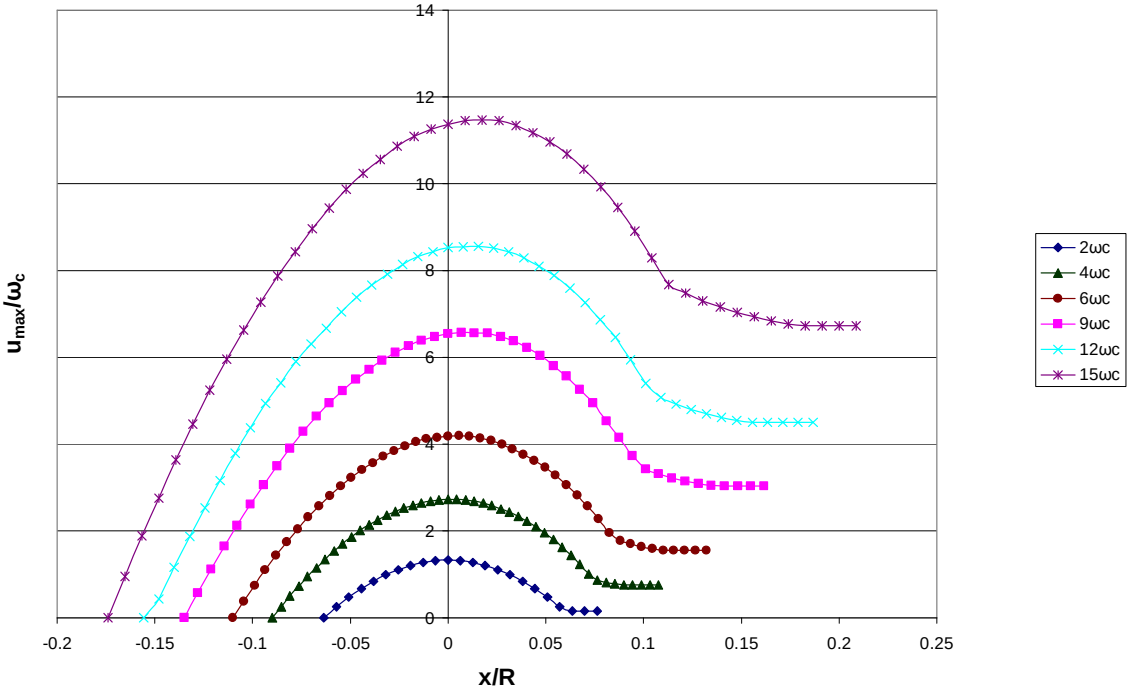

Figure 22: Normalized deformation in aluminum as sliding progresses.

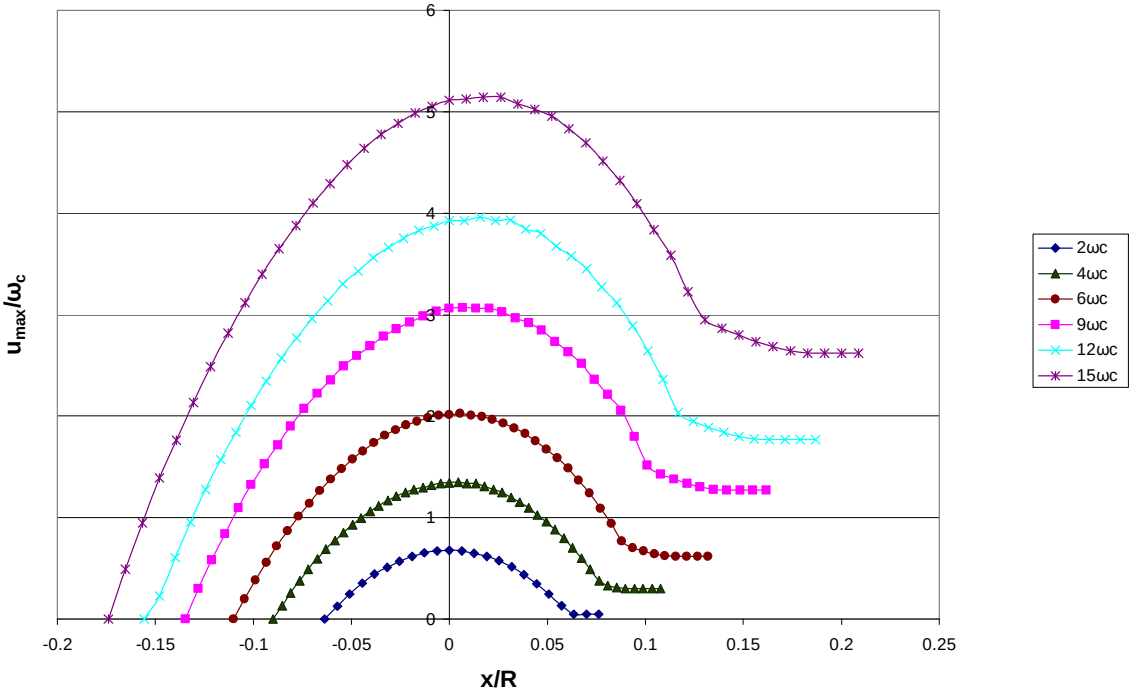

Figure 23: Normalized deformation in copper as sliding progresses.

Once the hemispheres have come out of contact they are left with residual deformation. This can be seen as a flattening out of the deformation curves in Figures 21 through 23. The simulation is run past the point when the hemispheres come out of contact in order to capture this phenomenon. This deformation is due to plasticity effects and is unrecoverable. Figure 24 presents a plot of the residual deformations, u_{res}, normalized by the critical interference, ω_c versus preset vertical interference, ω^*. The residual deformations dramatically increase as the interference increases. A polynomial curve fit that closely approximates the data for steel-on-steel sliding contact is given by:

$$\frac{u_y}{\omega_c} = 0.2(\omega^* - 1) + 0.01(\omega^* - 1)^2 \qquad 1 \le \omega^* \le 15 \qquad (15)$$

The aluminum and copper results are qualitatively similar to the steel results. However, the copper hemispheres show significantly less residual deformation. This is reasonable if one considers the fact that the copper has a higher yield strength than the aluminum such that the aluminum hemisphere will absorb most of the deformation. A polynomial curve fit for aluminum in aluminum-on-copper sliding contact is given by:

$$\frac{u_y}{\omega_c} = 0.248(\omega^* - 1) + 0.014(\omega^* - 1)^2 \qquad 1 \le \omega^* \le 15 \qquad (16)$$

and a curve fit for copper in aluminum-on-copper sliding contact is given by:

$$\frac{u_y}{\omega_c} = 0.095(\omega^* - 1) + 0.006(\omega^* - 1)^2 \qquad 1 \le \omega^* \le 15 \qquad (17)$$

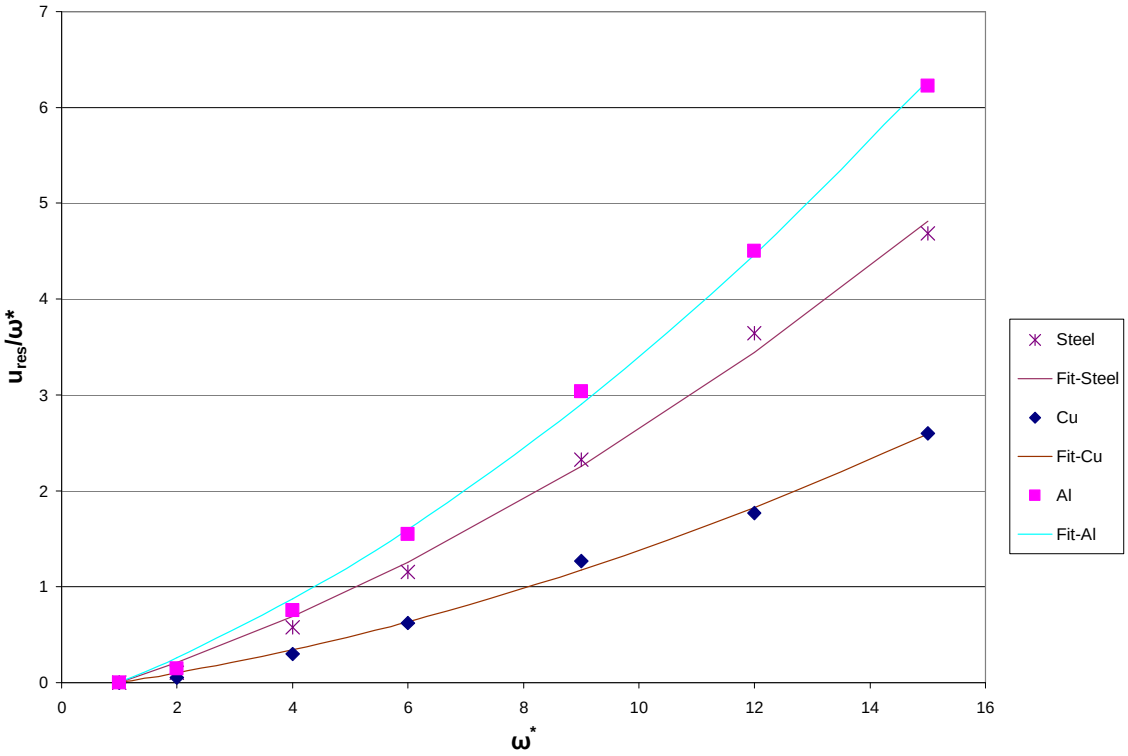

Figure 24: Residual deformations versus preset interference for aluminum-on-copper contact

3.7. Conclusions

The results of the FEA of frictionless sliding in the elastic-plastic domain between two hemispheres are discussed. Results are presented for sliding between two steel hemispheres and between an Al and a Cu hemisphere. The resultant parameters such as deformations, forces, stresses, and energy losses that occur are presented and explained. All the results are presented nondimensionally in order to apply to hemispherical contact at any scale. The development and propagation of stress in the hemispheres as sliding progresses is discussed. It is found that as the interference increases, the stresses in the

hemispheres expand and reach the surface at values slightly above the yield strength. The reaction forces required to maintain straight line contact are investigated and a "load ratio" is defined, similar to a friction coefficient due to mechanical interference only. A single set of equations is derived to characterize the energy loss due to plastic deformation in both cases because it is found that the magnitudes of the net energy at the end of sliding are similar for all cases analyzed. An effective coefficient of friction is introduced in order to help quantify energy loss due to plasticity. Equations to characterize residual deformations in steel-on-steel contact and aluminum-on-copper contact are derived. It is shown that aluminum shows more deformation than copper throughout the progression of sliding. Contact areas during sliding are presented and it is also found that the normalized dimensions of the contact region are larger in aluminum-on-copper contact.

CHAPTER IV: RESULTS—FRICTIONAL

The frictionless results presented previously represent the resistance in sliding due to only the mechanical interference. An imposed friction coefficient is introduced to the model to represent additional effects that could impede sliding as in adhesion, for instance. In this analysis, a coefficient of friction of 0.3 is used as a representative value for metallic contact situations. The frictional model in ABAQUS as used here is a basic Coulomb friction model that adds a shear traction at the surface that is proportional to the contact pressure by the friction coefficient imposed at that location because a displacement is specified. If, however, a force boundary condition were to be applied, then the hemispheres may or may not slide if the shear traction has reached the threshold established by the contact pressure scaled by the imposed friction coefficient. This is the most basic form of a friction coefficient in ABAQUS in that it is isotropic and is constant (i.e., has no dependence on slip-rate, contact pressure, temperature).

4.1. Stresses

For the steel-on-steel contact cases, the stress regions formed in both hemispheres are anti-symmetric about the normal to the contact interface throughout the course of the sliding process. For the aluminum-on-copper cases, the stress regions formed in the hemispheres are not anti-symmetric due to the differences in material properties. In all cases, regions of high stress initially develop below the contact surface. As sliding progresses and load on the hemispheres increases, yielding occurs and a sub-surface

plastic core develops. Elastic material surrounds this plastic core, and provides the greater part of resistance to sliding. As the load continues to increase with the progression of sliding, the elastic region diminishes, making way for the growth and propagation of a plastic core, which reduces the resistance to sliding.

At the vertical axis of alignment, as seen in Figures 25 and 26 for $2\omega_c$ and $15\omega_c$ steel-on-steel and aluminum-on-contact, respectively, the von Mises stress distribution in both hemispheres is mostly identical (identical in the steel-on-steel case). A main difference between the frictional and frictionless sliding is that in frictional sliding the stress patterns are symmetric about a line angled in a direction that opposes the sliding. Whereas in frictionless sliding the stress patterns are symmetric about the vertical. This is the effect of the friction coefficient between the two surfaces which contributes to the tugging action that results from mechanical interference that opposes sliding. It should be noted that, due to the resolution of the contour intervals it is not clear in Figures 23(a) and 24(a), the hemispheres have yielded. Though, similarly to the frictionless cases, the yielded regions are below the surface.

Figures 27 and 28 present the residual von Mises stress distribution once the hemispheres come out of contact for $2\omega_c$ and $15\omega_c$ steel-on-steel and aluminum-on-copper, respectively. It can be seen that the highest residual stresses are at the surface. Also, there is more flattening of the aluminum surface than the copper when sliding completes as shown in Figure 28(b). It is of note that the residual stresses in each hemisphere are well below the yield strength.

Figures 29 and 30 present the residual plastic strains for steel-on-steel and aluminum-on-copper sliding contact, respectively. As shown in Figure 29, the residual

plastic strains are identical for both hemispheres and have reached the surface. As interference increases, the maximum residual stress increases and shifts towards the leading edge of contact. In aluminum-on-copper sliding contact, as shown in Figure 30, the aluminum displays much more residual plastic strain than the copper. As interference increases, the volume of plastically strained material expands, eventually covering the entire contacting area.

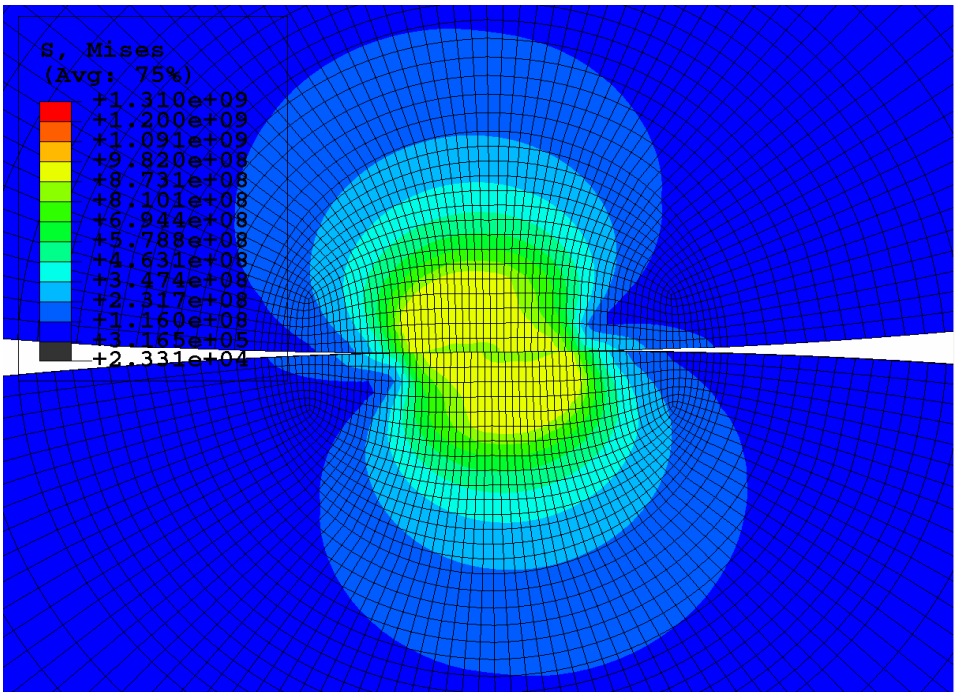

(a)

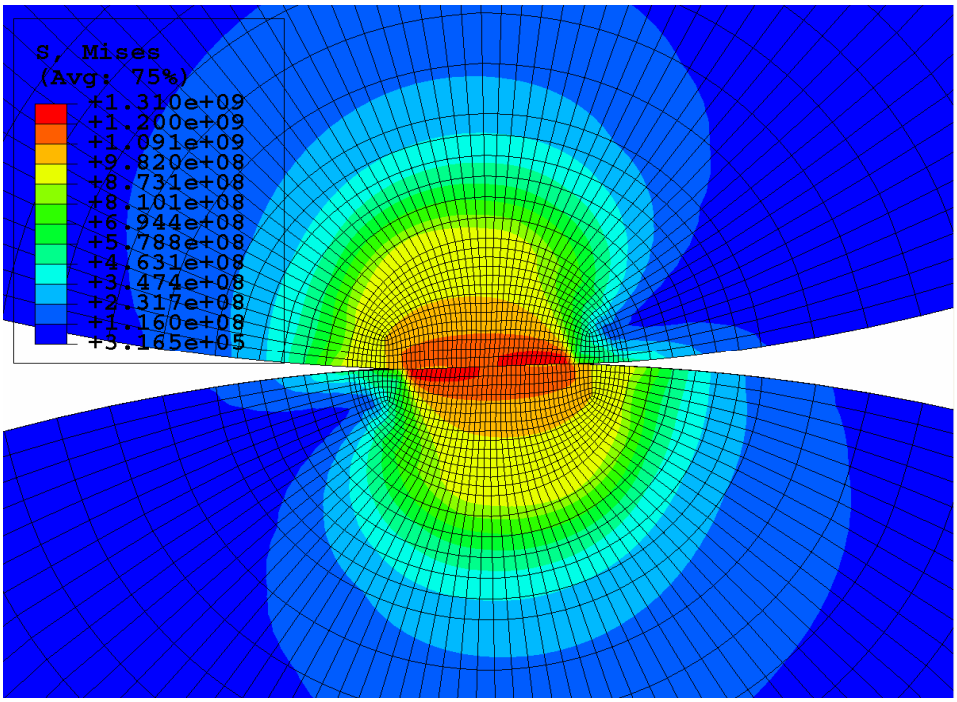

(b)

Figure 25: Von Mises stress in $2\omega_c$ (a) and $15\omega_c$ (b) at the point of vertical alignment for frictional steel-on-steel sliding contact.

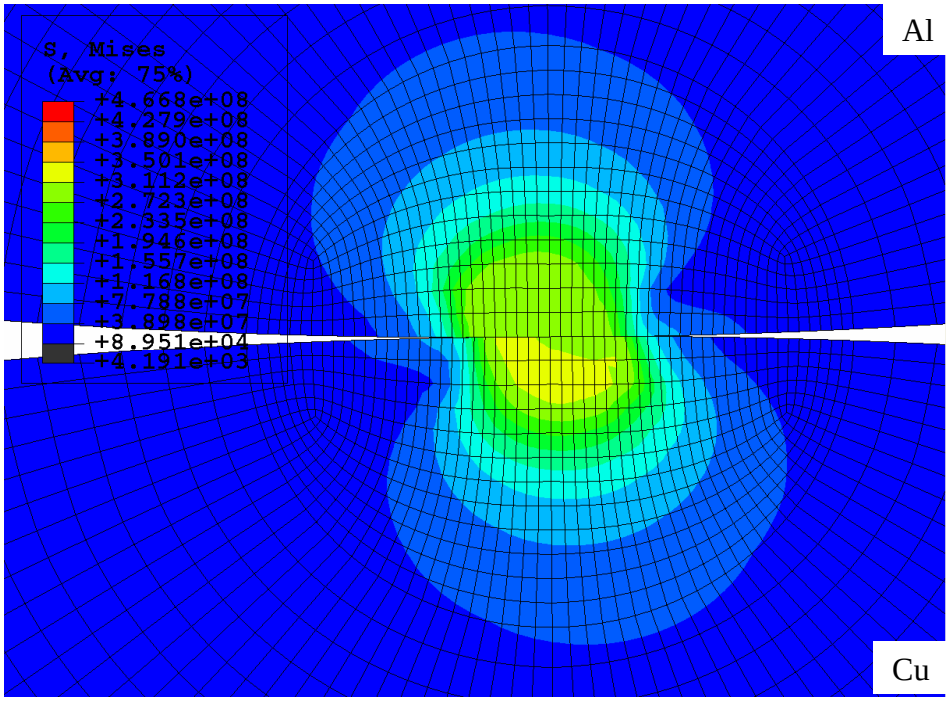

(a)

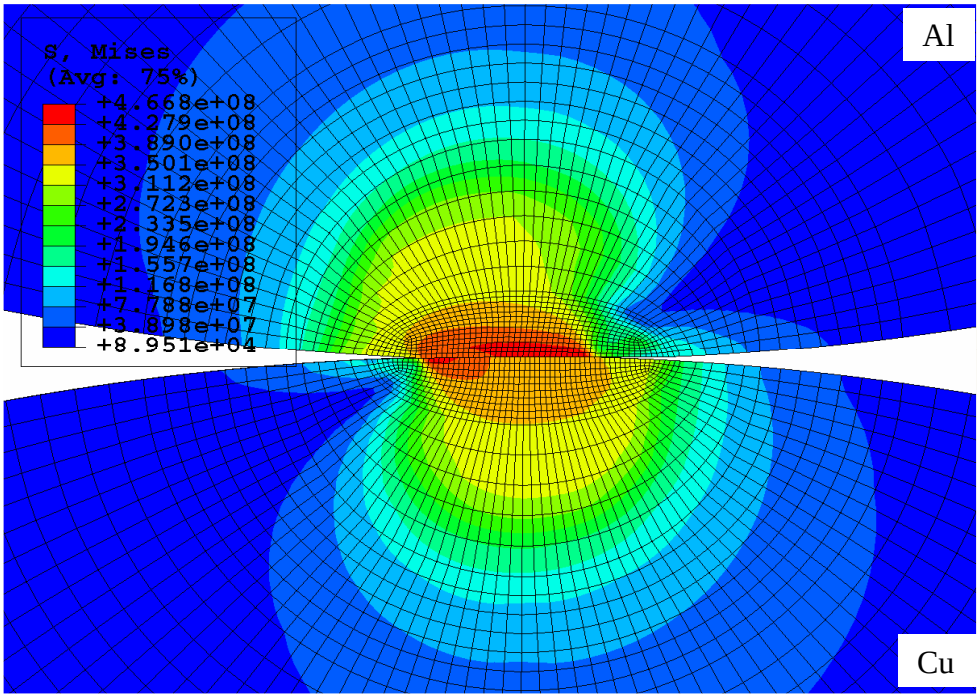

(b)

Figure 26: Von Mises stress in $2\omega_c$ (a) and $15\omega_c$ (b) at the point of vertical alignment for frictional aluminum-on-copper sliding contact.

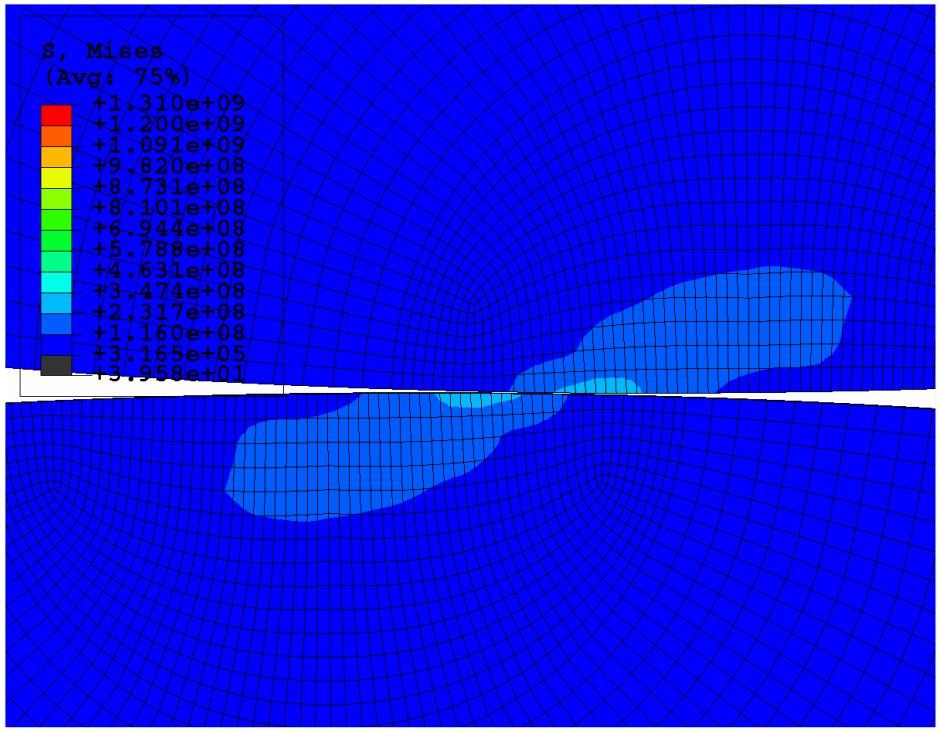

(a)

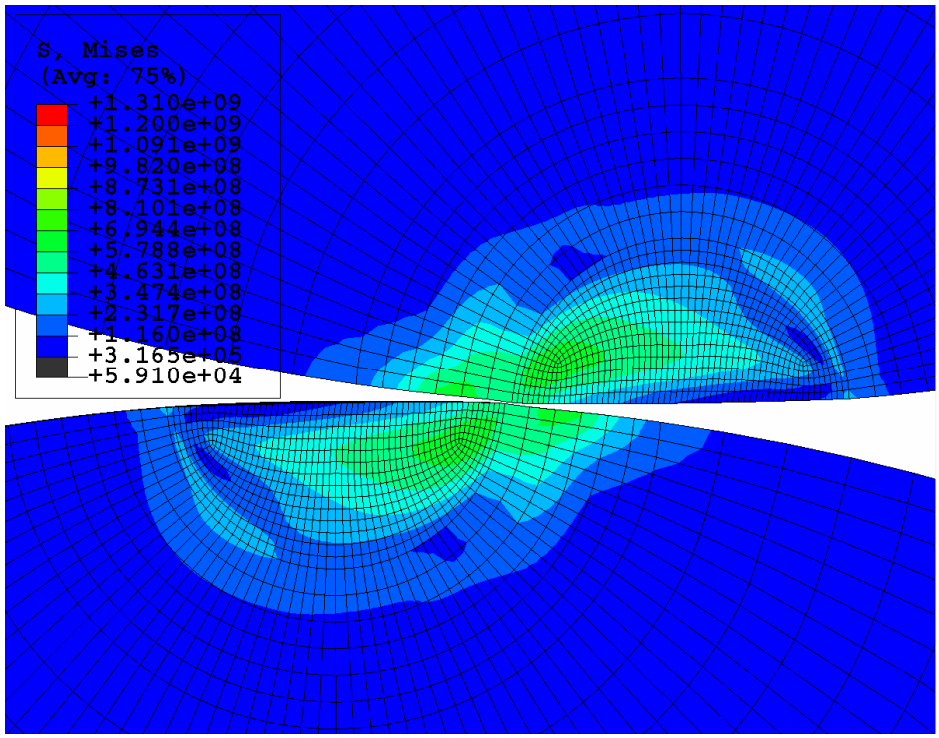

(b)

Figure 27: Residual von Mises stress in $2\omega_c$ (a) and $15\omega_c$ (b) at the completion of sliding for frictional steel-on-steel contact.

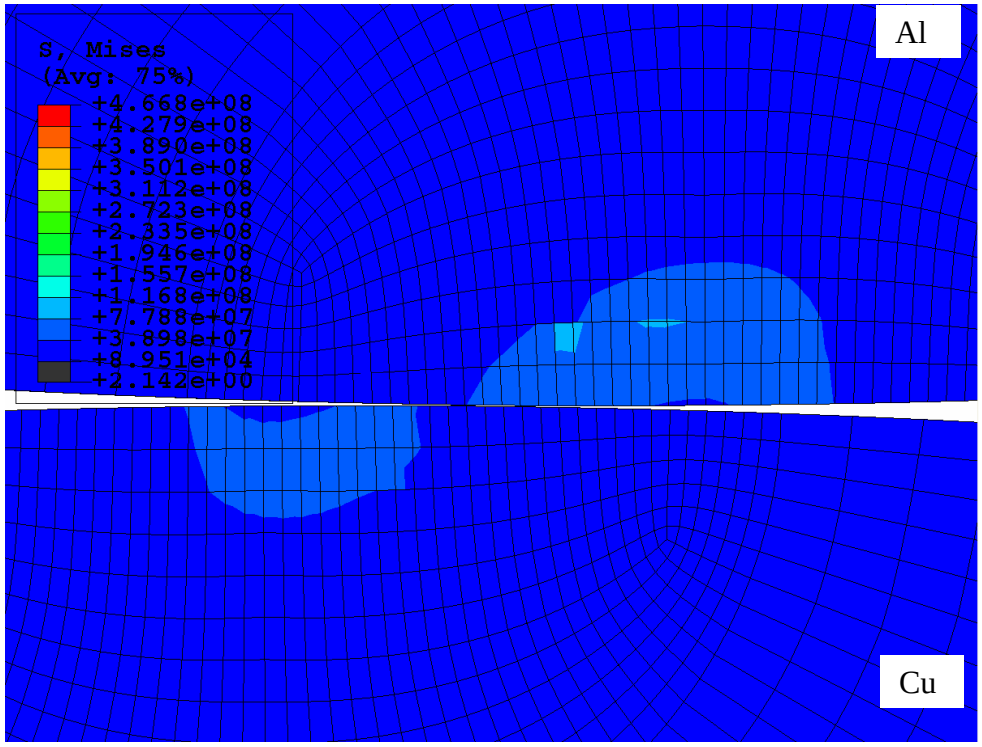

(a)

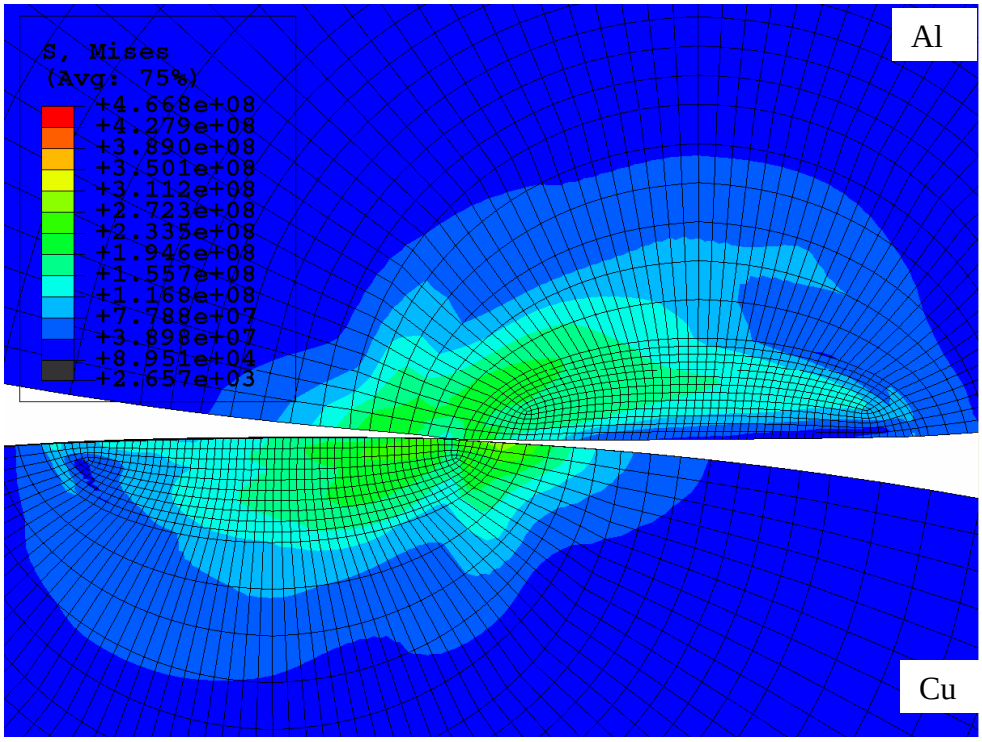

(b)

Figure 28: Residual von Mises stress in $2\omega_c$ (a) and $15\omega_c$ (b) at the completion of sliding for frictional aluminum-on-copper contact.

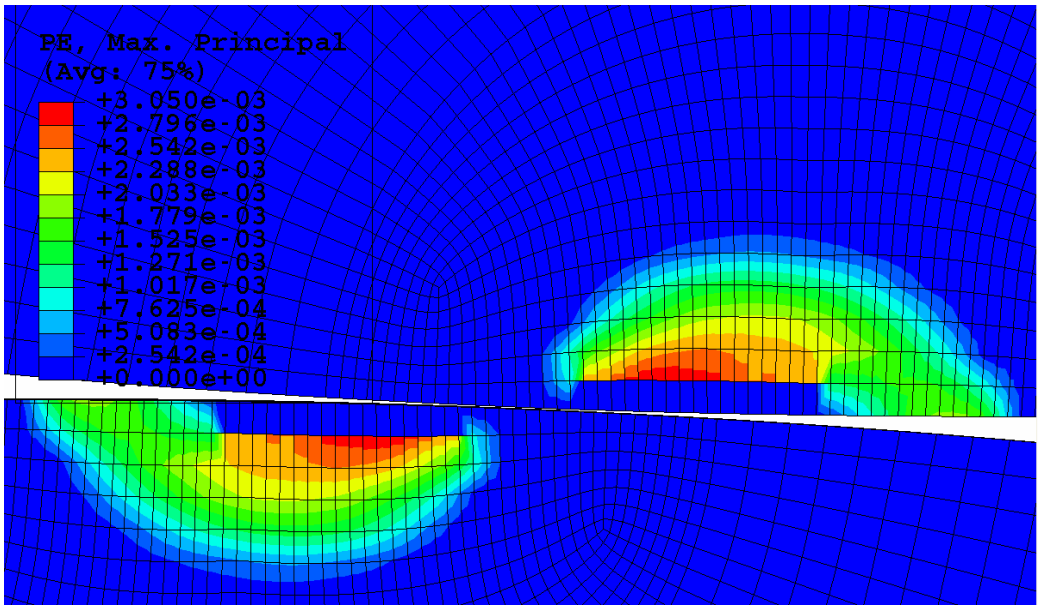

(a)

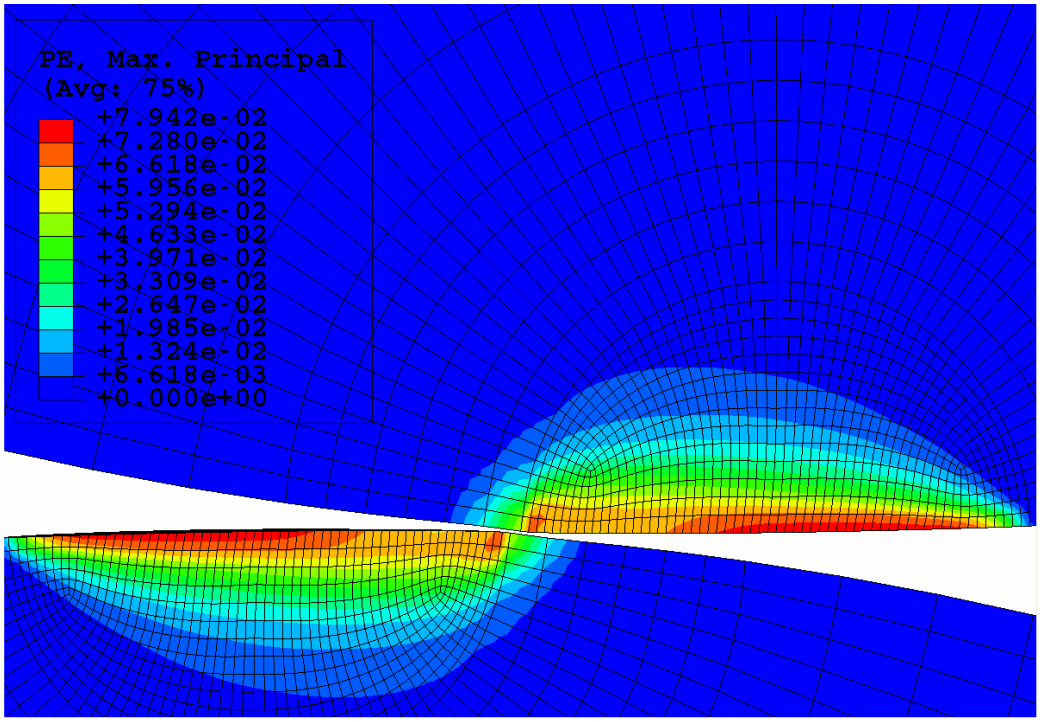

(b)

Figure 29: Residual plastic strains in $2\omega_c$ (a) and $15\omega_c$ (b) at the completion of sliding for steel-on-steel contact

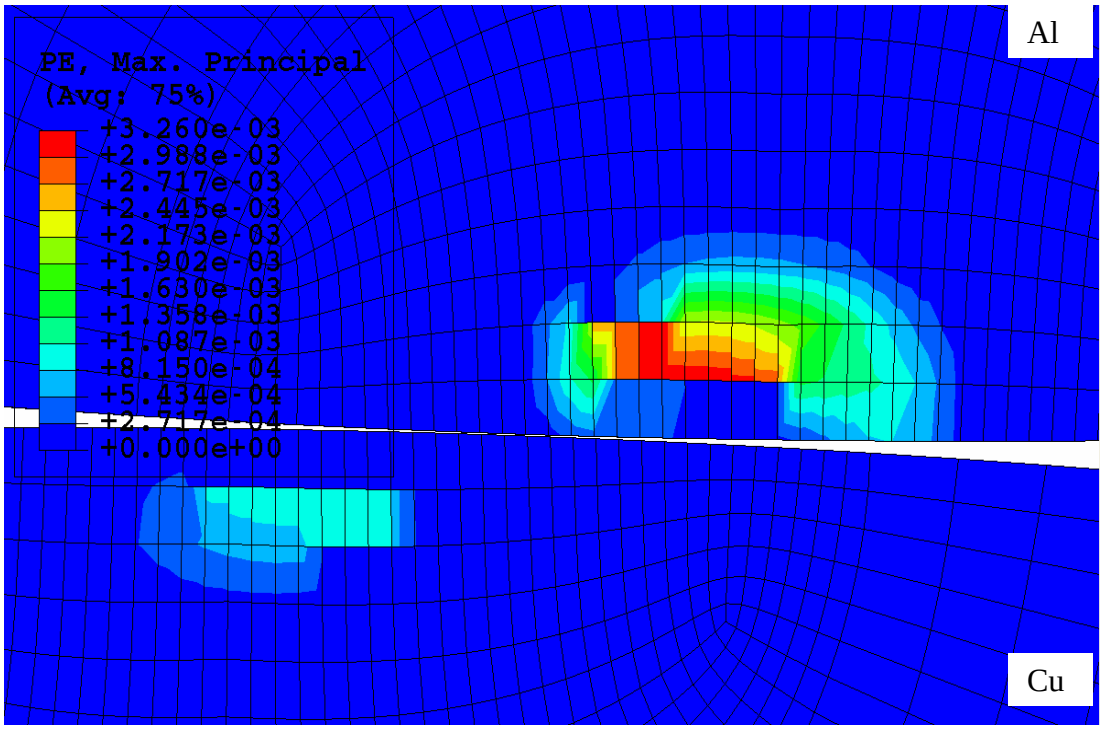

(a)

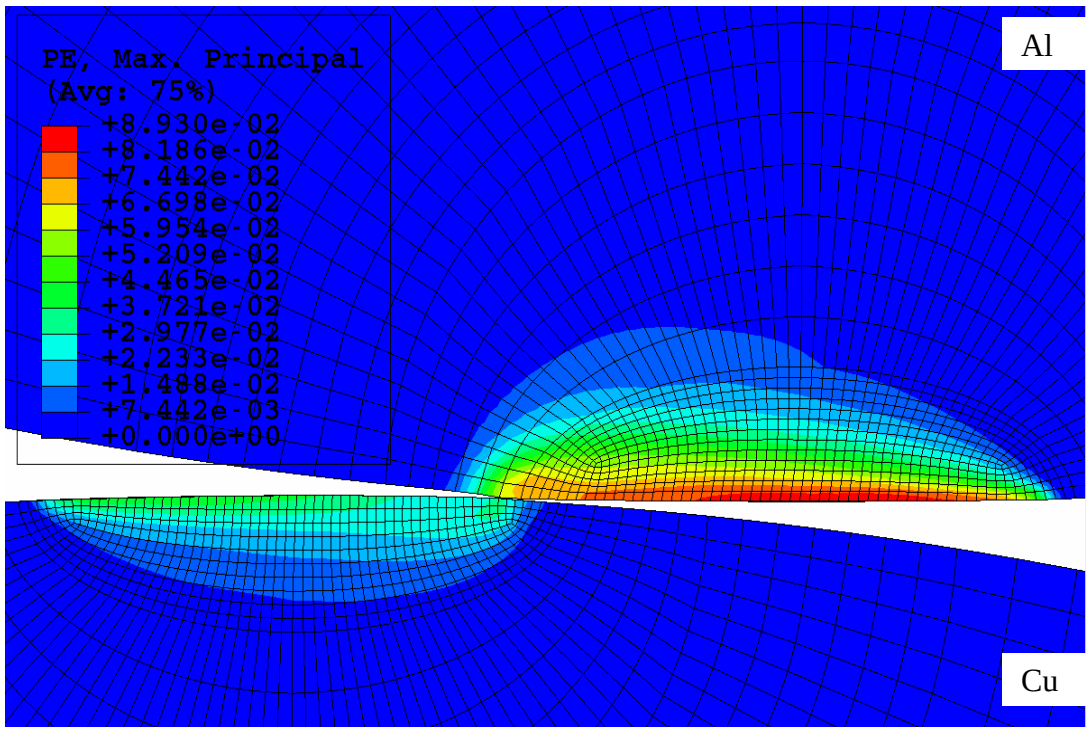

(b)

Figure 30: Residual plastic strains in $2\omega_c$ (a) and $15\omega_c$ (b) at the completion of sliding for aluminum-on-copper contact

4.2. Forces

The method presented in section 3.2 is used to monitor the forces as sliding progresses in the frictional sliding cases. Figures 31 and 32 present the normalized horizontal reaction forces for the preset vertical interferences studied here as sliding progresses for steel-on-steel contact and aluminum-on-copper contact, respectively. The normalized vertical reaction forces for steel-on-steel contact and aluminum-on-copper contact are presented in Figures 33 and 34, respectively. All these reaction forces are normalized by the critical load, P_c, as defined previously in Eq. (1).

As sliding begins, the horizontal forces start from zero and increase in magnitude to a maximum value then begin to decrease before the hemispheres are vertically aligned ($x/R = 0$). As shown in Figures 31 and 32, unlike the frictionless sliding cases, the lower interference cases show a nearly symmetric pattern about the x/R axis and are completely negative. As the interference increases, the maximum force occurs progressively earlier in the progression of sliding. This can be attributed to an earlier initiation of plasticity and an increase in the volume of plastically yielded material that is tugged forward as the interference increases. Similar trend can be seen in the vertical reaction forces, as shown in Figures 33 and 34. The magnitude of the vertical reaction forces, though are much higher in magnitude than the horizontal reaction forces.

It should be noted that the critical load, P_c, normalizes both the vertical and horizontal reaction forces well for both material combinations as the maximum normalized reaction forces are nearly identical for both material combinations.

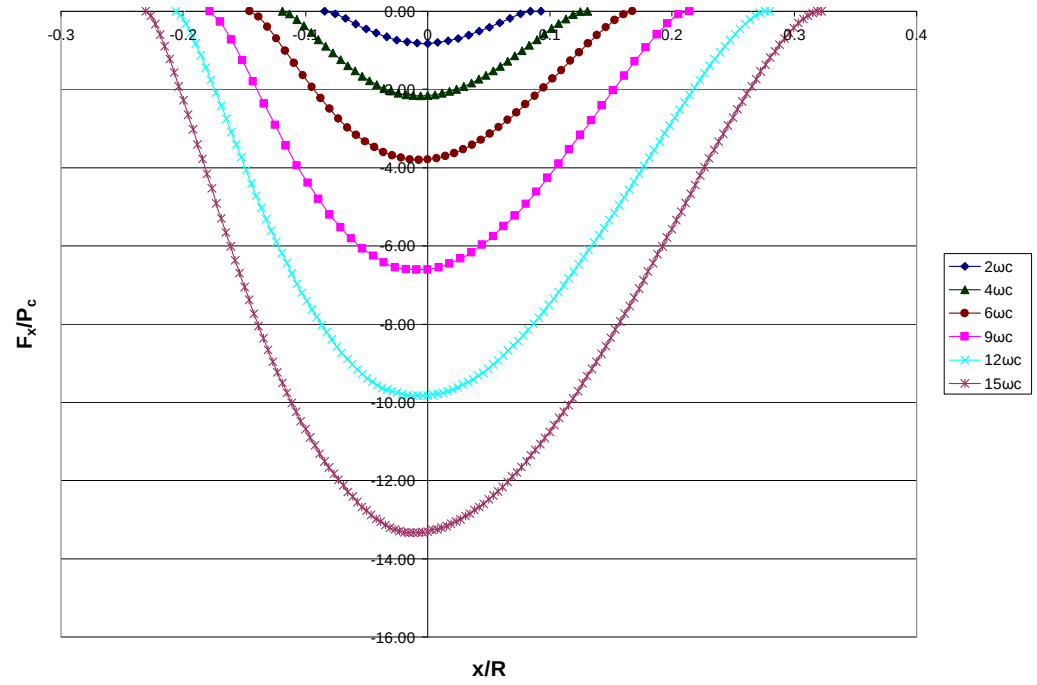

Figure 31: The normalized horizontal reaction forces as sliding progresses for steel-on-steel contact.

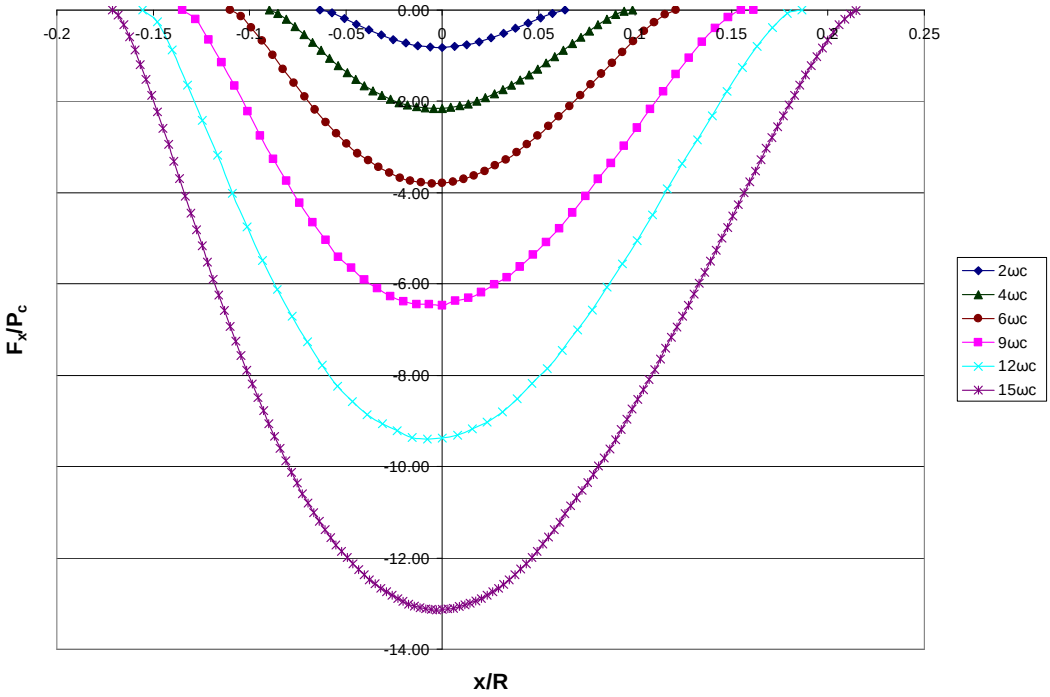

Figure 32: The normalized horizontal reaction forces as sliding progresses for aluminum-on-copper contact.

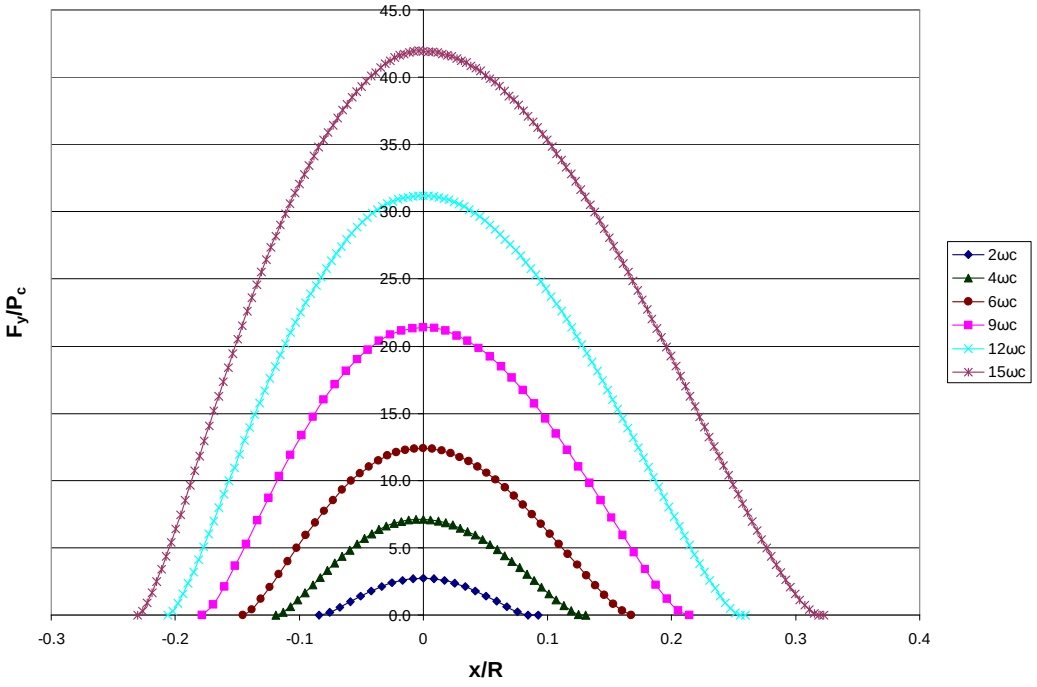

Figure 33: The normalized vertical reaction forces as sliding progresses for steel-on-steel contact.

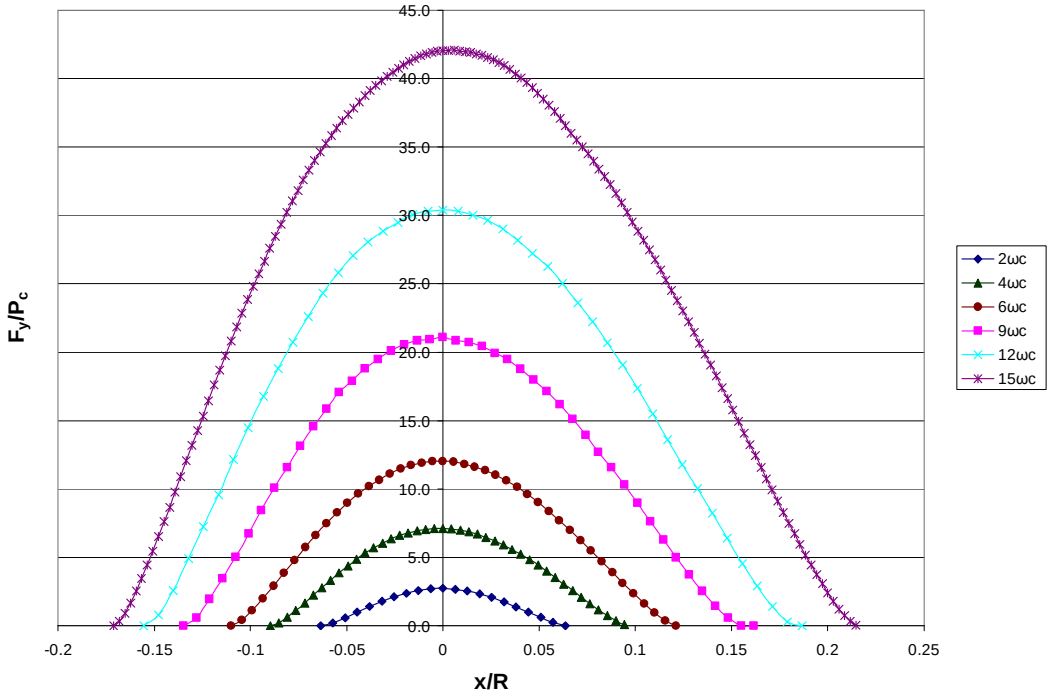

Figure 34: The normalized vertical reaction forces as sliding progresses for aluminum-on-copper contact.

A "load ratio" is defined as F_x/F_y, being the ratio of the horizontal reaction force with respect to the vertical reaction force, in order to better understand the resistance to sliding due to the mechanical interference. While each of the data points on these curves can be thought of as qualitatively similar to the instantaneous local coefficient of friction, it is emphasized that this is not a coefficient of friction in the traditional sense since but rather a combination of the imposed coefficient of friction and the mechanical interference to sliding. This ratio is generated and plotted versus the normalized sliding distance as shown in Figures 35 and 36 for steel-on-steel and aluminum-on-copper, respectively.

It can be seen that the maximum magnitude of the "load ratio" increases steadily as the preset vertical interference increases. The load ratio increases as more plasticity is initiated as plasticity is increased because more plasticity results in a reduced load carrying capacity of the hemisphere. The load ratio also increases as the hemispheres are coming out of contact because the portions of the hemispheres that are still elastic can still impose an elastic rebound force.

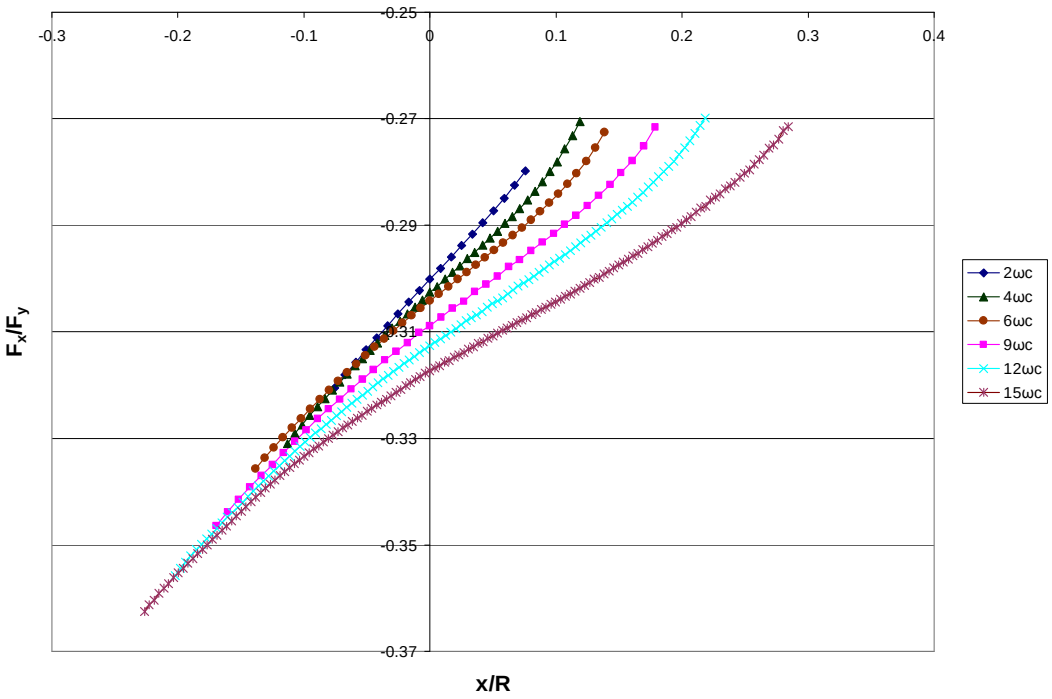

Figure 35: The "load ratio" as sliding progresses for $2\omega_c$ through $15\omega_c$ for steel-on-steel contact.

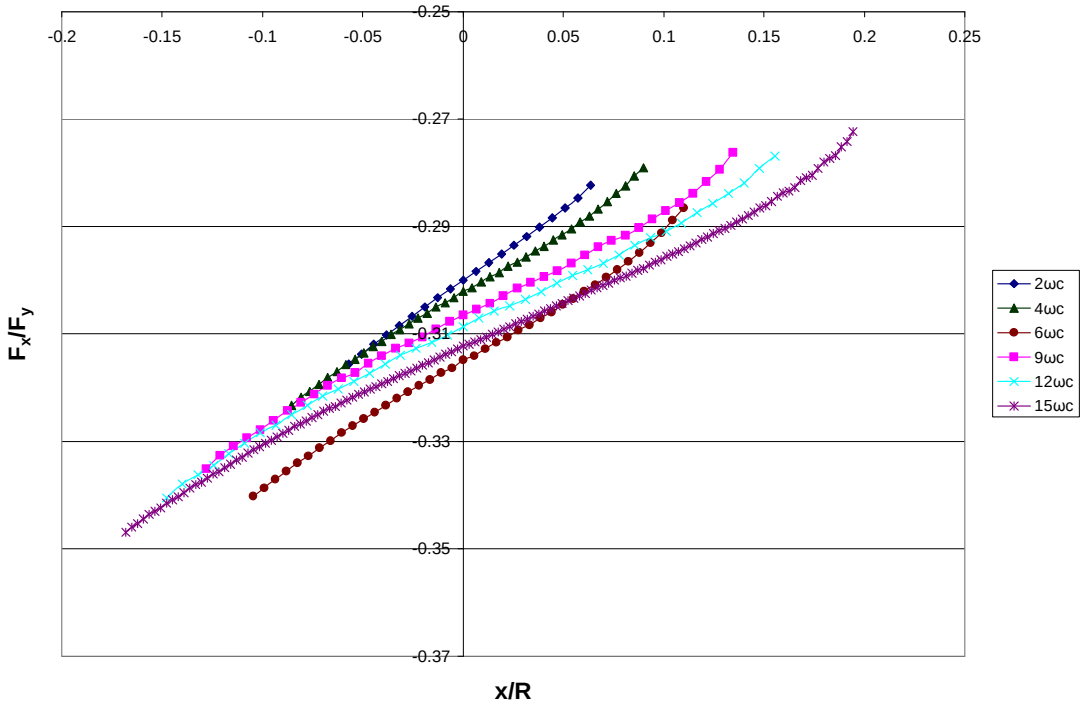

Figure 36: The "load ratio" as sliding progresses for $2\omega_c$ through $15\omega_c$ for aluminum-on-copper contact.

4.3. Energy Loss

The net energy loss in frictional sliding, U_{net}, can be calculated the same way as in section 3.3 for frictionless sliding by using Eq. (9). Figure 37 shows the plot of U_{net}/U_c for each of the preset vertical interferences, ω^* for steel-on-steel and aluminum-on-copper contact. As interference increases, progressively more energy is lost to plasticity resulting from the higher mechanical interferences as well as the added shear traction resulting from the non-conservative nature of friction. A second order polynomial curve is then fitted to the numerical data. It represents the trend followed by energy loss for the range of the applied vertical interference, ω^*, and is found to closely capture the increasing energy loss with increasingly elastic-plastic loading. The fitted equation is:

$$\frac{U_{net}}{U_c} = 27.294\omega^* + 118.146\omega^{*2} \qquad \omega^* \geq 0 \tag{18}$$

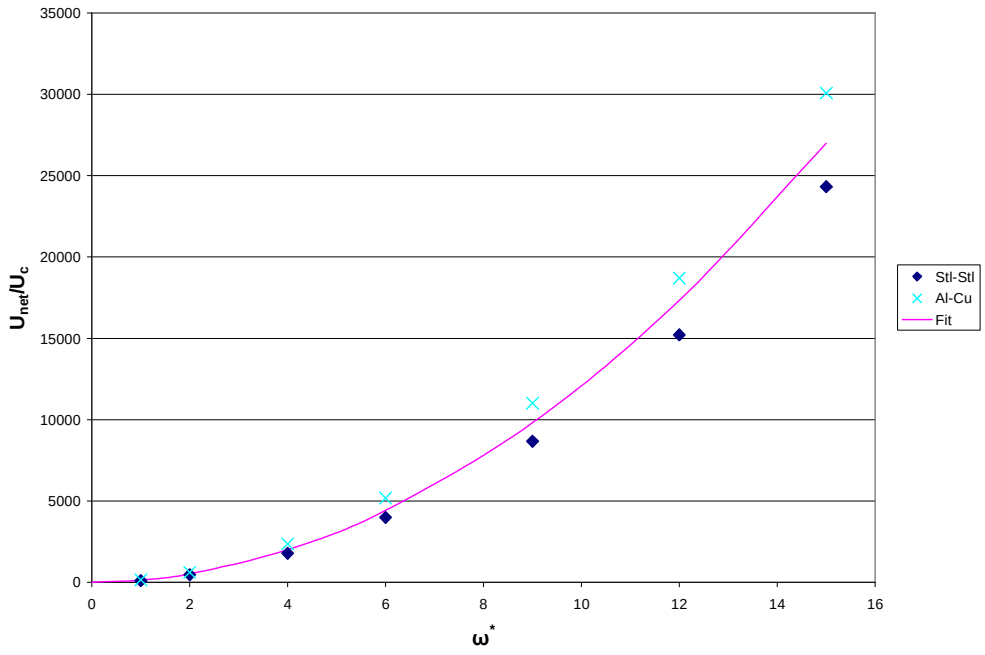

Figure 37: Normalized net energy loss versus preset interference.

4.4. Effective Coefficient of Friction

An effective coefficient of friction, $\overline{\mu}$, as defined in Eq. (14), is also used to capture the net energy loss due to plasticity in frictional sliding. Figure 38 presents $\overline{\mu}$ versus preset vertical interference. As shown in the figure, the effective coefficient of friction increases as vertical interference increases. In the elastic domain (ω^*<1) the effective coefficient of friction is the imposed coefficient of friction, 0.3 in this case. As the interference increases and more plastic deformation occurs, the effective coefficient of friction increases. In the steel-on-steel contact case $\overline{\mu}$ increases faster than in the aluminum-on-copper contact.

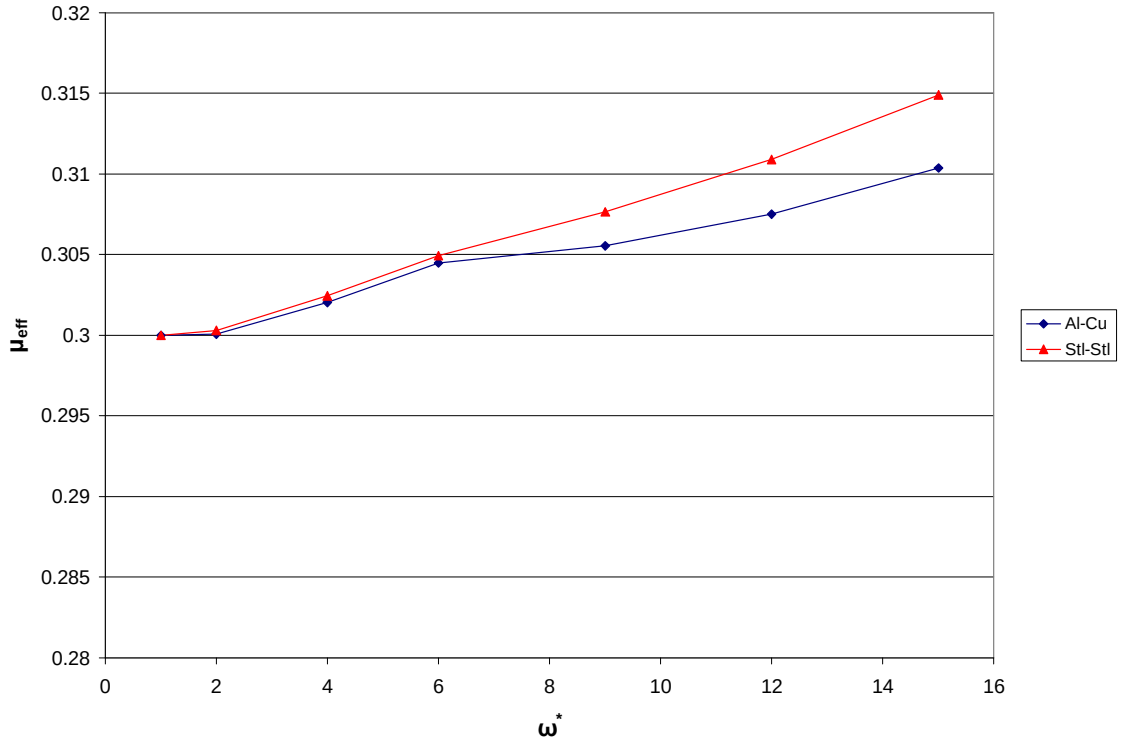

Figure 38: The effective coefficient of friction versus preset vertical interference.

4.5. Contact Area

The contact area in frictional sliding is also investigated. Figures 39 and 40 present a plot of the contact area, normalized by the critical contact area, A_c, versus normalized sliding distance, x/R. For small vertical interferences the contact area shows a nearly symmetric pattern. As interference increases, the location of maximum contact occurs progressively earlier in the progression of sliding. It is also of note that the maximum values are nearly the same for both material combinations suggesting the normalization scheme used is effective.

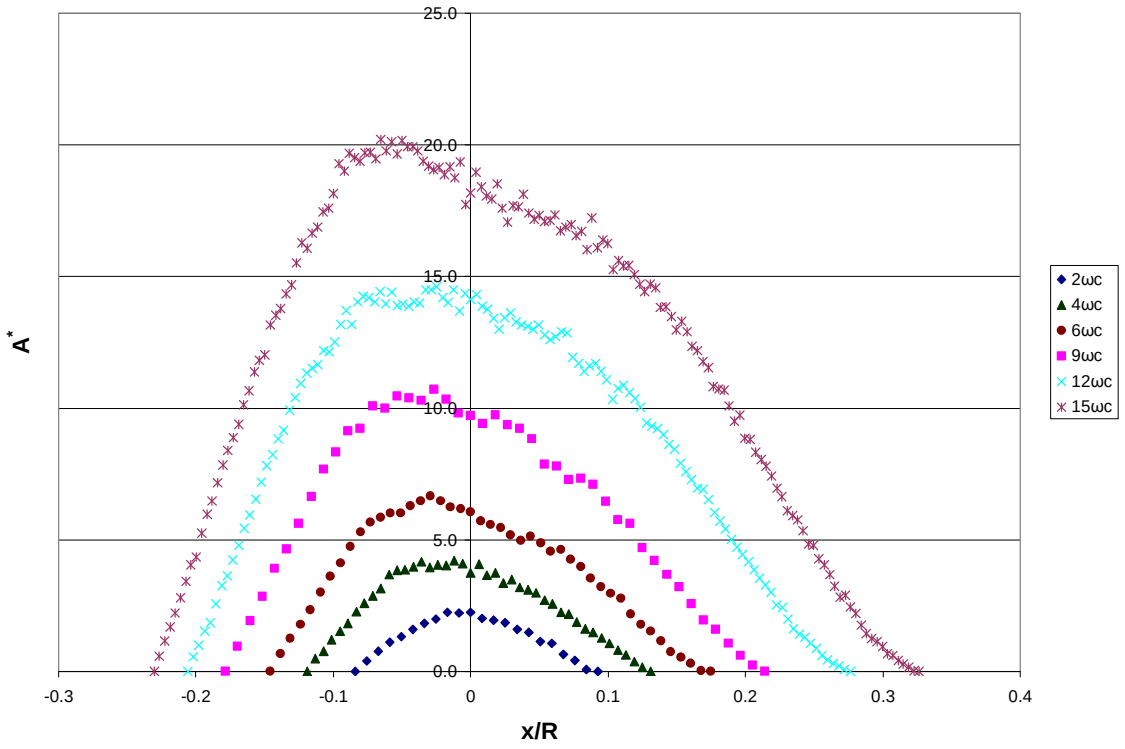

Figure 39: Contact areas for $2\omega_c$ through $15\omega_c$ for steel-on-steel contact.

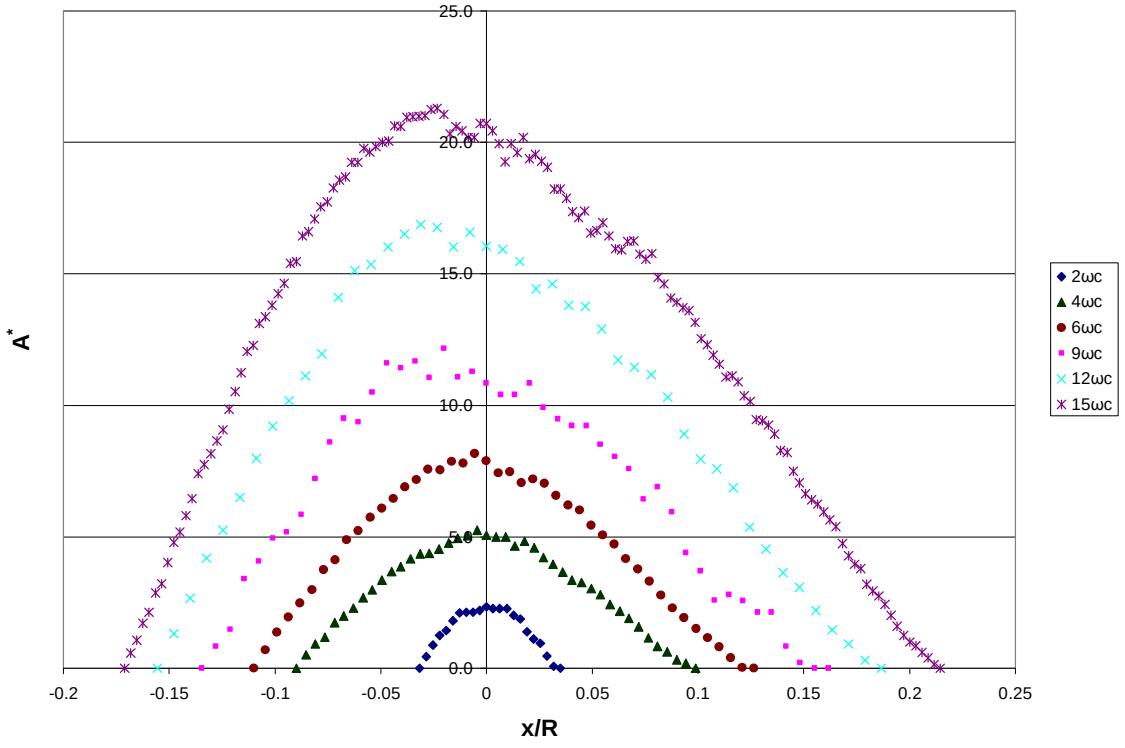

Figure 40: Contact areas for $2\omega_c$ through $15\omega_c$ for aluminum-on-copper contact.

4.6. Deformations

The resulting deformations in the hemispheres as sliding progresses are studied in this analysis as well. Figure 41 presents the maximum deformation in the hemispheres as sliding progresses for steel-on-steel contact. As shown in the figure, the deformation increases to a maximum value past the point of vertical alignment and then decreases until the hemispheres come out of contact.

Once the hemispheres have come out of contact there is residual deformation due to the plastic deformation. This can be seen in Figure 41 as the flat portion at the end of the deformation curves. The simulation is run past the point when the hemispheres come out of contact to capture this phenomenon. Figure 42 presents a plot of the residual deformations, u_{res}, normalized by the critical interference, ω_c versus preset vertical interference, ω^*. The residual deformations dramatically increase as the interference increases. A polynomial curve fit that closely approximates the data is given by:

$$\frac{u_y}{\omega_c} = 0.205(\omega^* - 1) + 0.017(\omega^* - 1)^2 \qquad 1 \le \omega^* \le 15 \qquad (19)$$

It should be noted that the residual deformation after sliding at an interference equal to the critical interference is not zero for frictional sliding, but is negligible for the two material combinations presented here.

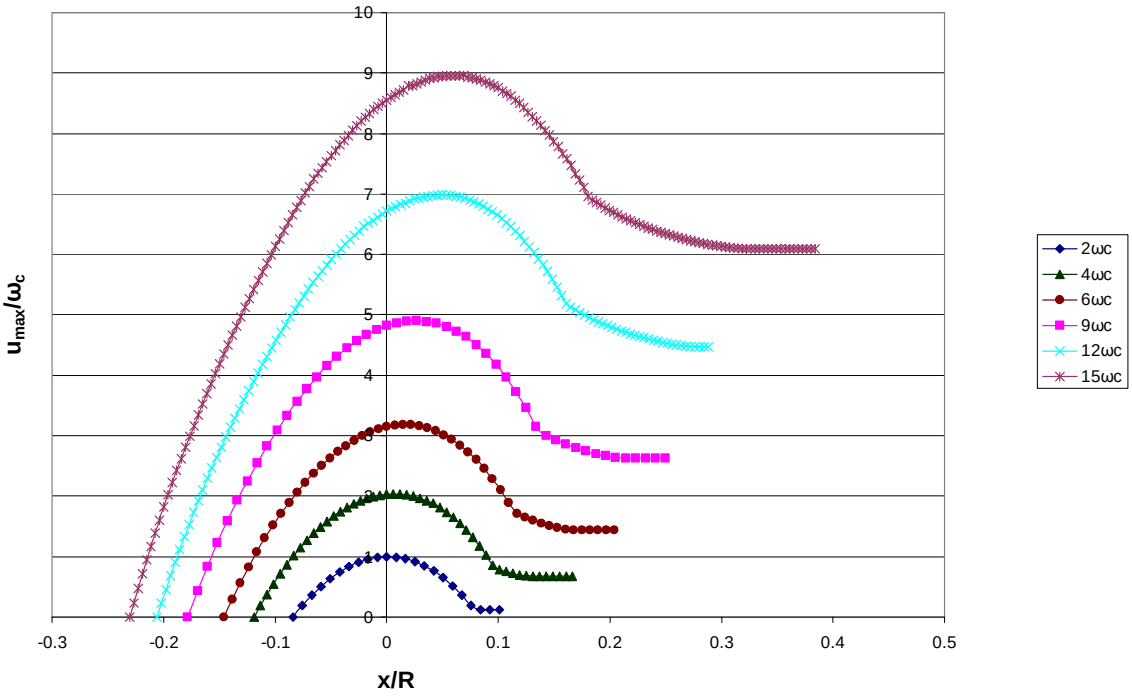

Figure 41: Normalized deformation as sliding progresses for steel-on-steel contact.

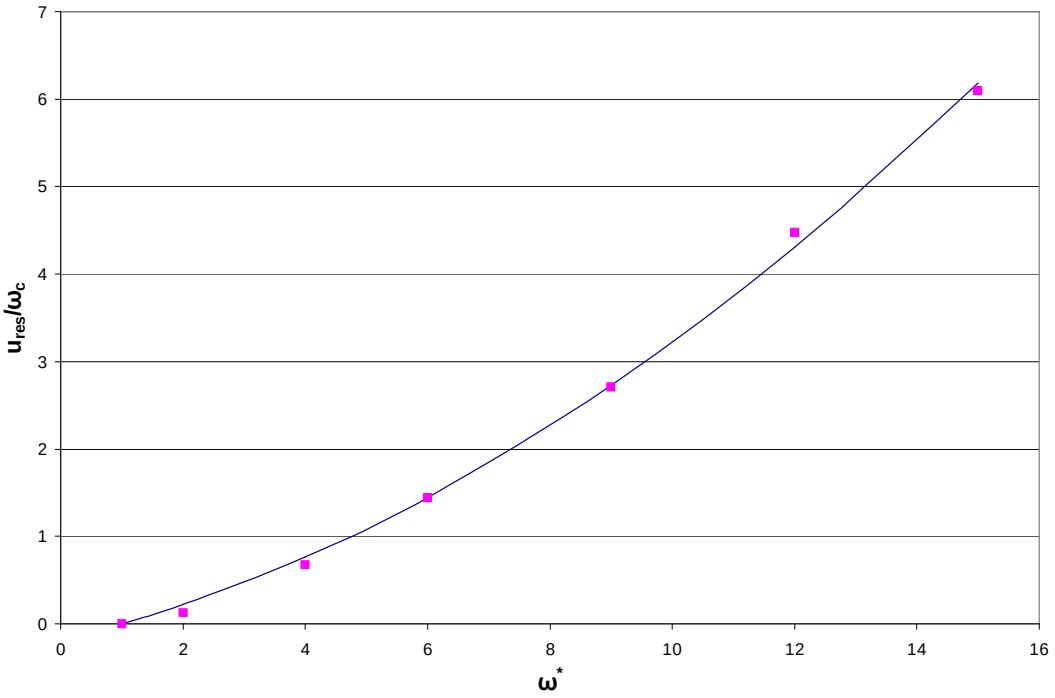

Figure 42: Normalized residual deformations versus preset interference for steel-on-steel contact.

Since in the aluminum-on-copper cases the contact is between two different materials, the upper and lower hemispheres will deform differently based on their respective material properties. Figures 43 and 44 present, respectively, the deformation in aluminum and copper as sliding progresses for the interferences studied. As shown in the figures, the aluminum deforms over twice as much as the copper, due to its lower yield strength, as shown in Table 1. Qualitatively, though they show a similar trend to each other as well as the steel.

The residual deformations in both the aluminum and copper are presented in Figure 45. The aluminum results are qualitatively similar to the steel results, but the copper shows much less residual deformation than the aluminum. This is due to the fact that the copper has a higher yield strength than the aluminum and the aluminum will absorb most of the deformation. A polynomial curve fit that closely approximates the data for copper is given by:

$$\frac{u_y}{\omega_c} = 0.098(\omega^* - 1) + 0.008(\omega^* - 1)^2 \qquad 1 \le \omega^* \le 15 \qquad (20)$$

and for aluminum is given by:

$$\frac{u_y}{\omega_c} = 0.335(\omega^* - 1) + 0.014(\omega^* - 1)^2 \qquad 1 \le \omega^* \le 15 \qquad (21)$$

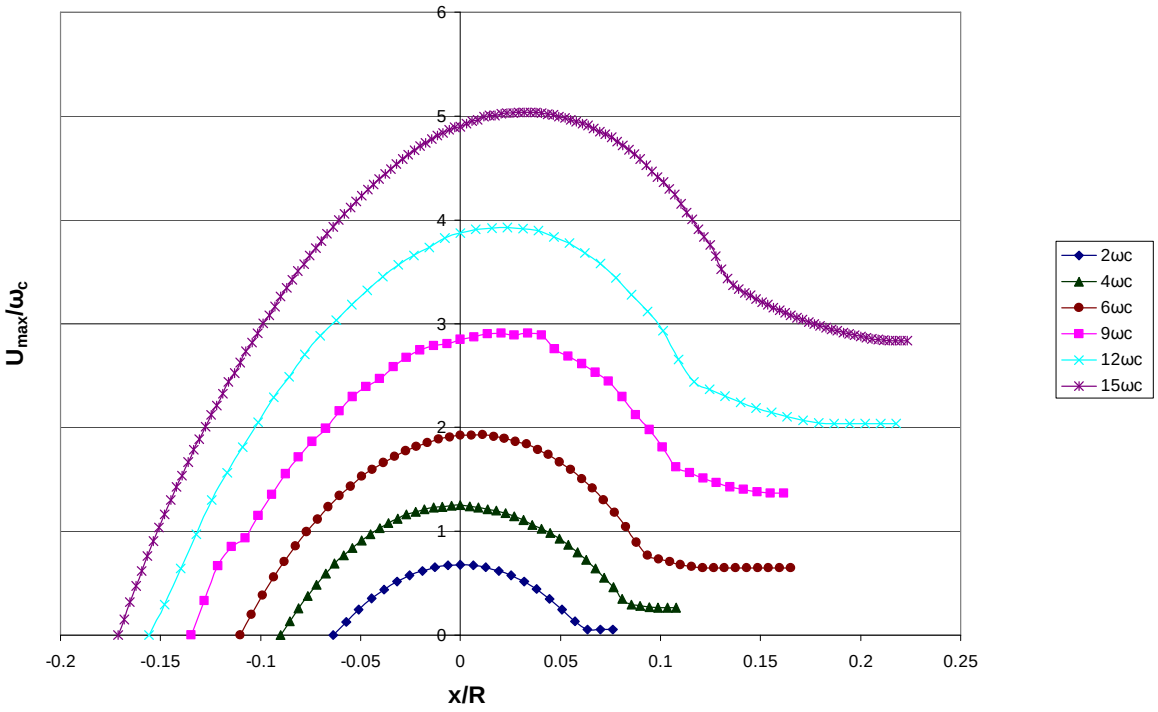

Figure 43: Normalized deformation in copper as sliding progresses.

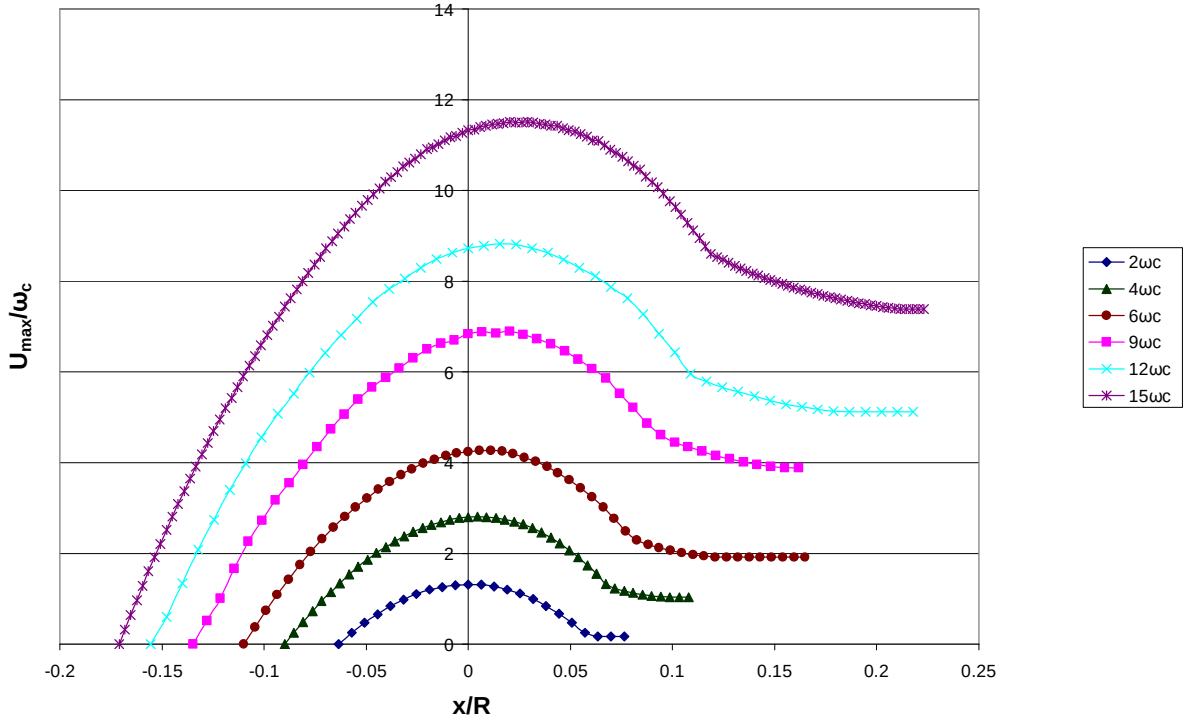

Figure 44: Normalized deformation in aluminum as sliding progresses.

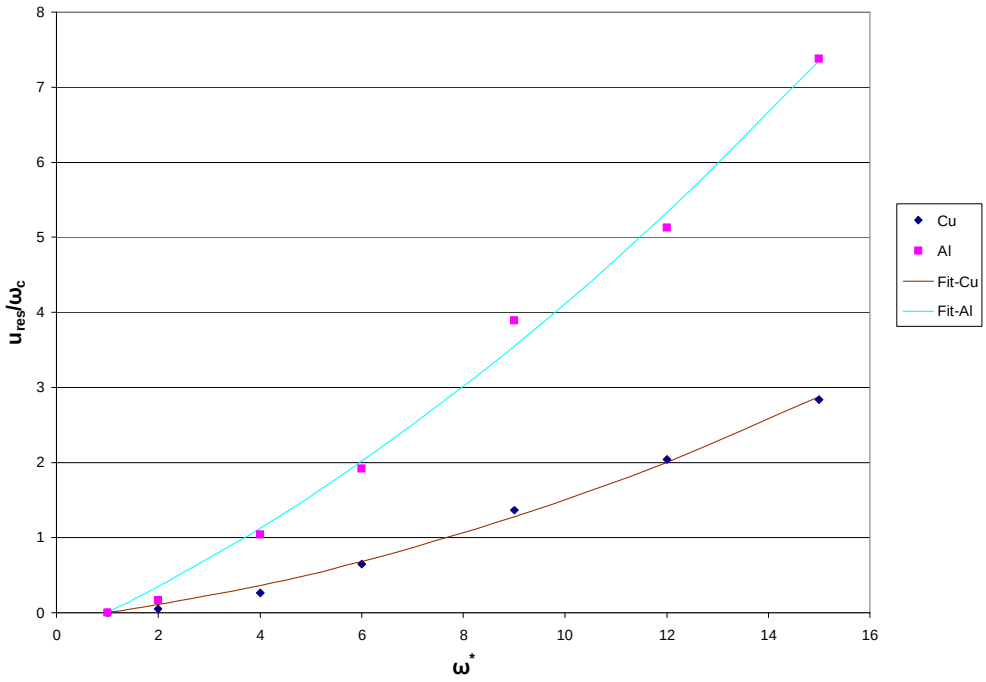

Figure 45: Residual deformations versus preset interference for aluminum-on-copper contact.

4.7. Conclusions

The results of the FEA of frictional sliding in the elastic-plastic domain between two hemispheres are discussed. Results are presented for sliding between two steel hemispheres and between an aluminum and a copper hemisphere. The resultant parameters such as deformations, forces, stresses, and energy losses that occur are presented and explained. All the results are presented nondimensionally in order to apply to hemispherical contact at any scale. The development and propagation of stress in the hemispheres as sliding progresses is discussed. It is found that as the interference increases, the stresses in the hemispheres expand and reach the surface at values above the yield strength due to the addition of strain hardening to the material model. It is also found that the residual von Mises stress are below the yield strength. Residual plastic strains are discussed and as interference increases the residual plastic strained volume

expands and eventually covers the whole contact region. A single set of equations is derived to characterize the energy loss due to plastic deformation for both material combinations because the magnitudes of the net energy at the end of sliding are similar. An effective coefficient of friction is introduced in order to help quantify the added contribution of plasticity. This effective coefficient of friction increases faster in steel-on-steel sliding than in aluminum-on-copper sliding. Equations to characterize residual deformations in steel-on-steel contact and aluminum-on-copper contact are derived. It is shown that aluminum shows more deformation than copper throughout the progression of sliding. Contact areas during sliding are presented and it is also found that the normalized dimensions of the contact region are larger in aluminum-on-copper contact.

CHAPTER V: COMPARISON OF FRICITONAL AND FRICITONLESS SLIDING

In this section comparisons are drawn between frictional and frictionless sliding for each of the result parameters that are discussed in the previous sections. Figures in this section present results only for vertical interference values of ω^* = 9, 12 and 15 for clarity. This helps compare the effects of sliding with a mechanical interference and the combined effect of sliding with an imposed friction coefficient and an imposed mechanical interference.

5.1. Stresses

Stress formations and residual stresses in sliding are of the highest interest as they help in predicting the region of yield and subsequent failure. For frictionless sliding, representative von Mises stress contour plots are shown in Figures 3 through 6, while Figures 25 through 28 capture the development of stresses for frictional sliding between two hemispheres for the two extreme cases in this analysis ($2\omega_c$ and $15\omega_c$). One of the most significant differences between frictionless and frictional sliding in the stress contours at the point of vertical alignment is the axis of symmetry for the stress pattern. For the frictionless sliding cases, the stress field in the two sliding steel hemispheres is mirrored about the horizontal contact interface. However, for frictional sliding the stress fields that develop during the course of sliding are tilted in a direction that is opposite to the direction of sliding.

Another major difference in frictional and frictionless sliding is the size of the plastic core during sliding. For instance, in the $2\omega_c$ steel-on-steel case the plastic core is completely inside the hemisphere for frictionless sliding while it is larger and has reached

the surface in the frictional sliding case (see Figure 3 (a) and 25 (a)). A similar trend is seen in aluminum-on-copper sliding.

Finally, it is important to note that the residual stresses in frictional sliding are lower than in frictionless sliding. In frictionless sliding the maximum residual stresses are at the yield strength for the highest interference cases. Whereas in frictional sliding, the maximum residual stresses have reduced well below the yield strength.

5.2. Forces

Figures 46 through 49 show the normalized horizontal reaction force and normalized vertical reaction force for both steel-on-steel and aluminum-on-copper comparing the frictionless and frictional sliding results.

In studying Figures 46 and 47, it can be seen that the vertical reaction force follow the same general trend. However, the maximum forces occur earlier in the frictionless sliding cases than in the frictional sliding cases, but the latter has higher maximum values. Also, the hemispheres stay in contact longer with friction present. This is due to the additional tugging action that friction contributes. Note, in fact, that the frictional $12\omega_c$ case stays in contact longer than the frictionless $15\omega_c$ case. The maximum magnitude of the vertical reaction force is larger for the frictional sliding cases as well.

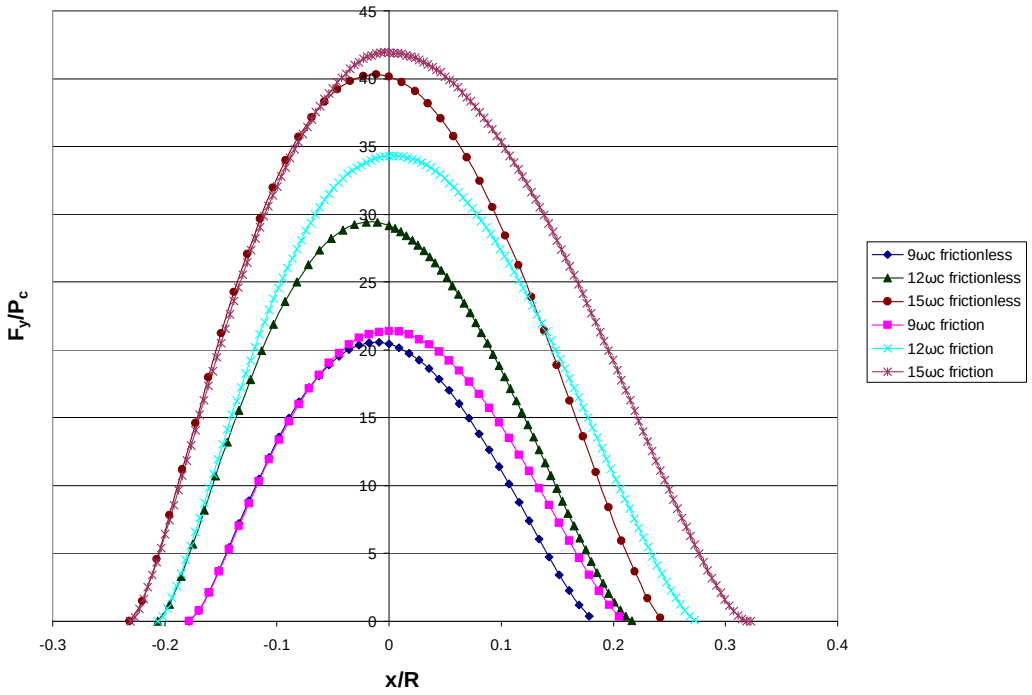

Figure 46: A comparison of the vertical reaction force for steel-on-steel frictional and frictionless sliding.

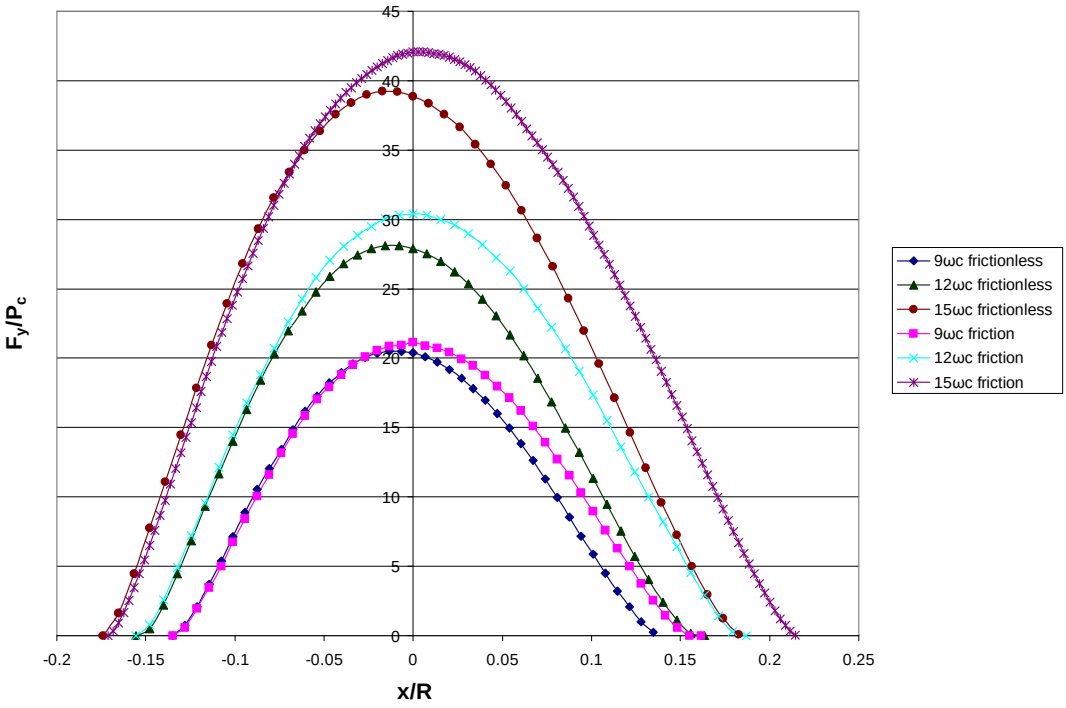

Figure 47: A comparison of the vertical reaction force for aluminum-on-copper frictional and frictionless sliding.

In studying the horizontal reaction force curves, Figures 48 and 49, it can be seen that the reaction forces for the frictional sliding cases are completely negative due to the increased opposition to sliding the friction coefficient imposes masking the effects of the positive elastic rebound force, while in the frictionless sliding cases this elastic rebound force is evident. Also of note is the much higher magnitude of the horizontal reaction force values in the frictional sliding cases. This added shear traction contributes to the larger volume of the plastic core in the frictional sliding cases and helps explain why yielding regions reach the surface much sooner.

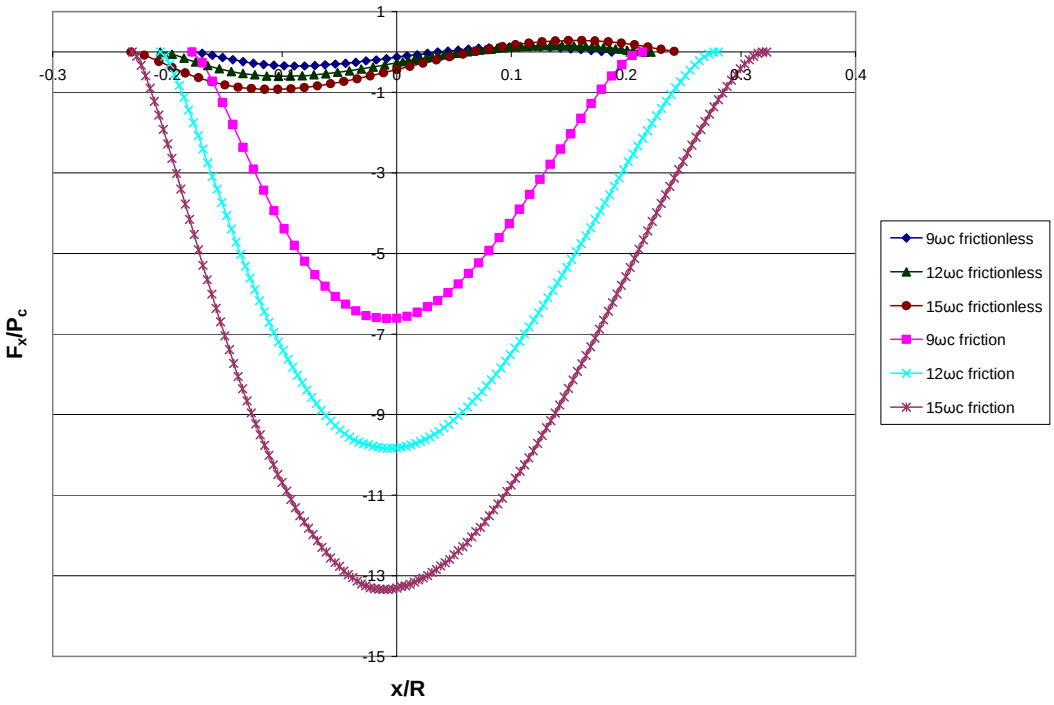

Figure 48: A comparison of the horizontal reaction force for steel-on-steel frictional and frictionless sliding.

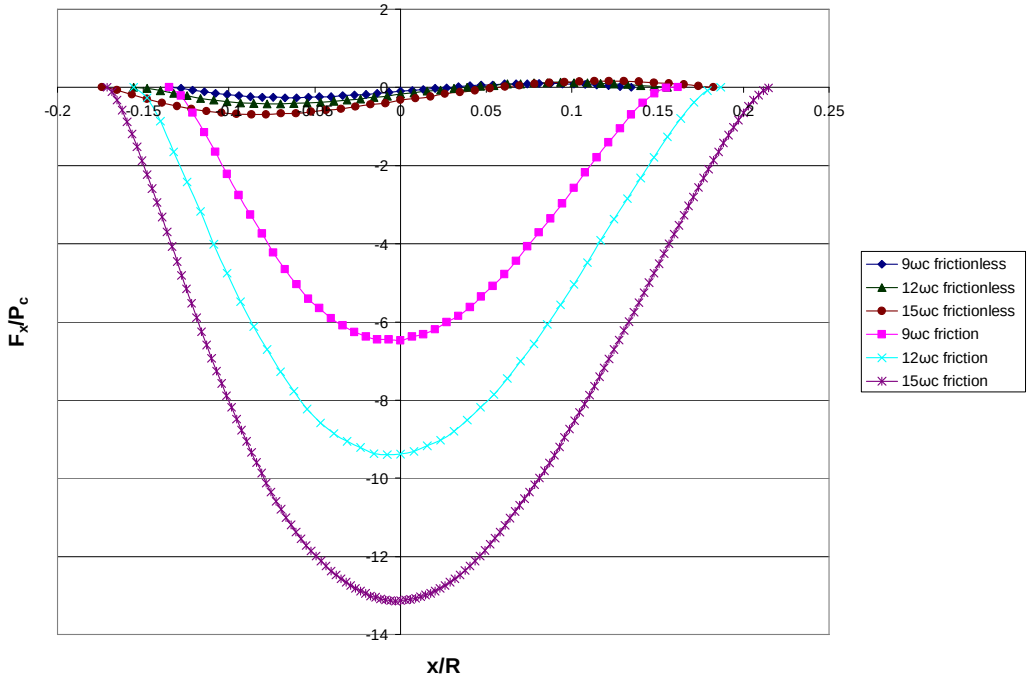

Figure 49: A comparison of the horizontal reaction force for aluminum-on-copper frictional and frictionless sliding.

5.3. Energy Loss

Comparisons of the net energy loss for frictional and frictionless sliding yield very different results. Figure 50 shows the fitted equations for the net energy loss for both frictionless and frictional sliding. The net energy loss is much higher in frictional sliding due to the non-conservative nature of friction and the increase in plasticity brought about by the added shear traction.

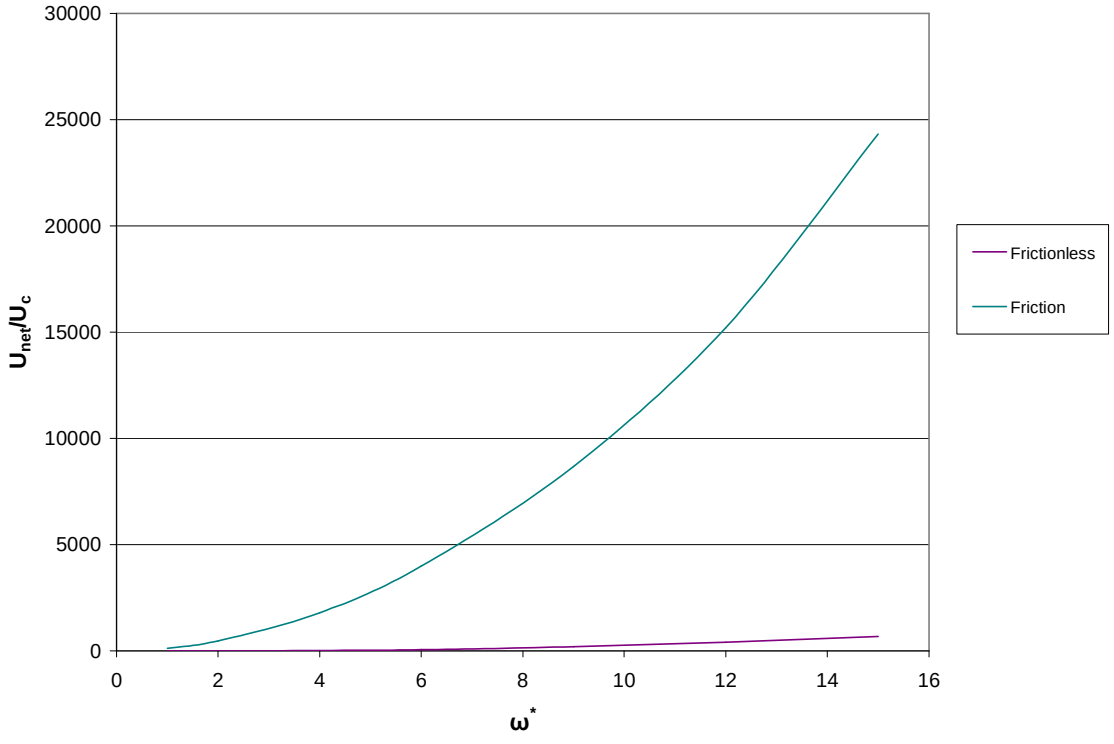

Figure 50: A comparison of the energy loss in steel-on-steel frictionless and frictional contact.

5.4. Effective Coefficient of Friction

In order to better compare the effects of plasticity brought about by a friction coefficient, the effective coefficient of friction is compared. Figure 51 presents the effective coefficient of friction for both frictionless and frictional sliding for steel-on-steel and aluminum-on-copper contact. It is important to note that the assigned coefficient of friction (μ=0.3) is subtracted from the effective coefficient of friction for frictional sliding cases in order to make an euqitable comparison. The effective coefficient of friction for each material combination is close for the lower interference cases and as the interference increases it can be seen that the addition of a friction coefficient to the sliding process increases the plasticity. This can be seen by the divergence of the frictional and frictionless cases as interference increases when comparing a material combination. It can be seen that as interference increases the $\overline{\mu}$ curve begins to flatten out in the frictionless cases. On the other hand, the slope of the $\overline{\mu}$ curve begins to increase as interference increases in frictional sliding.

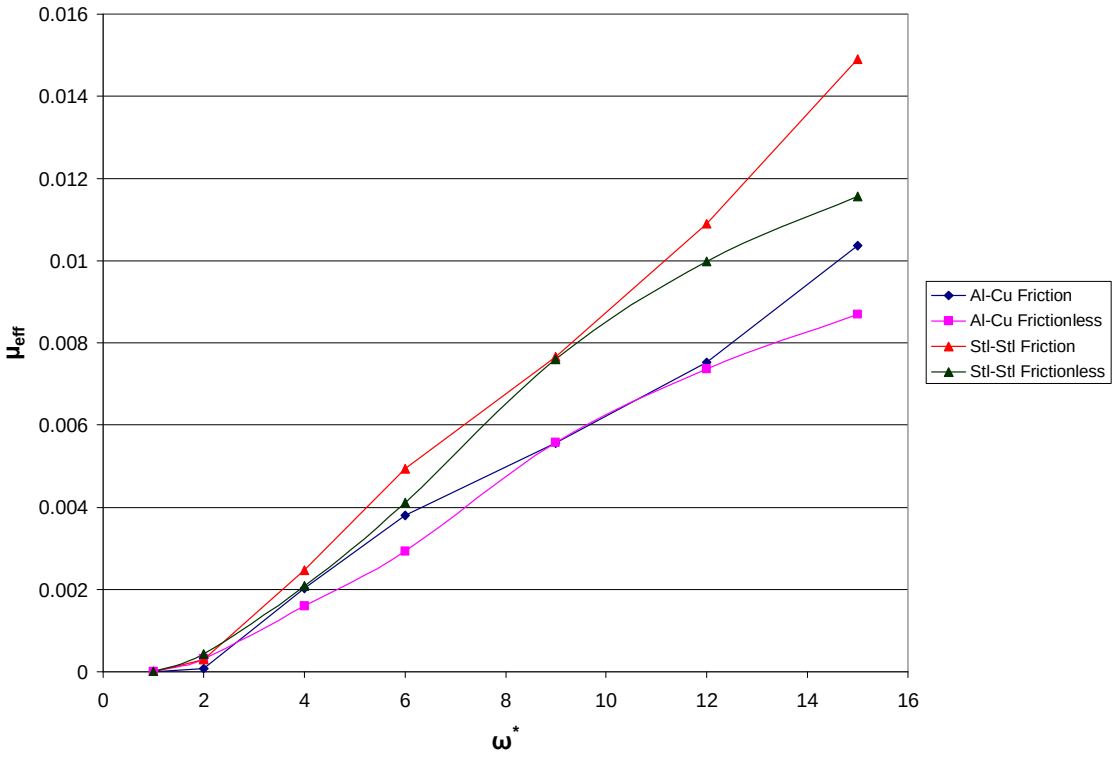

Figure 51: A comparison of the effective coefficient of friction for frictionless and frictional sliding.

5.5. Contact Area

Figures 52 and 53 present the frictionless and frictional comparisons of the contact area as sliding progresses for steel-on-steel and aluminum-on-copper contact, respectively. As the preset interference increases, the difference in contact area increases at a given sliding location. For instance, the contact areas at vertical alignment for $9\omega_c$ cases are much closer than the contact areas for $15\omega_c$ cases at vertical alignment. These figures clearly show that the hemispheres stay in contact longer when friction is present. Also, the contact areas for frictional and frictionless contact show a similar trend initially, but as plastic deformation becomes significant the contact area is larger for frictional contact.

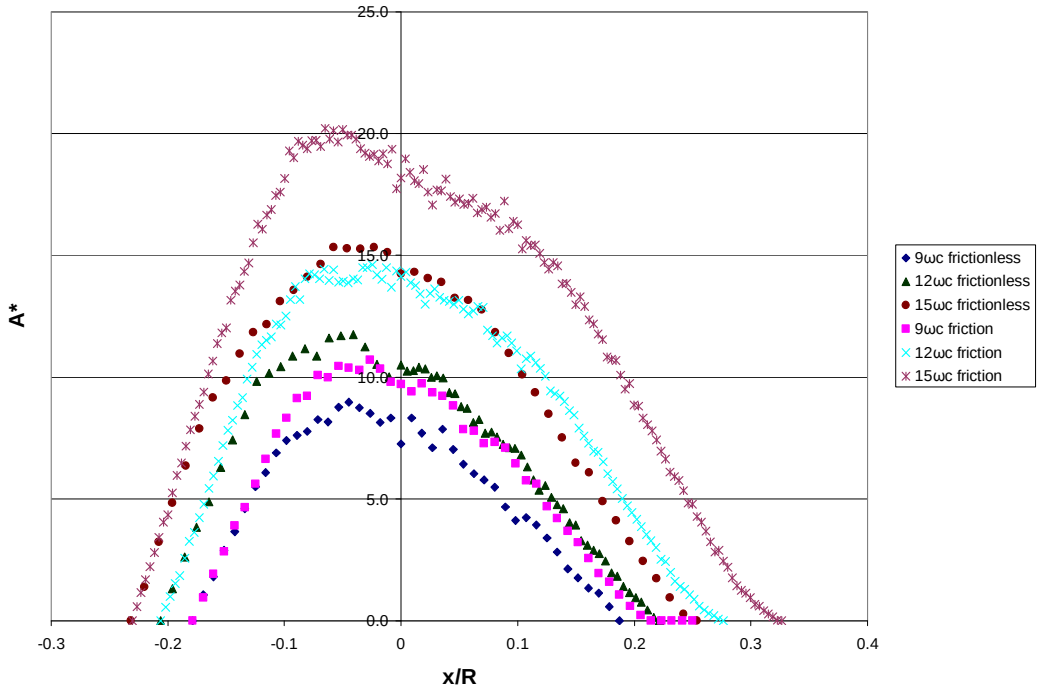

Figure 52: A comparison of the contact areas as sliding progresses for steel-on-steel contact for frictional and frictionless contact.

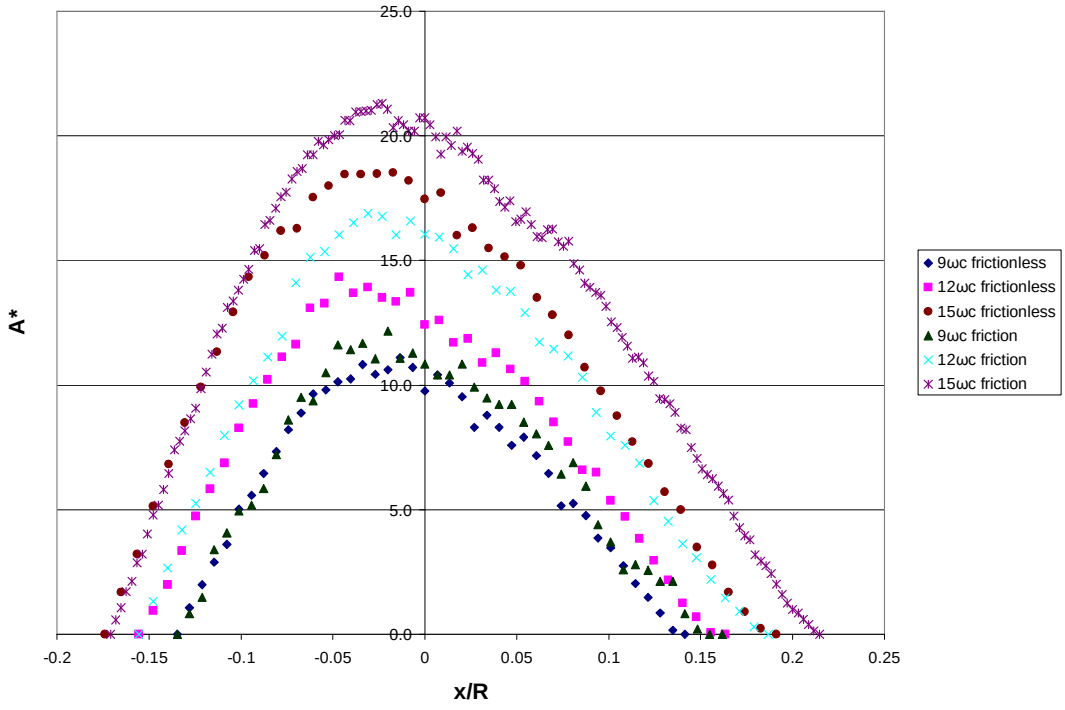

Figure 53: A comparison of the contact areas as sliding progresses for aluminum-on-copper contact for frictional and frictionless contact.

5.6. Deformations

A comparison of the maximum deformations in the hemispheres as sliding progresses for frictional and frictionless contact is presented in Figures 54 through 56. For the steel-on-steel case, as shown in Figure 50, the frictional sliding cases show more deformation and the difference between frictional and frictionless cases increase as the preset interference increases. Also, the point of maximum interference occurs progressively later in the frictional sliding case as interference increases. This suggests that frictional tugging contributes not only to the magnitude of the maximum deformation but also its location in the progression of sliding.

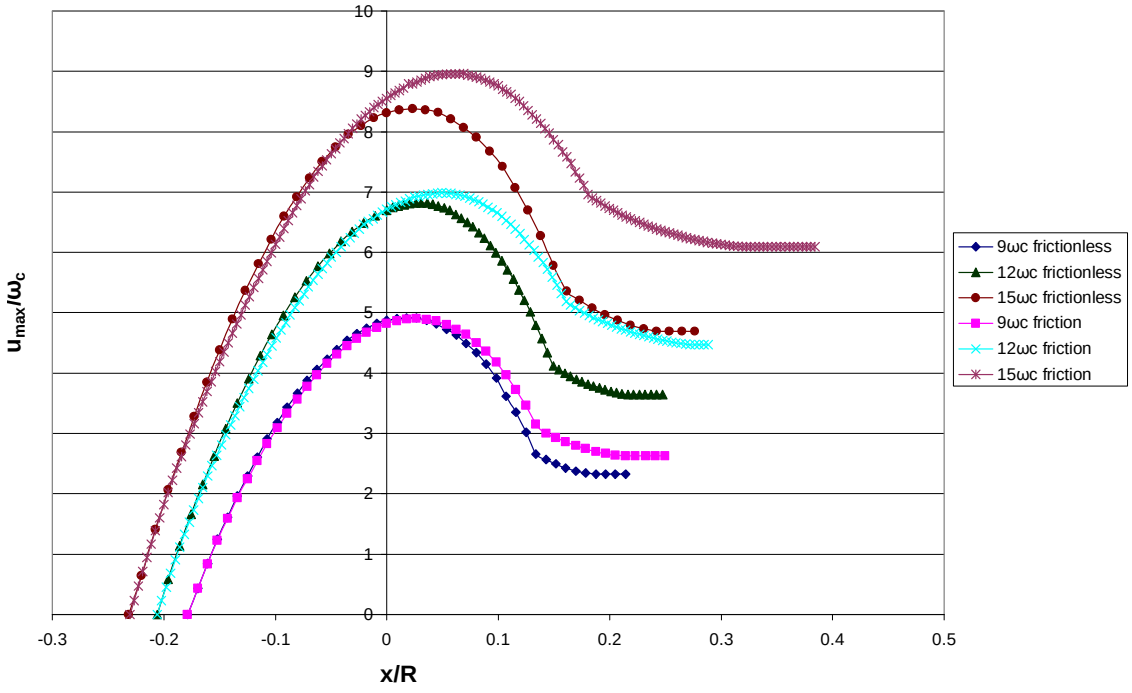

Figure 54: A comparison of the deformation as sliding progresses for frictional and frictionless steel-on-steel contact.

Expectedly, the copper and aluminum spheres behave differently with regard to deformation. Figure 55 presents the maximum deformation as sliding progresses for copper frictional and frictionless contact. As shown, the frictionless cases show a higher maximum deformation that occurs earlier in the progression of sliding than in the frictional cases. The residual deformation, however, is higher for the frictional sliding cases. On the other hand, the aluminum, as shown in Figure 56, displays a higher maximum deformation in the frictional sliding cases as well as more residual deformation than in the frictionless sliding cases.

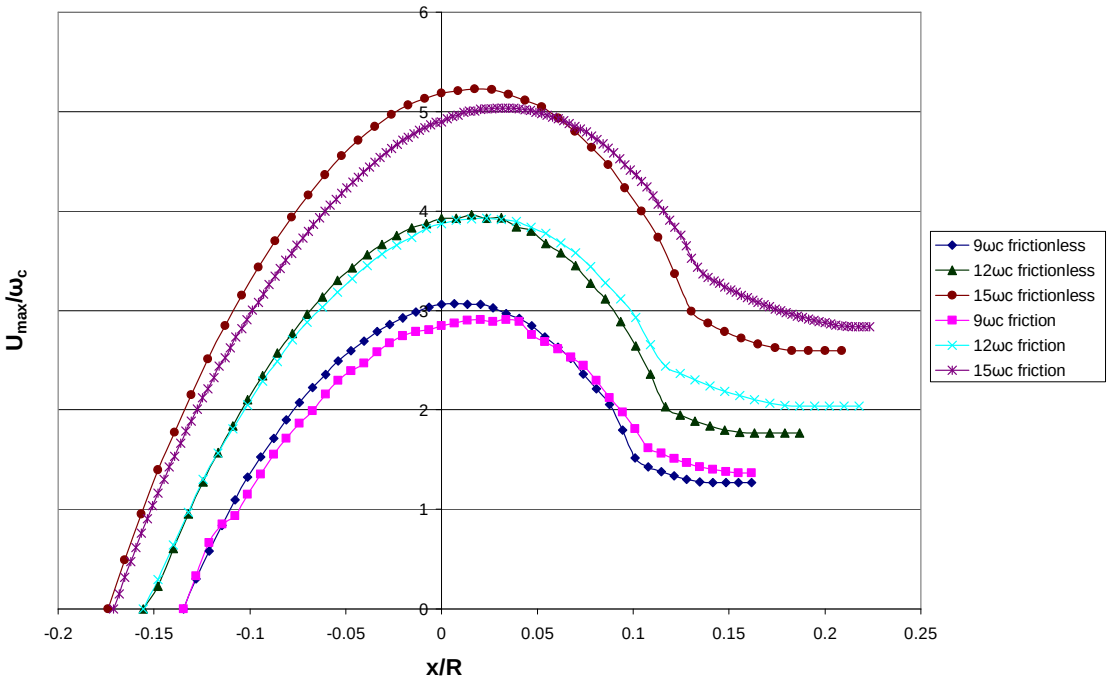

Figure 55: A comparison of the normalized maximum deformation in copper as sliding progresses for frictional and frictionless aluminum-on-copper contact.

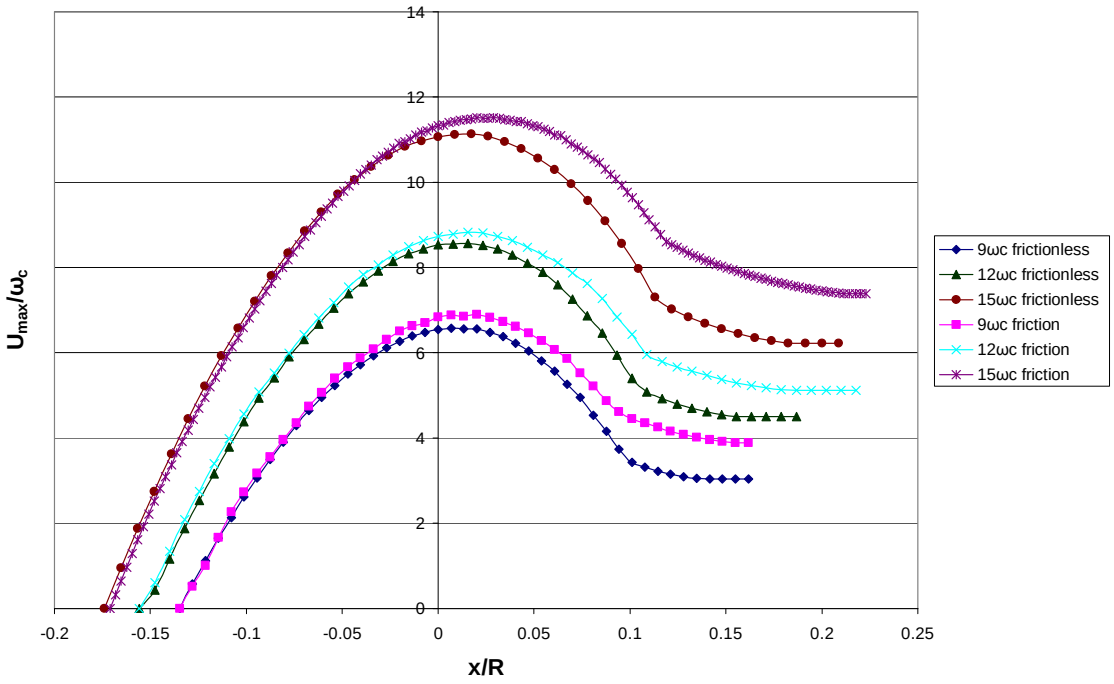

Figure 56: A comparison of the deformation in aluminum as sliding progresses for frictional and frictionless aluminum-on-copper contact.

Figures 57 and 58 present the residual deformations for steel-on-steel and aluminum-on-copper contact, respectively. As shown in the figures, there is more residual deformation in the frictional cases compared to the frictionless cases for all materials. The steel-on-steel case shows more divergence between frictional and frictionless sliding as the preset interference increases than either aluminum or copper in aluminum-on-copper contact, as shown by comparing Figures 57 and 58.

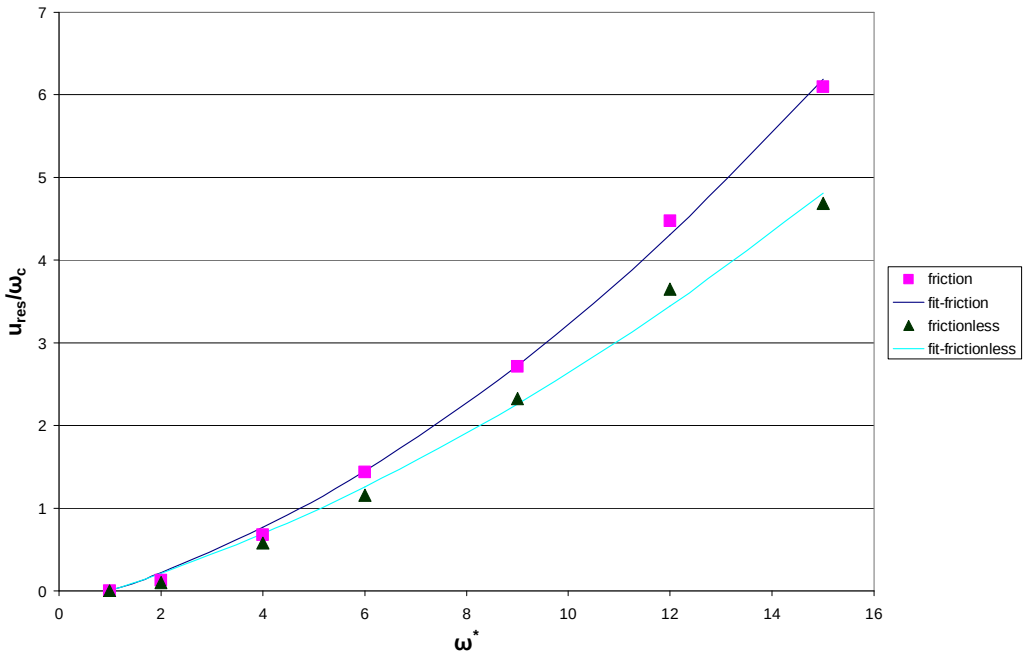

Figure 57: A comparison of the residual deformation for frictional and frictionless steel-on-steel contact.

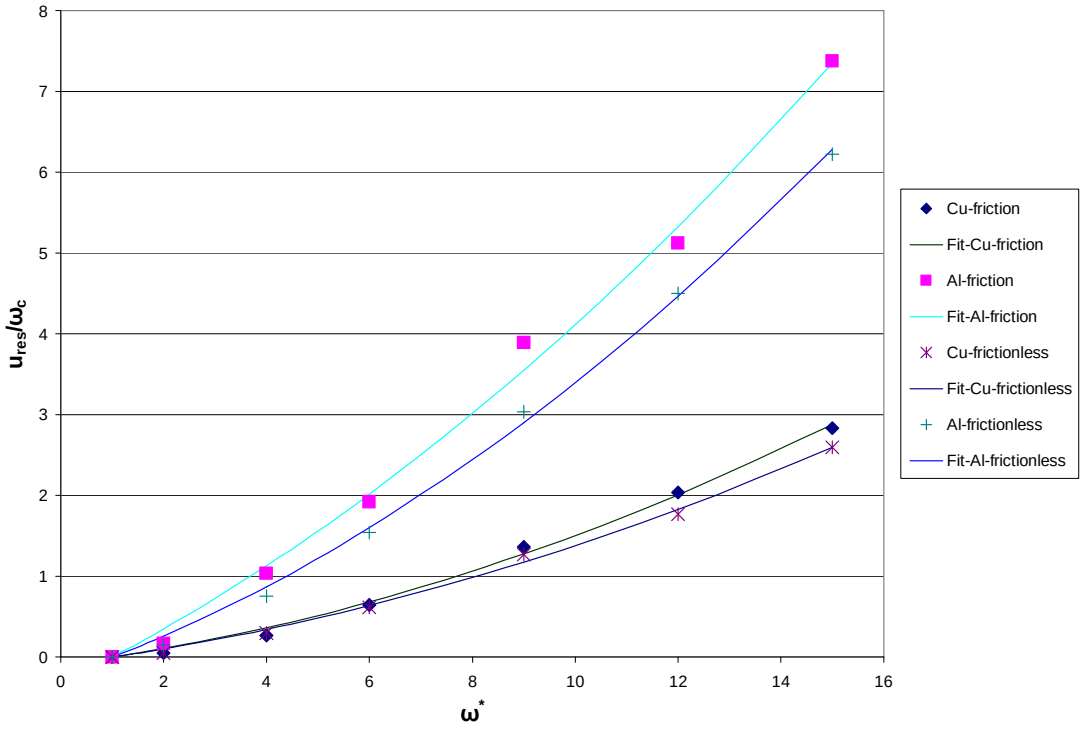

Figure 58: A comparison of the residual deformation for frictional and frictionless steel-on-steel contact.

5.7. Conclusions

Comparisons between frictional and frictionless sliding are drawn in this chapter. The von Mises stresses seen in frictional sliding are higher in magnitude and distributed in a larger volume than in the frictionless sliding cases. Also, the stress pattern in the frictional sliding cases is symmetric about a line angled in a direction that opposes sliding while in frictionless sliding, the stress pattern is symmetric about the vertical. All frictional sliding cases show that the residual stresses have reduced well below the yield strength while the frictionless steel-on-steel sliding $15\omega_c$ case shows residual stresses at the yield strength. Overall, the residual von Mises stresses are lower in the frictional sliding cases than in the frictionless sliding cases. Forces and contact areas are larger in magnitude for frictional sliding and the horizontal reaction force is completely negative in frictional sliding, while it becomes positive as the hemispheres separate in frictionless sliding. As friction is non-conservative, the energy loss in frictional sliding is much greater than in frictionless sliding. However, the effective coefficient of friction is similar in magnitude for both frictional and frictionless sliding for the cases studied. In steel-on-steel contact, both the residual and maximum deformations seen during sliding are larger for frictional sliding than frictionless sliding. Similarly, in aluminum-on-copper sliding the aluminum results in a larger maximum and residual deformation for frictional sliding compared to frictionless sliding. However, copper shows a smaller maximum deformation and a larger residual deformation for frictional sliding when compared to frictionless sliding.

CHAPTER VI: COMPARISON TO SEMI-ANALYTICAL RESULTS

Elastic-plastic sliding contact has no analytical solution. As such, one is reduced to numerical modeling to find a solution. This makes model validation difficult. There is however another numerical simulation to compare with the FEA see Boucly [22]. This numerical method is called a semi-analytical method (SAM). A brief description of the SAM is as follows. The contact pressure on the surface can be thought of as the summation of concentrated normal loads over the contact area. Each of these concentrated loads has a corresponding influence on the displacements throughout the body. This influence is quantified using influence coefficients, which are actually the discretized form of Green's functions. The SAM takes advantage of this by using the superposition principle to sum at each location in the region of interest the displacements due to the contact pressure. Once this information is gathered the stresses, strains, and deformations can be calculated based on the material properties from the compatibility and equilibrium relations. An iterative process is used to incorporate the residual deformations present from a previous load step. For more information on the specifics of the methodology used here see Boucly [22].

Figures 59 and 60 present a comparison of the normalized horizontal and vertical reaction forces for the different vertical interferences for steel-on-steel contact, respectively. The FEA and SAM results are nearly identical for the smaller interference cases. As shown in Figure 59, with increasing preset interference, the SAM results diverge from the FEA results once the hemispheres have passed the point of vertical alignment. As the hemispheres come out of contact, the SAM predicts a higher reaction

force indicating less energy loss due to plasticity. The vertical reaction force curves, as shown in Figure 60, are also nearly identical for all the interference cases presented.

One problem with the SAM as used here is that it is not capable of modeling two dissimilar materials as both being plastic. For identical materials this is not an issue (steel-on-steel for instance), but for the case of aluminum-on-copper sliding, a decision was made to model the copper hemisphere as elastic. The justification being that the residual deformations seen in the copper hemisphere are much lower than the residual deformations in the aluminum hemisphere. Figures 61 and 62 present the normalized horizontal and vertical reaction forces for aluminum-on-copper contact, respectively.

It can be seen that SAM results for both the horizontal and vertical reaction forces for the aluminum-on-copper cases, shown in Figures 61 and 62, deviate more from the FEA results than the steel-on-steel sliding cases, shown in Figures 59 and 60. The SAM produces normalized vertical reaction forces are higher than the FEA results in the aluminum-on-copper sliding. This is due to the condition that the copper hemisphere is modeled as completely elastic resulting in a higher overall load carrying capacity. This can also be seen in the normalized horizontal reaction force curves for aluminum-on-copper contact where the SAM yields forces larger in magnitude over more of the sliding distance for the loading phase than the FEA.

Overall, the SAM method shows promise to solve these types of problems. The greatest advantage of the SAM used here is the run time. The code takes hours to run as opposed to days for the FEA method used.

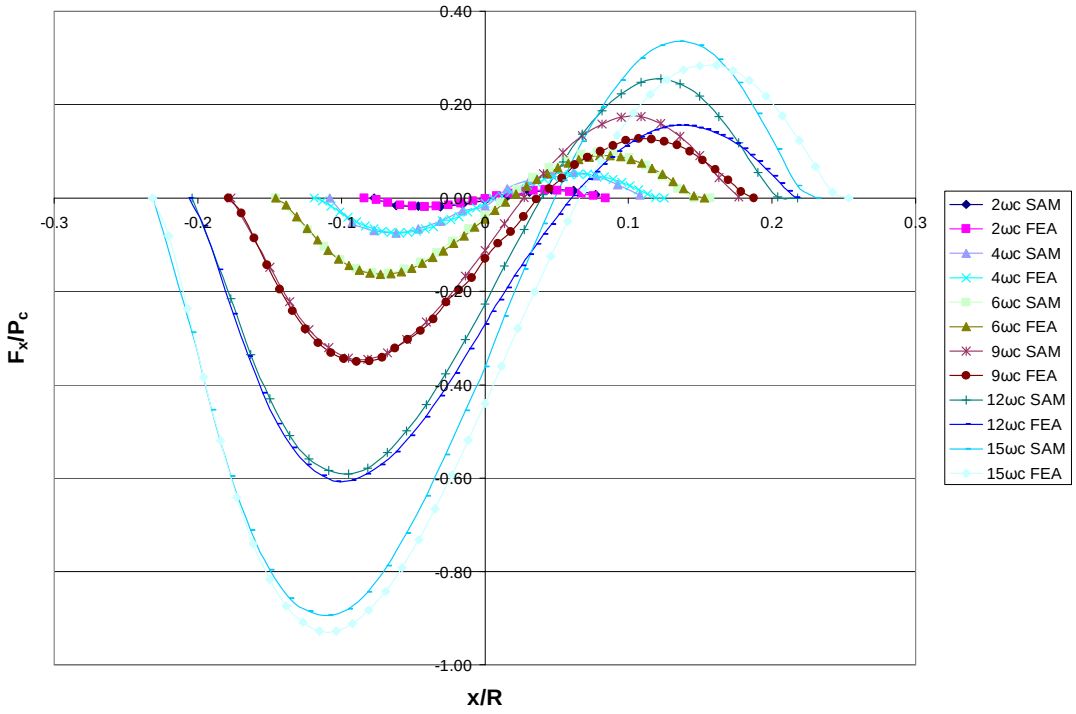

Figure 59: A comparison of the SAM and FEA results for the normalized horizontal reaction force for steel-on-steel contact.

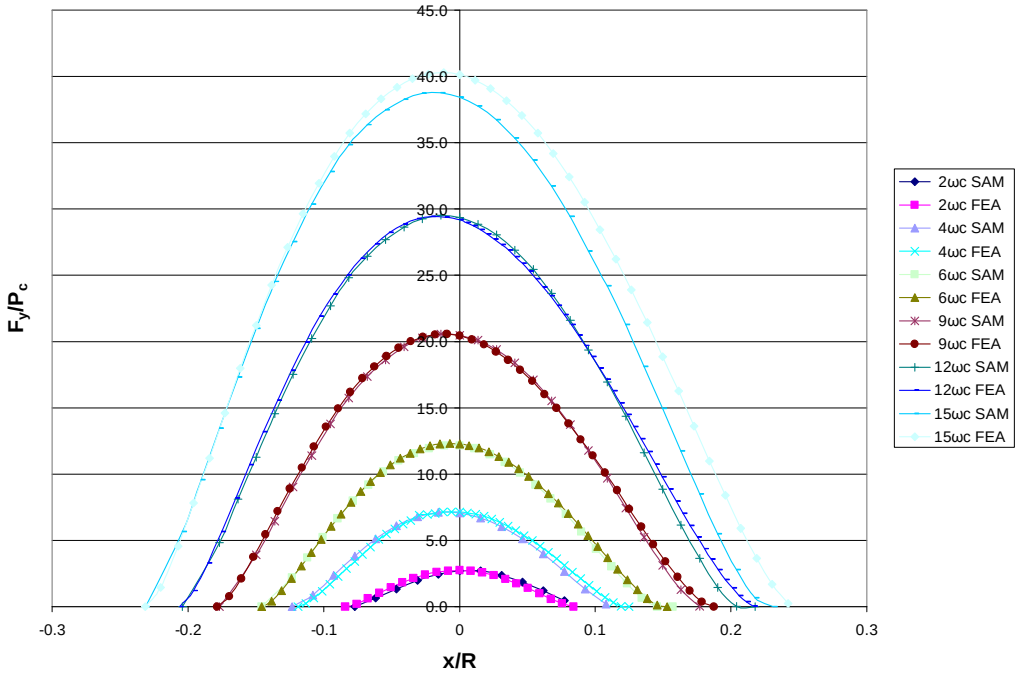

Figure 60: A comparison of the SAM and FEA results for the normalized vertical reaction force for steel-on-steel contact.

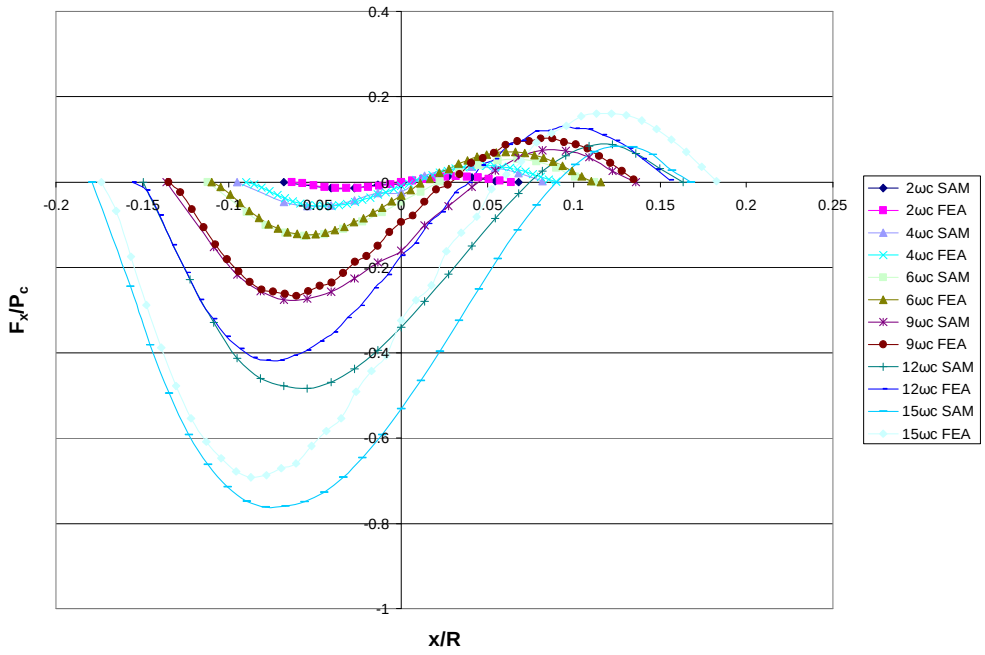

Figure 61: A comparison of the SAM and FEA results for the normalized horizontal reaction force for aluminum-on-copper contact.

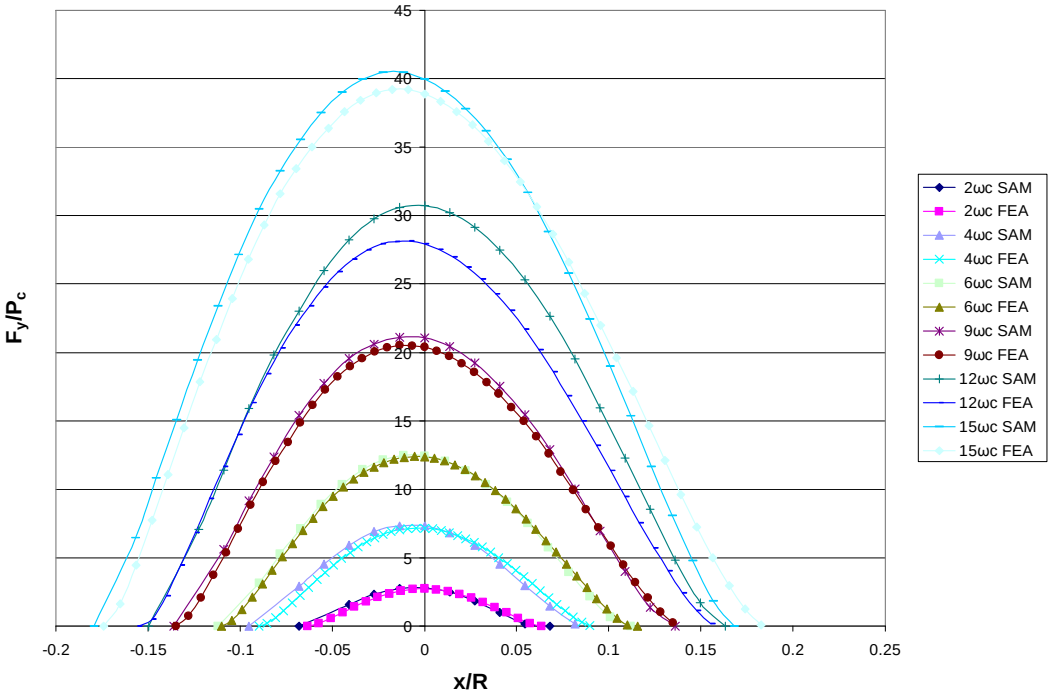

Figure 62: A comparison of the SAM and FEA results for the normalized vertical reaction force for aluminum-on-copper contact.

CHAPTER VII: COMPARISON OF HARDENING RESULTS

As previously stated, the material model contains a 2% strain hardening based on the Young's Modulus. This strain hardening is implemented in order to improve convergence time. This section presents different amounts of strain hardening for a high interference case of both frictional and frictionless sliding contact in order to draw conclusions about the effects of strain hardening on the parameters of interest.

Representative results for both material combinations studied in this analysis are presented. Frictional steel-on-steel contact with an interference of $12\omega_c$ is presented with a strain hardening values of both 2% and 0.5% of the Young's Modulus. Figure 63 presents the stress-strain curves for the steel material models to be discussed. Frictionless aluminum-on-copper contact with an interference of $15\omega_c$ is presented with a strain hardening values of 2% of both the Young's Modulus, E, and the yield strength, S_y. Figure 64 presents the stress-strain curves for the aluminum and copper material models to be discussed. Table 5 presents the cases presented here and the associated run time in hours. As shown in Table 5, increasing the strain hardening drastically decreases the run time (37% in frictional steel-on-steel contact with an interference of $12\omega_c$ and 66% in frictionless aluminum-on-copper contact with an interference of $15\omega_c$).

It would seem, based on the stress-strain curves presented, that the amount of strain hardening would have a dramatic effect on the results, but, with the interference cases studied here, the plastic strain does not get very high. For example, the frictional steel-on-steel contact with an interference of $15\omega_c$ and a strain hardening model of 2% of E yields a maximum strain of 0.092. With these small amounts of strain the results do not vary greatly.

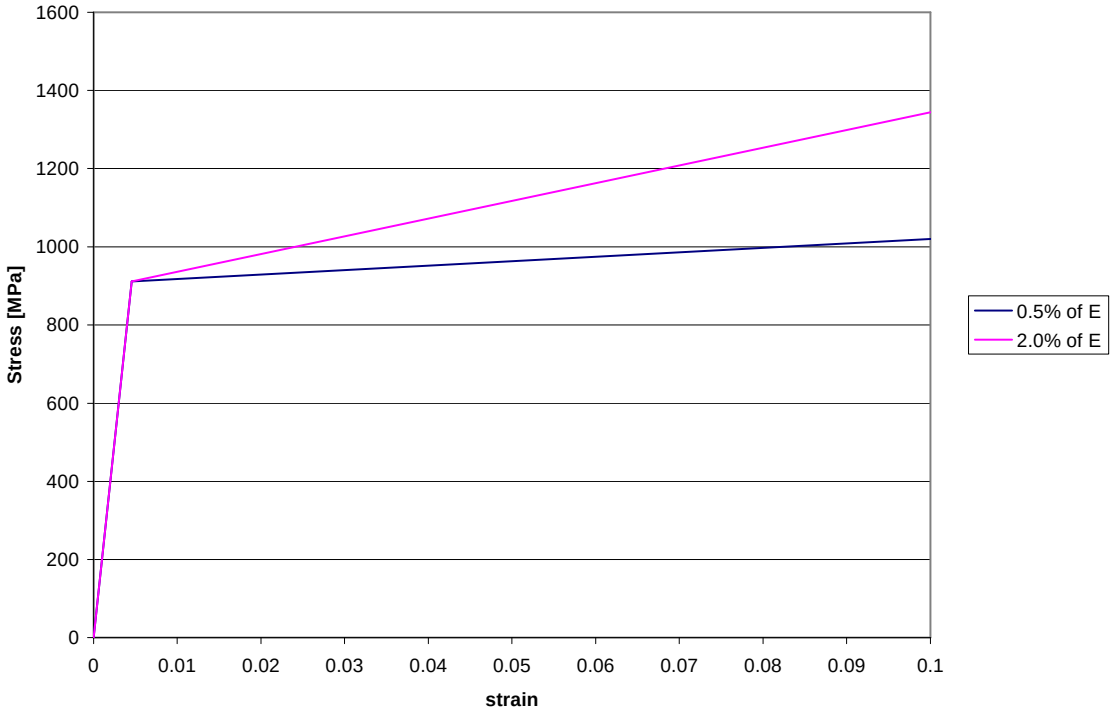

Figure 63: The stress-strain curve presenting the different hardening used for steel-on-steel contact.

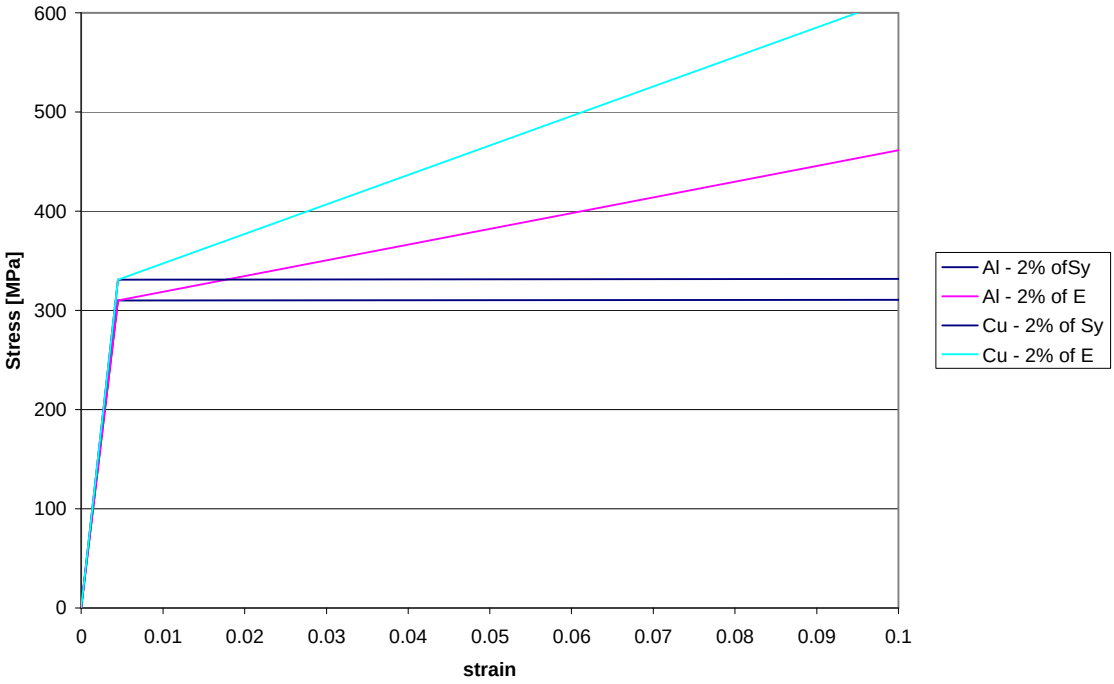

Figure 64: The stress-strain curve presenting the different strain hardening models used for aluminum-on-copper contact.

Table 5: The cases discussed in this chapter and the associated run time in hours.

	Stl-Stl	Al-Cu
2.0% of S_y	N/A	85 hrs.
0.5% of E	222.7 hrs.	N/A
2.0% of E	140.6 hrs.	29.8 hrs.

7.1. Stresses

The von Mises stress during sliding results increases as more strain hardening is implemented. Figure 65 presents the von Mises plots for steel-on-steel contact at the point of vertical alignment for strain hardening of both 0.5% and 2.0% of the Young's Modulus. Figure 66 presents the von Mises plots for aluminum-on-copper contact at the point of vertical alignment for strain hardening values of 2% of both the yield strength and the Young's Modulus. Table 6 presents the maximum values of the von Mises stress for each material and strain hardening value studied. As shown in Table 6, the aluminum and copper show nearly a perfectly plastic behavior for a strain hardening rate of 2% of S_y and higher stress values for a strain hardening value of 2% of E. Similar results are seen in steel-on-steel contact.

Table 6: Maximum von Mises stress for each material and strain hardening combination studied.

		Strain Hardening		
		2% of S_y	0.5% of E	2% of E
Material	Steel	N/A	1.03 GPa	1.21 GPa
	Aluminum	310 MPa	N/A	348 MPa
	Copper	331 MPa	N/A	379 MPa

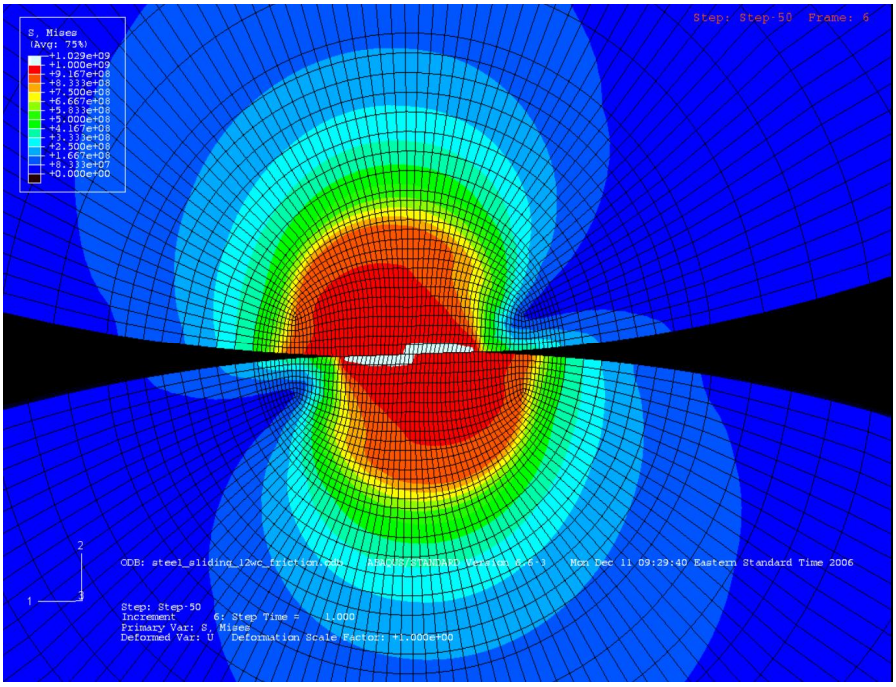

(a)

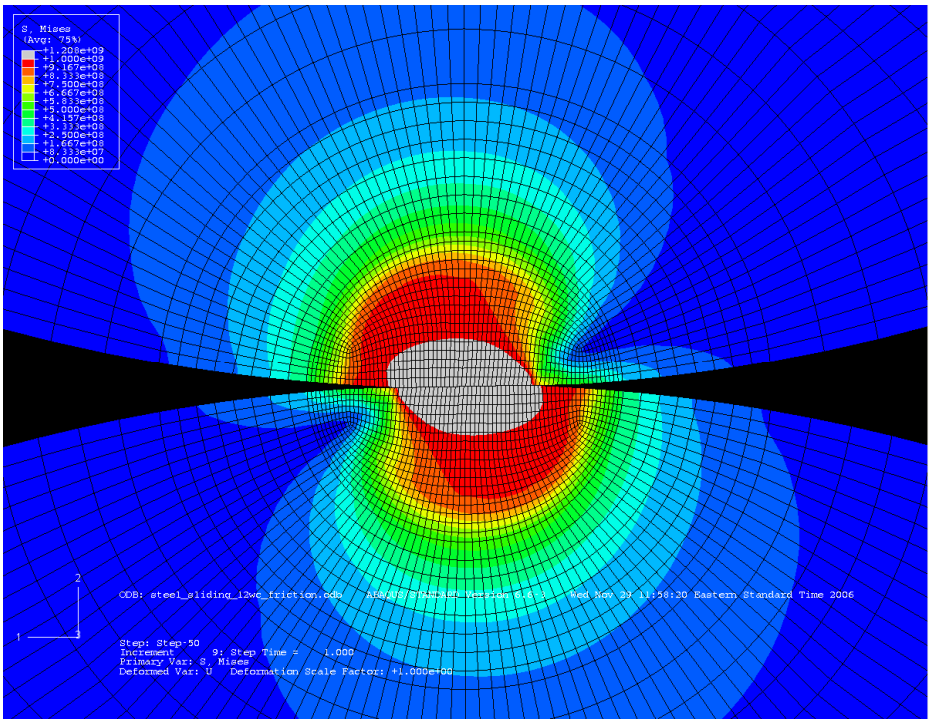

(b)

Figure 65: Frictional steel-on-steel contact with an interference of $12\omega_c$ for a strain hardening of (a) 0.5% and (b) 2.0% of *E*.

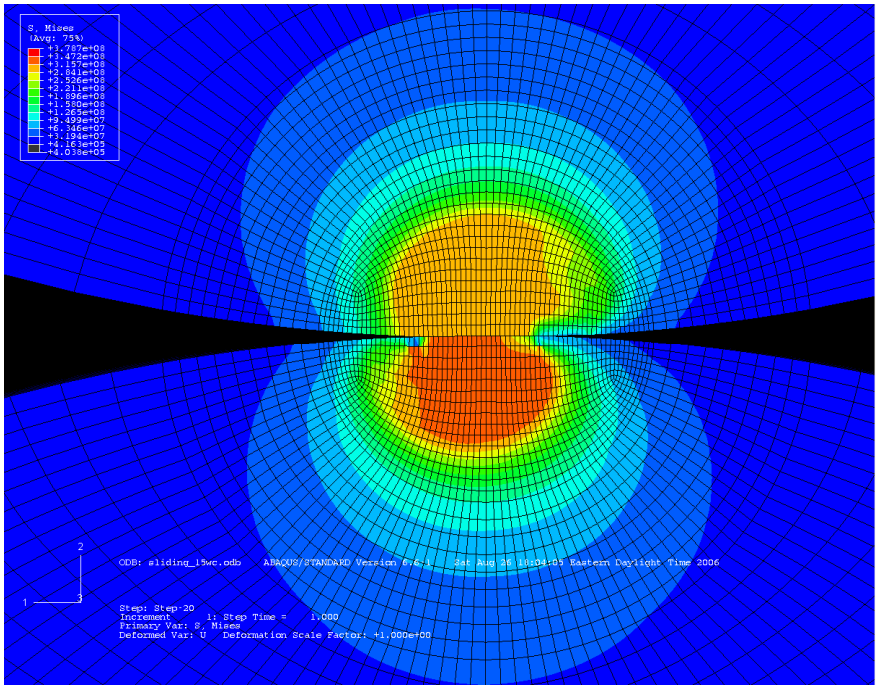

(a)

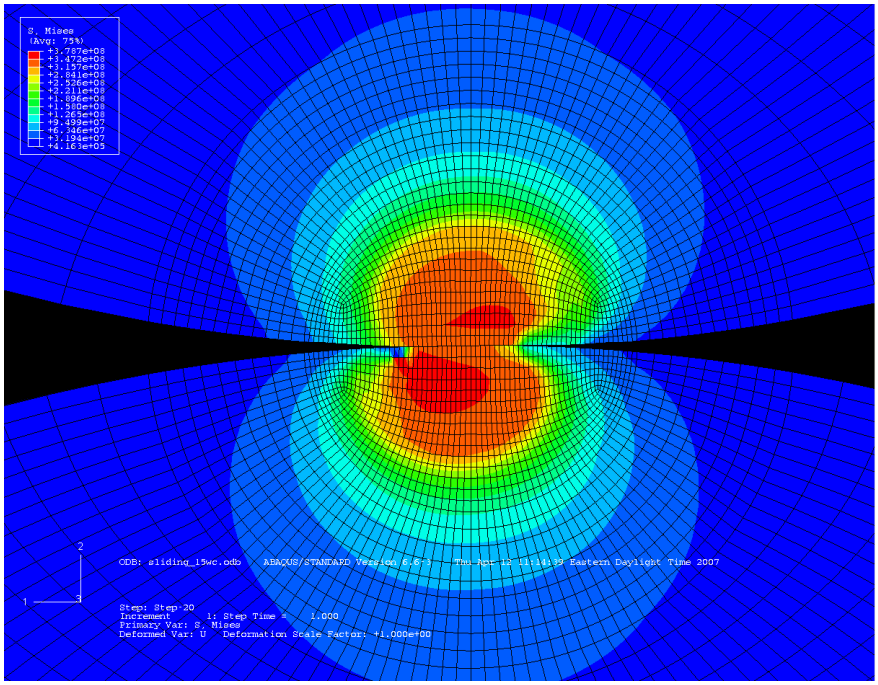

(b)

Figure 66: Frictionless aluminum-on-copper contact with an interference of $15\omega_c$ for a strain hardening of (a) 2% of S_y and (b) 2% of E.

7.2. Reaction Forces

To further characterize the importance of the strain hardening implemented in elastic-plastic sliding contact, the reaction forces are presented. Tables 7 and 8 present the percent difference of the maximum vertical and horizontal reaction forces for frictional steel-on-steel sliding contact with and interference of $12\omega_c$ and frictionless aluminum-on-copper sliding contact with an interference of $15\omega_c$, respectively.

Figures 67 and 68 show the normalized vertical and horizontal reaction forces for steel-on-steel contact for both strain hardening models used, respectively. As shown in the figures, the reaction forces are initially the same but, as more plastic deformation takes place, the two curves diverge. The lower strain hardening material model results in lower reaction forces once plasticity becomes significant. With increasing strain hardening, the plastically deformed material will have a higher load carrying capacity and will therefore have larger reaction forces for the same preset interference. As shown in the tables, the vertical reaction force varies more than the horizontal yet neither varies greatly with a maximum percent difference of 10%.

Figures 69 and 70 present the normalized vertical and horizontal reaction forces for aluminum-on-copper for both strain hardening models implemented, respectively. Similar results can be seen for aluminum-on-copper as is shown in steel-on-steel contact. Once again, the lower strain hardening material model results in lower reaction forces. Similar results as to steel-on-steel can be seen, especially in the vertical reaction forces. However, as this is a frictionless sliding process (the steel-on-steel results presented are frictional), the horizontal reaction force is quite different. As shown in Figure 70, the largest difference occurs as the hemispheres are coming out of contact. In fact, the

largest percent difference is 24.5% (see Table 8) occurring at the maximum positive horizontal reaction force. This occurs as the hemispheres are disengaging and the effects of plasticity have already taken place.

Table 7: Percent difference of the maximum normalized reaction forces for frictional steel-on-steel sliding contact at an interference of $12\omega_c$.

	% Diff
F_x	0.65%
F_y	10.03%

Table 8: Percent difference of the maximum normalized reaction forces for frictionless aluminum-on-copper sliding contact at an interference of $15\omega_c$.

	% Diff
F_x (Neg)	1.01%
F_x (Pos)	24.52%
F_y	2.58%

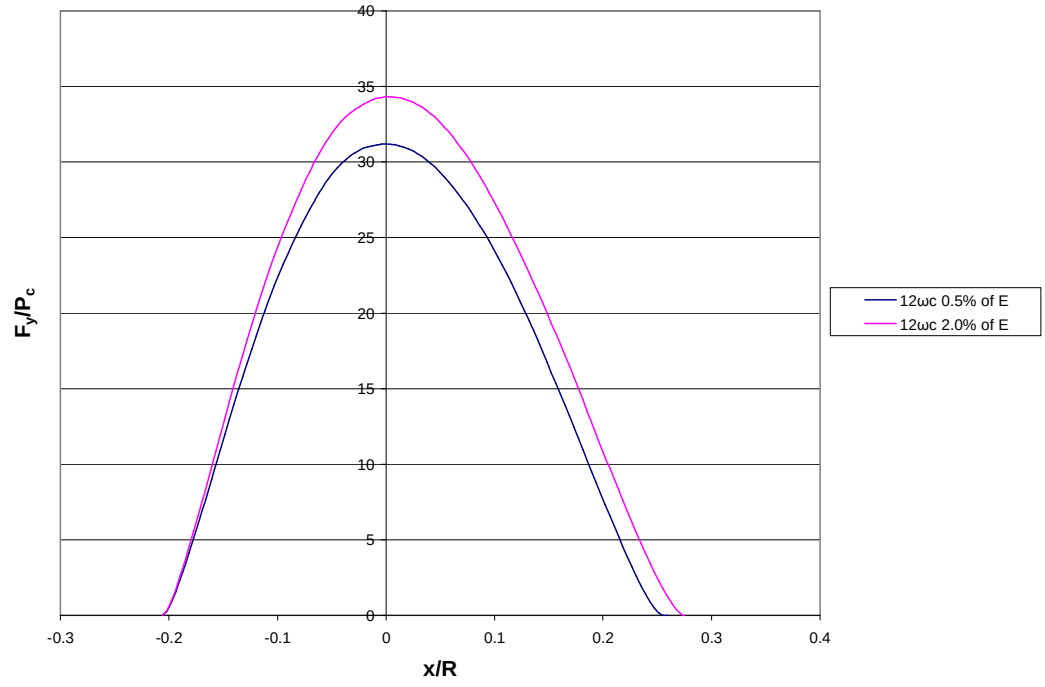

Figure 67: The normalized vertical reaction force for steel-on-steel contact for both strain hardening models studied.

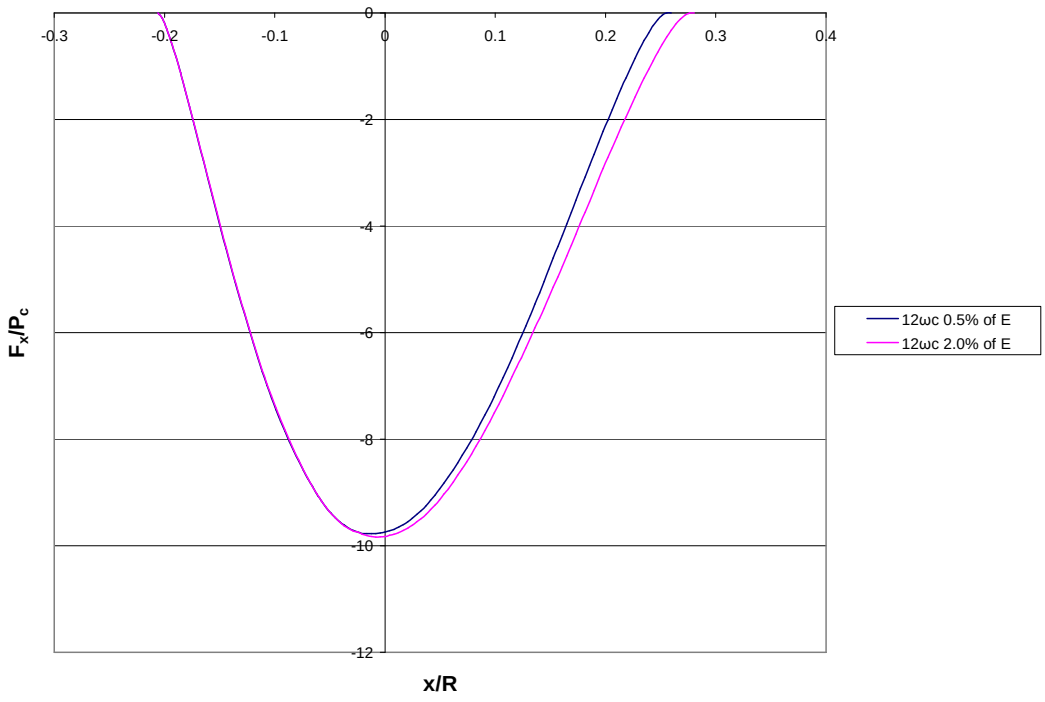

Figure 68**:** The normalized horizontal reaction force for steel-on-steel contact for both strain hardening models studied.

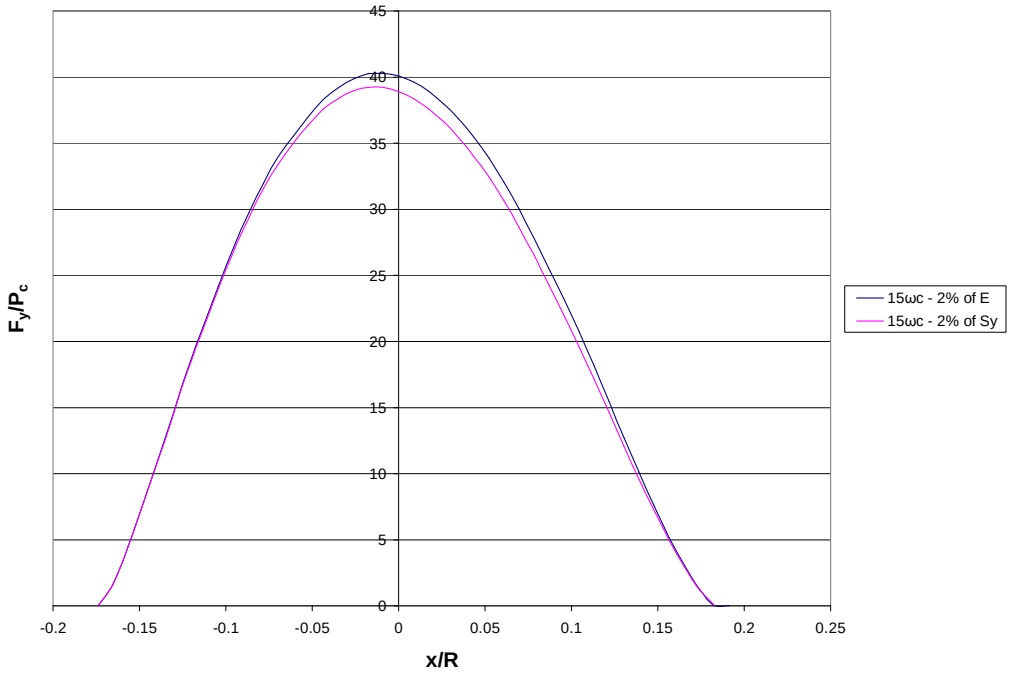

Figure 69: The normalized vertical reaction force for aluminum-on-copper contact for both strain hardening models studied.

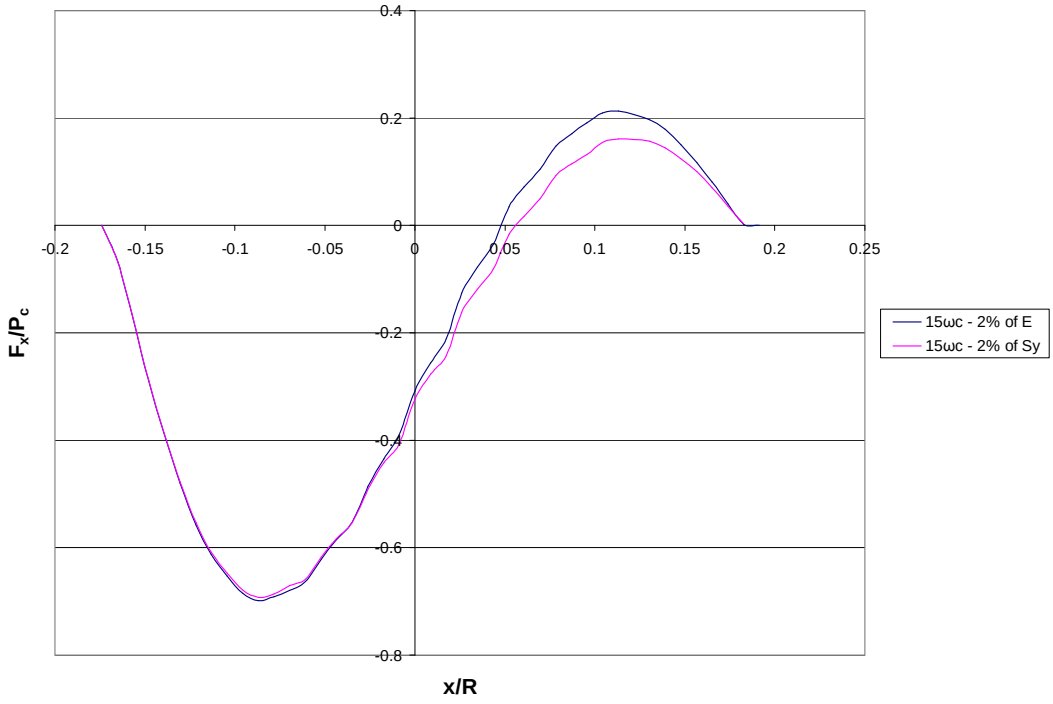

Figure 70: The normalized horizontal reaction force for aluminum-on-copper contact for both strain hardening models studied.

7.3. Energy Loss

The net energy loss, as described by Eq. (9), can also be used to compare the influence of the effects strain hardening in elastic-plastic sliding. Table 9 presents a comparison of the normalized net energy loss for the different strain hardening values. Less strain hardening results in more energy loss due to plastic deformation for frictionless sliding contact (see the Al-Cu values in Table 8). This is because as the hemispheres are separating there is less rebound force in the plastically deformed material for the smaller strain hardening values (see Figure 70). However, for frictional sliding (see the steel-on-steel contact values in Table 7) the opposite is true. This is because the increase in the rebound force with a higher strain hardening (reducing the energy loss) is masked by a much larger increase in energy loss due the increased opposition to sliding from friction. The increased opposition to sliding, or shear traction due to friction, results from its dependence on the vertical reaction force (see Eq. (11) and Figure 63), which increases with increasing strain hardening.

Table 9: A comparison of strain hardenings effect on the normalized net energy loss for frictional steel-on-steel contact at an interference of $12\omega_c$ and frictionless aluminum-on-copper contact at an interference of $15\omega_c$.

	Stl-Stl	Al-Cu
2.0% of S_y	N/A	811
0.5% of E	7920	N/A
2.0% of E	15200	743

7.4. Deformations

The degree of strain hardening effects the deformation during sliding. As more strain hardening is effectively a stiffer material once deformed plastically, there is less deformation for a given interference as well as less residual deformation. Table 10 presents the percent difference in the maximum and residual deformations for steel in frictional steel-on-steel contact at an interference of $12\omega_c$ and aluminum and copper in frictionless aluminum-on-copper contact at an interference of $15\omega_c$.

Figure 71 presents the normalized deformation for frictional steel-steel contact with a preset interference of $12\omega_c$ for strain hardening values of both 2% and 0.5% of the Young's Modulus. As shown in the figure, the lower strain hardening value displays more deformation once plasticity becomes significant. In fact, the percent difference in the maximum deformation is 3.47% and the difference in the residual deformation is 9.58% for the different strain hardening values.

Table 10: Percent difference in the maximum and residual deformation for different strain hardening values.

	% Diff (Max)	% Diff (Res)
Steel	3.47%	9.58%
Aluminum	2.97%	7.38%
Copper	1.59%	0.78%

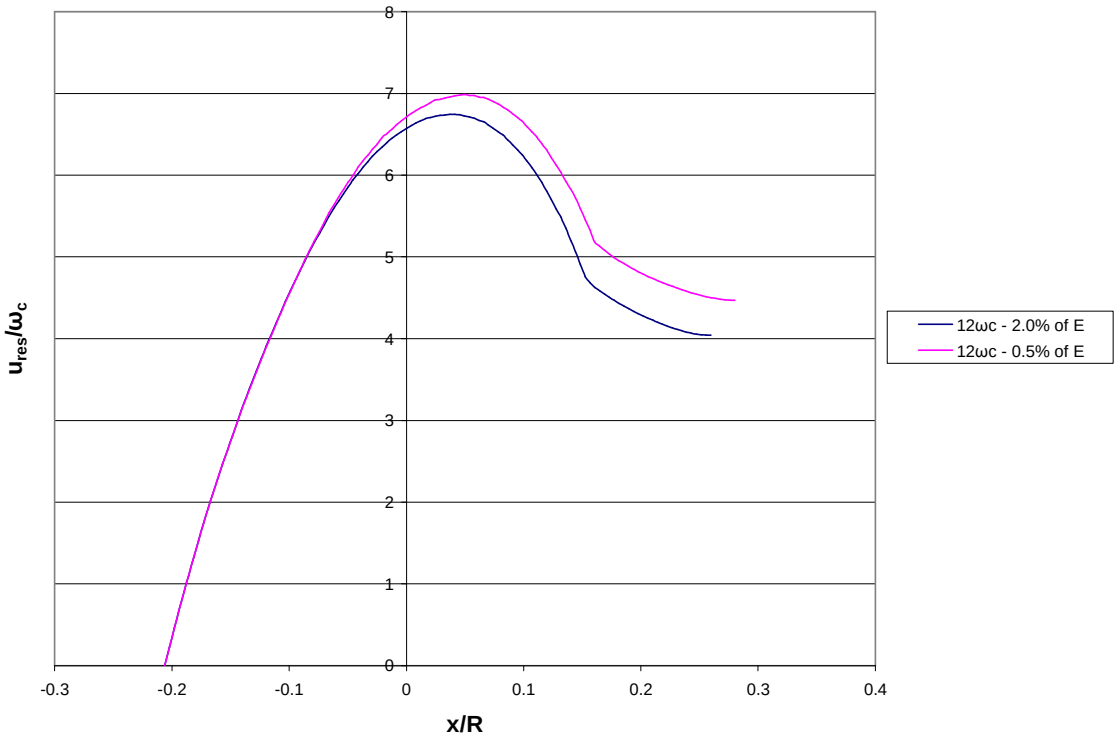

Figure 71: Deformations for frictional steel-on-steel contact with a preset interference of $12\omega_c$ for strain hardening of both 2% and 0.5% of E.

Figure 72 presents the normalized deformation for frictionless aluminum-on-copper contact at an interference of $15\omega_c$ for 2% of both the Young's Modulus and the yield strength. Aluminum shows the same trend as steel in the steel-on-steel sliding contact situation, with a 2.97% difference in the maximum deformation and a 7.38% difference in the residual deformation. However, copper shows the opposite during sliding. The larger strain hardening model produces slightly more deformation in copper but slightly less residual deformation. Copper shows the smallest difference in deformation with different strain hardening values with a 1.59% difference in maximum deformation and 0.78% difference in residual deformation.

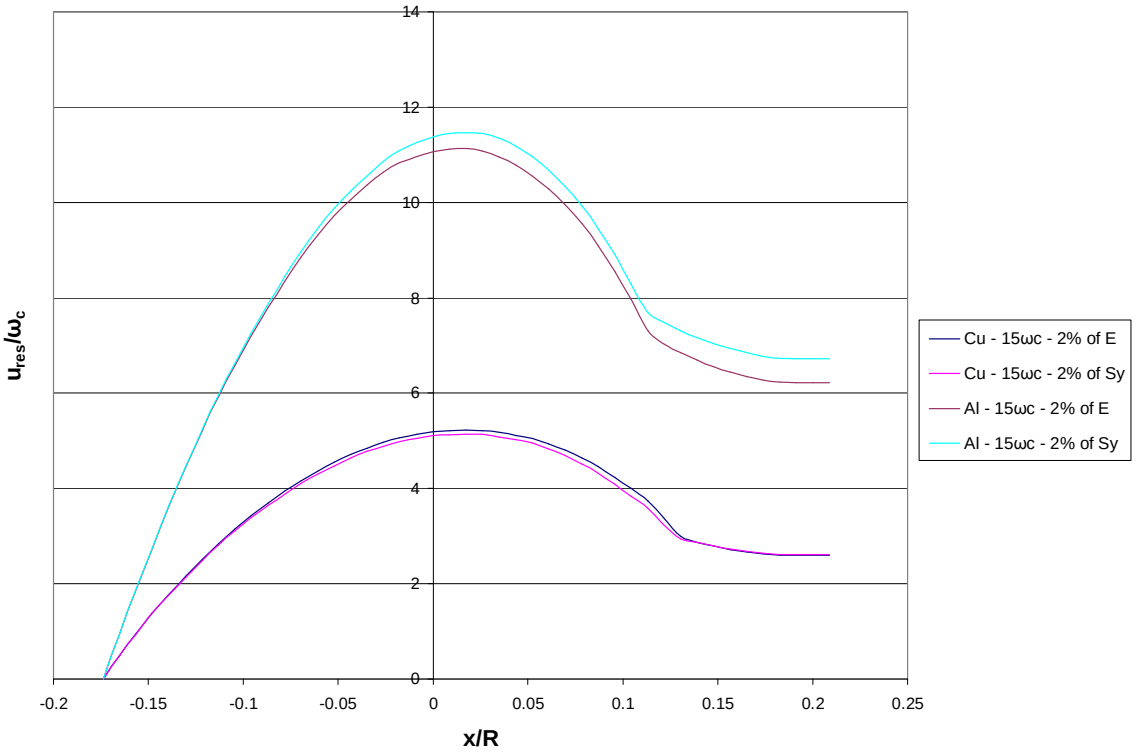

Figure 72: Deformations in frictionless aluminum-on-copper contact with a preset interference of $15\omega_c$ for strain hardening of 2% of both E and S_y.

7.5. Conclusions

Comparisons between different amounts of strain hardening are drawn in this chapter for a frictional steel-on-steel contact situation with an interference of $12\omega_c$ and a frictionless aluminum-on-copper contact situation with an interference of $15\omega_c$. The magnitudes of the von Mises stress increase with increasing strain hardening. Forces are larger with more strain hardening. The net energy loss is lower with more strain hardening for frictionless sliding because the plastically deformed material will impose more of a rebound (positive) force as the hemispheres are separating. However, in

frictional sliding this effect is masked by the increase in shear traction opposing sliding resulting from the imposed coefficient of friction. In steel-on-steel contact both the residual and maximum deformations seen during sliding decrease with increasing strain hardening. Similarly, in aluminum-on-copper sliding the aluminum material has smaller maximum and residual deformations for larger values of strain hardening. On the other hand, copper shows slightly more deformation throughout sliding with increasing strain hardening but slightly less residual deformation. In terms of percent difference of maximum values, it can be seen that strain hardening has some effect on the results, but by and large the values and general behavior are similar.

CHAPTER VIII: COMPARISON OF HEMISPHERICAL AND CYLINDRICAL RESULTS

As this analysis is very similar to the method followed by Vijaywargiya and Green [26] for cylindrical sliding contact a comparison of results may be of interest. It should be noted, however, that the previous work concentrated on modeling of cylinders in sliding contact. A plane strain assumption is assumed in [26], whereas, this work considers a full 3D model of sliding hemispheres. In fact, the parameters of interest are normalized by completely different critical values, both in magnitude and definition, for cylindrical and hemispherical sliding. As such, only a qualitative comparison of the trends is presented. All results in this chapter are for frictionless steel-on-steel sliding contact with identical material properties for both the cylinders and hemispheres.

8.1. Reaction Forces

Some similarities can be seen in the normalized horizontal reaction force curves as shown in Figure 73 (a) and (b) for cylindrical and hemispherical sliding, respectively. In both cylindrical and hemispherical sliding contact the horizontal reaction force is not zero when the bodies are vertically aligned. Also, as the vertical interference increases the force curves become less anti-symmetric in both cases, indicating more plasticity is taking place. However, as shown in 73(a), the maximum positive force value tends to reach a stable maximum in cylindrical sliding but this is not seen in hemispherical sliding contact (Figure 73(b)). It can be seen that there is more prolonged opposition to sliding in the cylindrical sliding cases. This is due to the fact that it is a 2D plane strain analysis and, as such, all the deformation must be absorbed in a single plane. Whereas in 3D hemispherical sliding there is material outside of a single plane to absorb deformation.

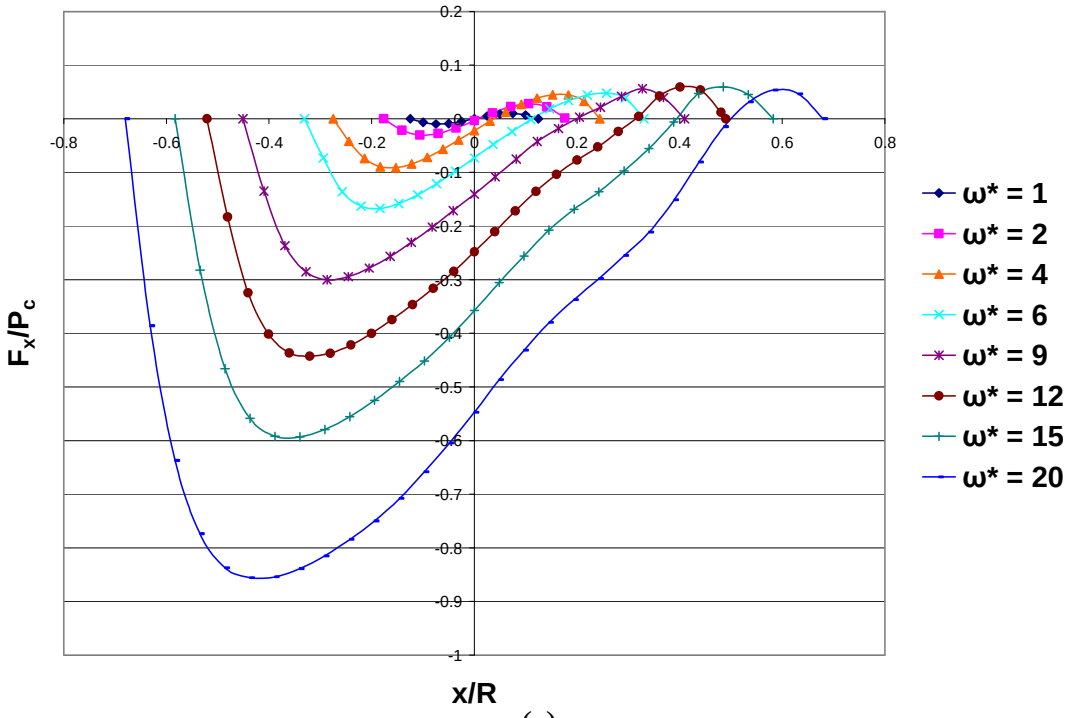

(a)

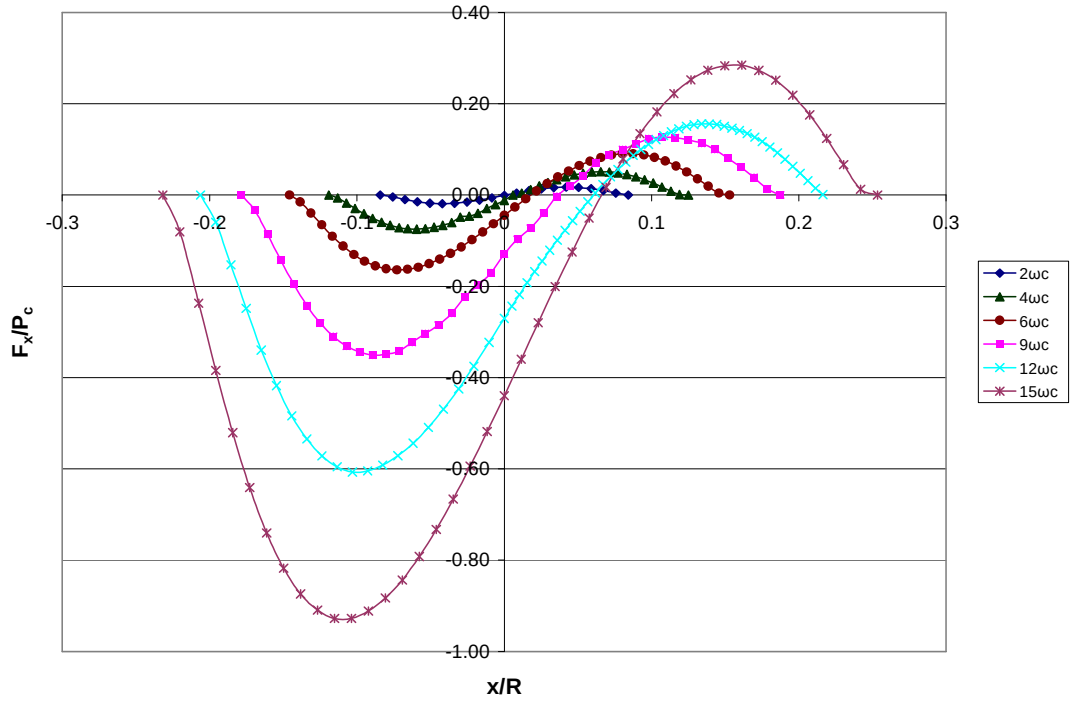

(b)

Figure 73: Normalized horizontal reaction force versus sliding distance for (a) cylindrical and (b) hemispherical sliding contact.

The normalized vertical reaction forces as sliding progresses for cylinders and hemispheres are presented in Figure 74(a) and 74(b), respectively. As shown in the figure, the hemispherical sliding contact situation yields much larger normalized vertical reaction forces. The maximum normalized vertical reaction force occurs progressively earlier in the progression of sliding in both cylindrical and hemispherical sliding contact. However, the hemispherical sliding results are much more symmetric about the axis of vertical alignment, whereas the cylindrical results tend to flatten out near the maximum, which occurs earlier in the progression of sliding.

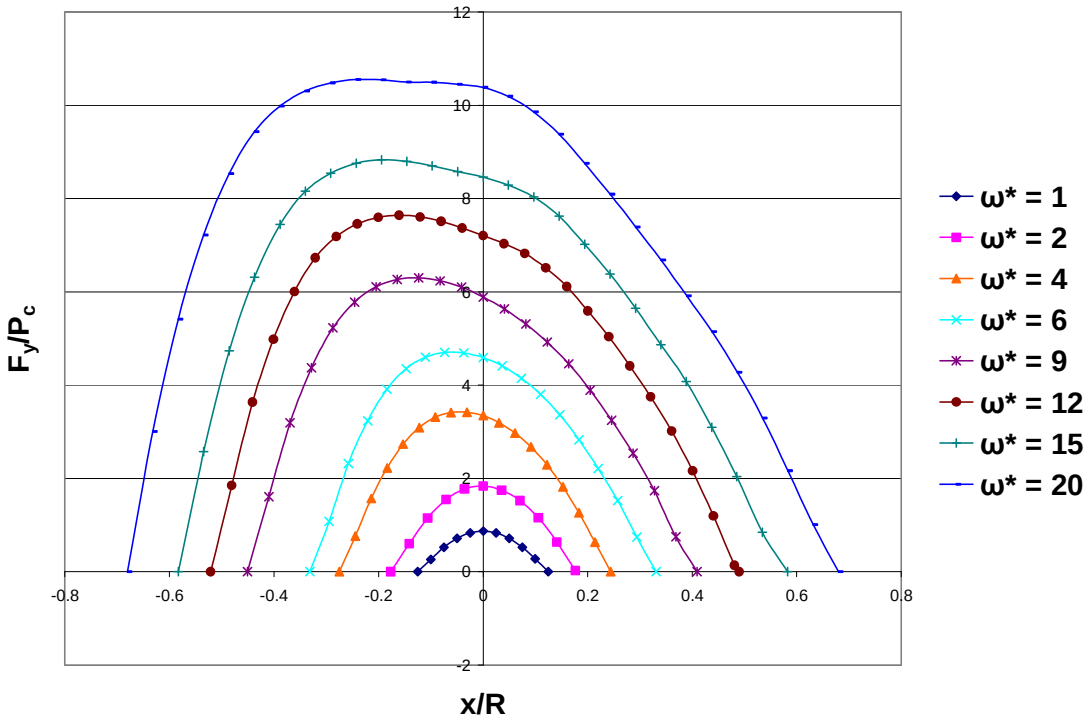

(a)

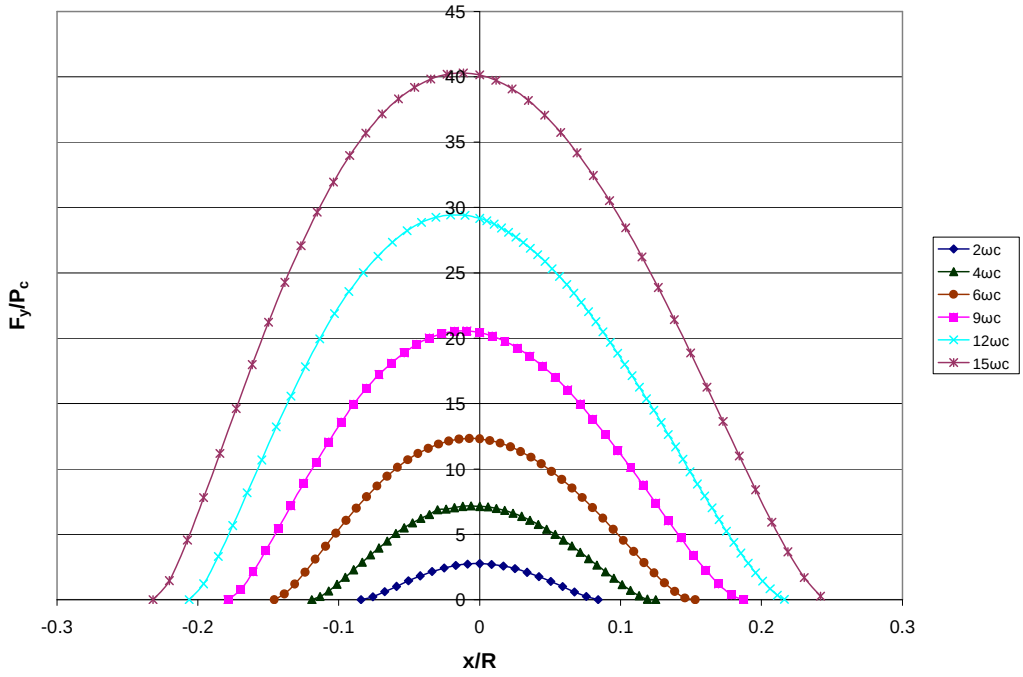

(b)

Figure 74: Normalized vertical reaction force versus sliding distance for (a) cylindrical and (b) hemispherical sliding contact.

8.2. Contact Dimensions

Figure 75 presents the contact pressure in frictionless steel-on-steel contact with an interference of $15\omega_c$ at the point of vertical alignment. This figure shows a top-view of one of the hemispheres at the contact interface. The actual contact area can be defined as any region with a non-zero contact pressure. As the dark blue region has a contact pressure value of zero, all other colored regions display some non-zero value of contact pressure and are in contact. As shown in the figure, hemispherical sliding contact has an irregularly shaped contact zone (i.e., not circular nor elliptical) and, as such a, contact half-width cannot be defined. Therefore, the two values, though both non-dimensional, are not equivalent.

Figure 76(a) presents the normalized contact half-width for cylindrical sliding contact and Figure 76(b) presents the normalized contact area for hemispherical sliding contact. Some similarities can be noted in the two contact situations, however. Firstly, it can be seen that the maximum value occurs before the axis of vertical alignment for both cases. The values then tend to dip and flatten out near the axis of vertical alignment for both cases. Also of note is that the general shape is similar indicating that the deformation has a similar effect on the contact area in both cylindrical and hemispherical sliding contact.

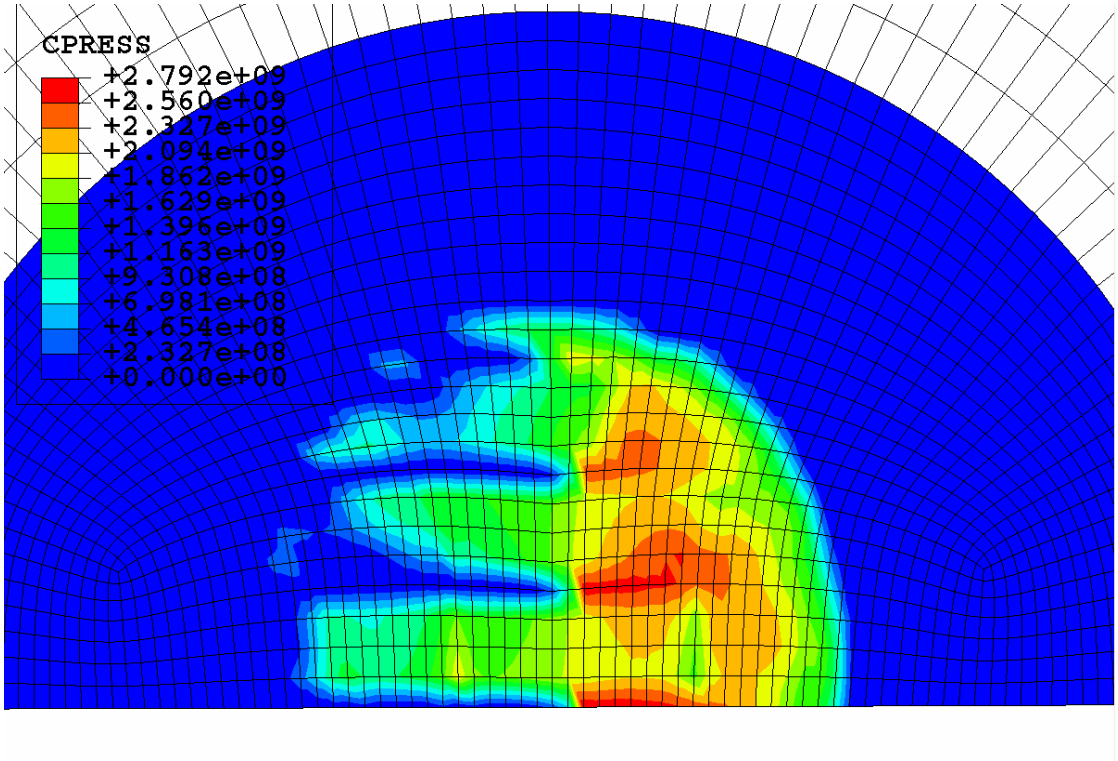

Figure 75: Contact pressure in frictionless steel-on-steel contact with an interference of $15\omega_c$ at the point of vertical alignment.

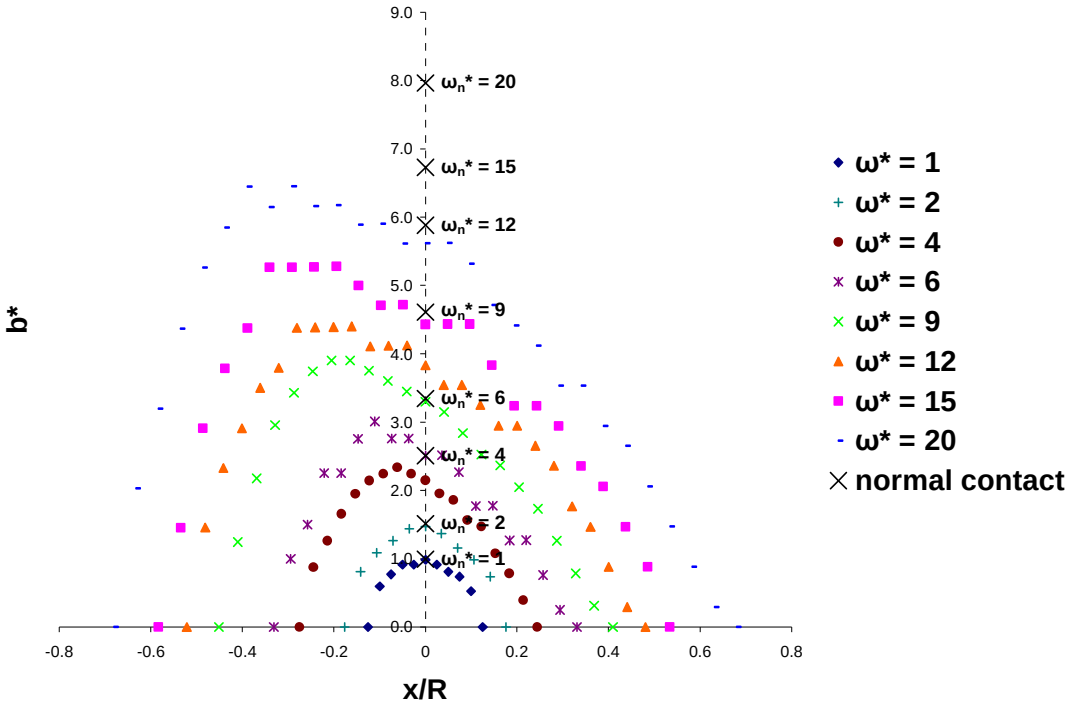

(a)

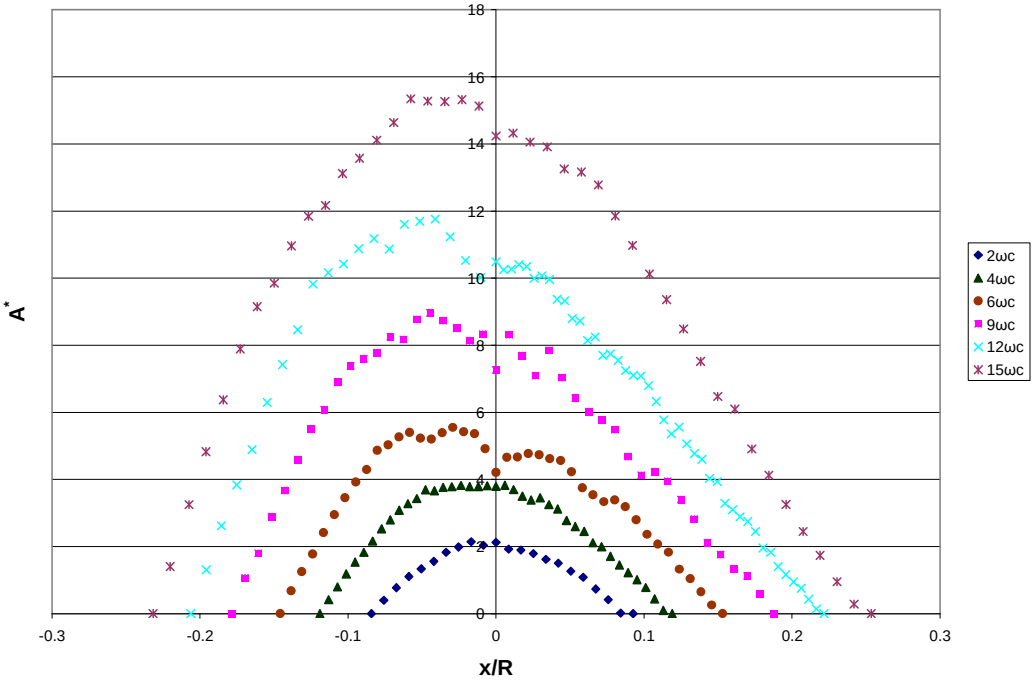

(b)

Figure 76: (a) Normalized contact half-width for cylindrical sliding (b) Normalized contact area for hemispherical sliding.

8.3. Deformations

The maximum deformations as sliding progresses for both cylindrical and hemispherical sliding contact are presented in Figure 77(a) and 77(b), respectively. As shown in the figure, both cylindrical and hemispherical sliding cases show a similar trend. As the preset vertical interference increases, the maximum value occurs later in the progression of sliding. The magnitude of the maximum normalized deformations is similar for both hemispherical and cylindrical sliding contact as well with the cylindrical sliding cases being slightly greater than the hemispherical on a case-by-case basis.

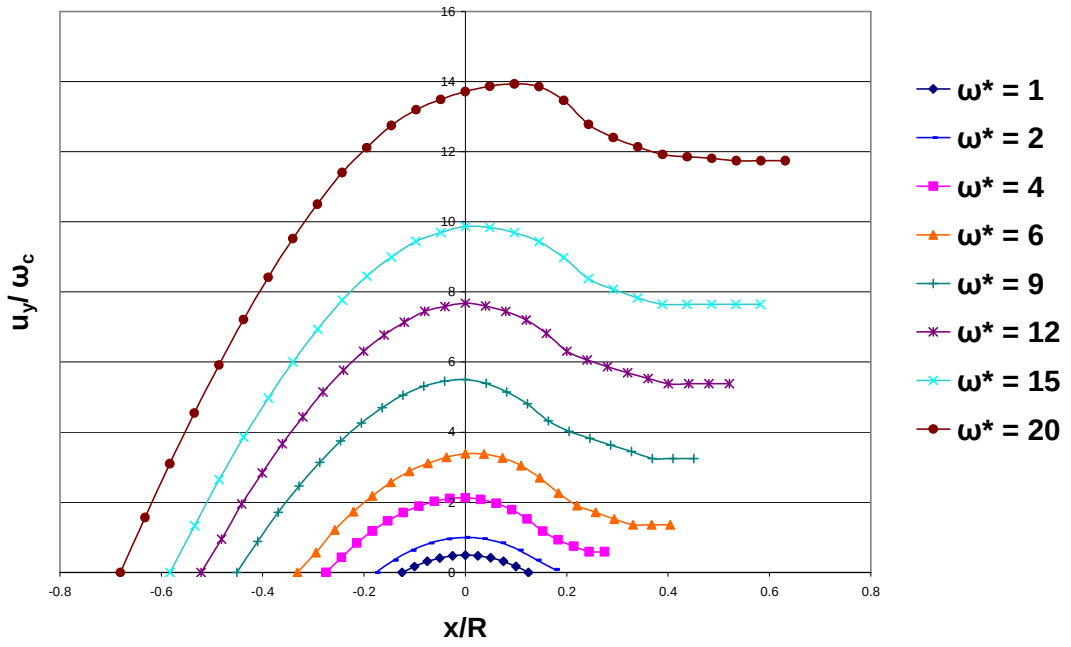

(a)

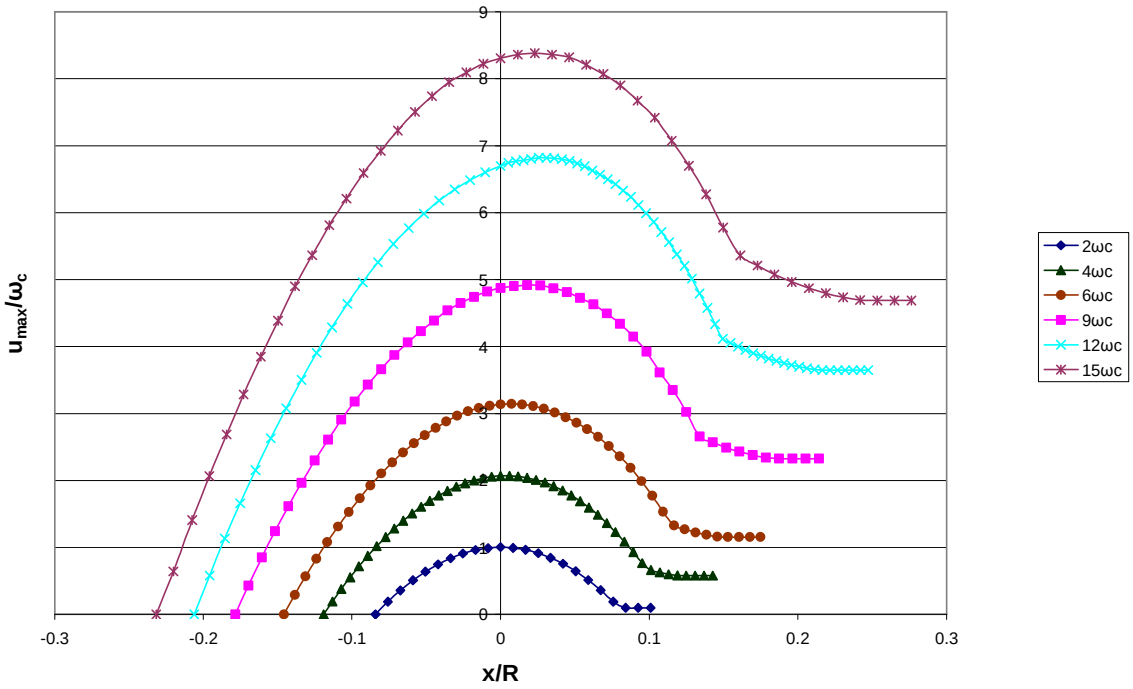

(b)

Figure 77: Normalized deformations as sliding progresses for (a) cylindrical and (b) hemispherical sliding contact.

8.3. Conclusions

Some of the results in this analysis are compared to cylindrical elastic-plastic sliding results by Vijaywargiya and Green [26]. Though qualitative comparisons of the trends are given, the results can not be quantitatively compared. Cylindrical sliding contact, as modeled in [26] is a 2D plane strain analysis, where the present work is a full 3D analysis. These are two distinct loading phenomena. However, some similarities are shown here.

The reaction forces, contact dimensions, and maximum deformations as sliding progresses for both cylindrical and hemispherical sliding contact have been compared. The general shapes of the reaction force curves are similar for both cases, but the magnitudes are quite different. The same can be said about the contact dimensions as sliding progresses. The maximum deformations seem to display the most similarity in trend, but, even here, the shape of the curves and magnitudes are different.

CHAPTER IX: THE EFFECTIVENESS OF THE NORMALIZATION SCHEME

It has been shown that the normalization scheme, as introduced in Chapter 2 and defined by [24], is effective when comparing steel-on-steel and aluminum-on-copper contact. This section expands on this finding and compares the normalized reaction forces for other metal-on-metal sliding contact situations. In this section the SAM is used to model copper-on-copper, aluminum-on-aluminum, and three different steel material models for steel-on-steel sliding contact. The FEA as presented earlier is used for the aluminum-on-copper sliding contact in order to make an equitable comparison as the SAM cannot model both materials being elasto-plastic in dissimilar-material sliding contact. Table 11 presents the material properties and critical values used here.

In this analysis, a parametric study on the effects of varying the yield strength, S_y, is carried out. Since steel has a fairly constant Young's Modulus and a variable yield strength, it was chosen for the parametric study. It is found that if the ratio of CS_y to E' is the same then the normalized force curves are identical for identical-material contact (i.e., steel-on-steel or aluminum-on-aluminum). In fact, for the lower interference cases, it is found that the aluminum-on-copper and steel-on-steel with an identical CS_y to E' ratio normalized force curves are nearly identical.

Figure 78 presents the normalized horizontal reaction force versus normalized sliding distance for the materials in Table 11 for interferences of $6\omega_c$ and $15\omega_c$. As shown in the figure, the normalized force curves are nearly identical for identical-material sliding cases with the same CS_y to E' ratio. Similar results can be seen for the steel-on-steel and copper-on-copper sliding cases with the same CS_y to E' ratio at a $6\omega_c$.

However, it is found that the higher interference case of the steel-on-steel and aluminum-on-copper sliding with the same CS_y to E' ratio do not match.

Figure 79 presents the normalized vertical reaction force versus normalized sliding distance. Very similar results to the normalized vertical reaction force curves can be seen (sliding combinations with the same CS_y to E' ratio are nearly identical). Another interesting point is that regardless of the CS_y to E' ratio the maximum normalized vertical reaction force value is identical indicating that the critical load normalizes the maximum vertical reaction force well.

These results indicate that the normalization scheme presented here works when normalizing the vertical reaction forces for elastic-plastic sliding contact and that the normalized reaction forces in one material combination is representative of the normalized vertical reaction forces in any sliding contact situation of metallic materials.

Table 11: The material properties and critical values in this comparison.

	Al-Al	Stl-Stl (1)	Cu-Cu	Stl-Stl (2)	Al-Cu	Stl-Stl (3)
Pc [J]	1.15E+05	3.46E+05	3.95E+04	6.04E+04	6.73E+04	1.49E+05
E' [GPa]	38.55	111.4	72.9	111.4	50.44	111.4
C	1.645	1.637	1.65	1.637	1.645	1.637
Sy [MPa]	310	911.1	310	505	310	687.9
ω_c [m]	2.16E-04	2.21E-04	6.91E-05	6.91E-05	1.26E-04	1.26E-04
CSy/E'	1.3%	1.3%	0.7%	0.7%	1.0%	1.0%

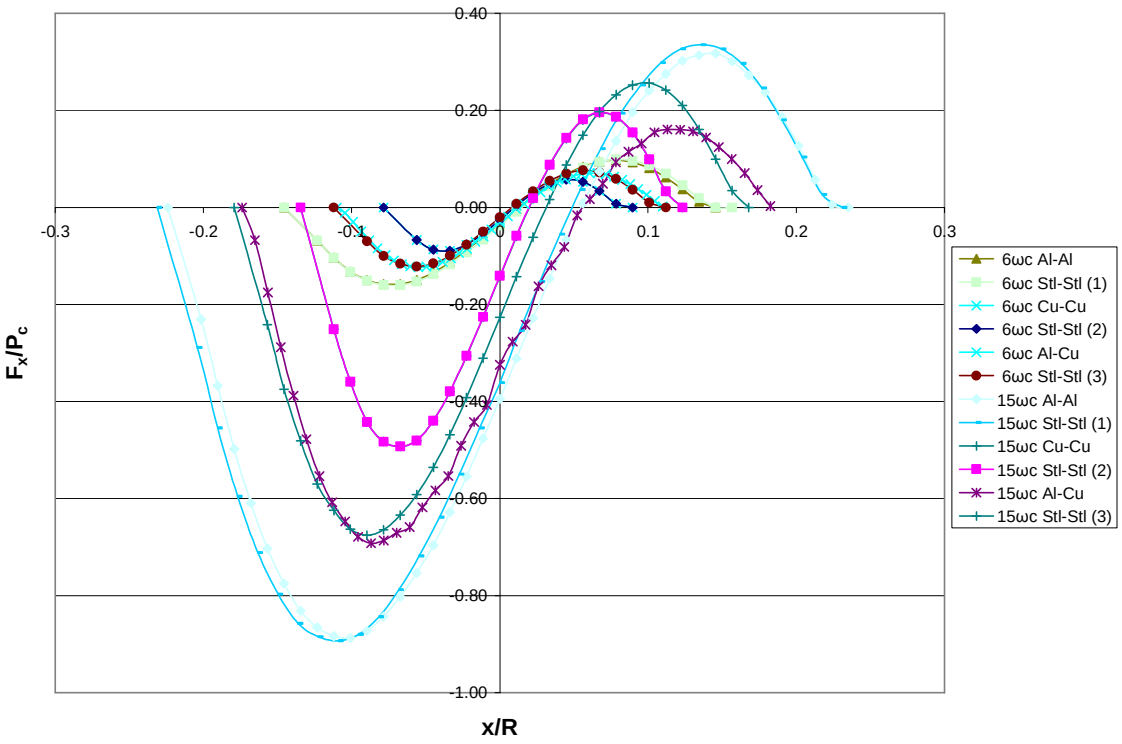

Figure 78: Normalized horizontal reaction force versus normalized sliding distance.

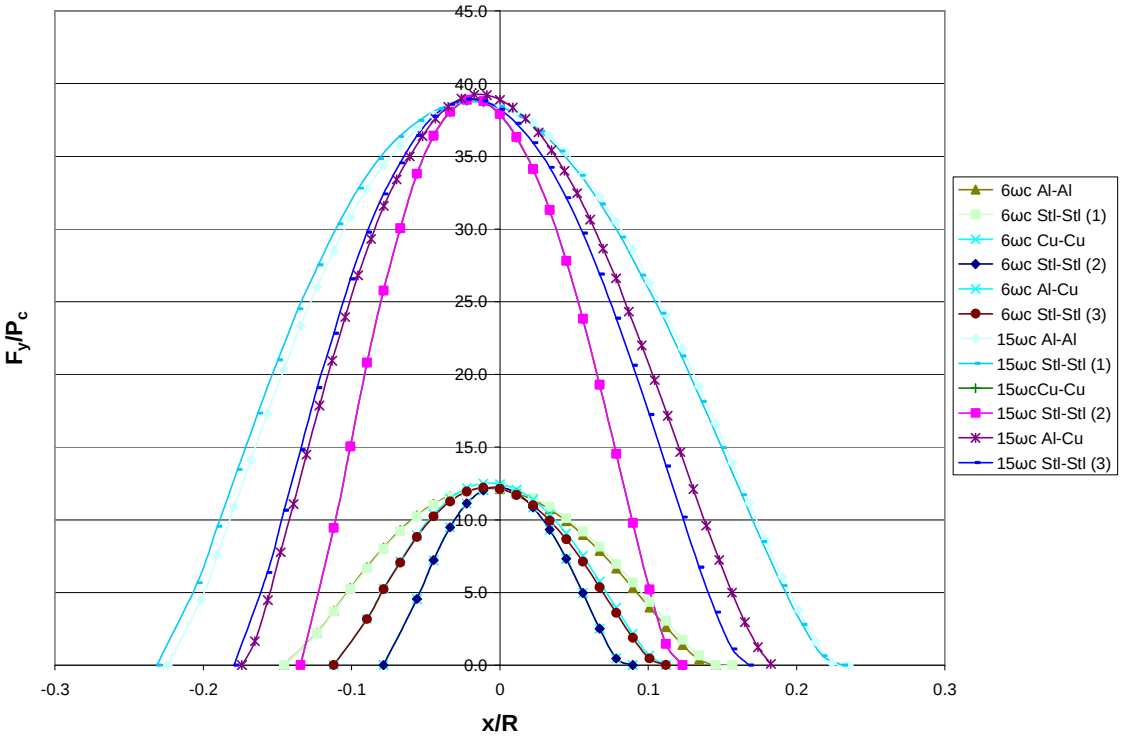

Figure 79: Normalized horizontal reaction force versus normalized sliding distance.

CHAPTER X: ELECTRICAL AND THERMAL ANALYSIS

10.1. Motivation

A specific application of sliding asperity contact, which the previously described FEA technique is well suited to model, is sliding electrical contacts. Sliding electrical contact occurs in many instances including brushed electrical motors, electrical switches and electromagnetic launchers, to name a few. An electromagnetic launcher (EML) is an apparatus that propels an armature along rails. This is accomplished by converting electric energy into kinetic energy. Figure 80 presents a schematic diagram of an EML.

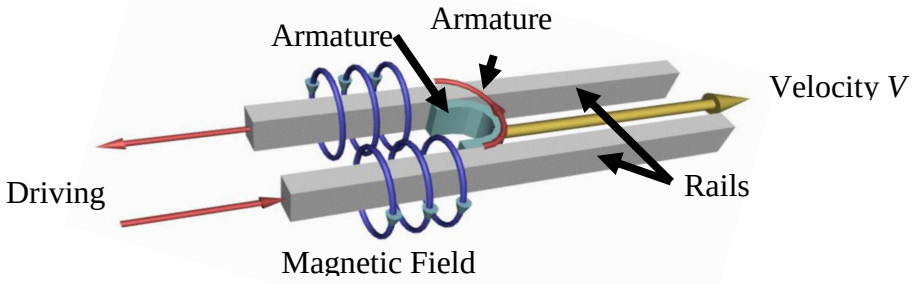

Figure 80: Schematic diagram of an EML (by Chester Petry, NAVSEA Dahlgren, NDIA 5th Annual System Engrg Conf., 2002)

An EML consists of two parallel metal rails that are connected to an electrical power supply and an electrically conductive armature. An electrically conductive armature is placed between the rails and a closed circuit is formed. A voltage difference is applied by a power supply to the rails and electric current flows from the power supply, into one rail, through the armature, through the other rail, and back to the power supply. The flow of current produces a magnetic field. An applied current, coupled with the

resulting magnetic field, creates an electromagnetic force called the Lorentz force. This is the driving force which propels the armature. The Lorentz force, which is the force exerted on a charged particle in an electromagnetic field, is given by:

$$F = q\left(E + v \times B\right) \tag{22}$$

where F is the force, E is the electric field, B is the magnetic field, q is the electric charge of the particle, and v is the instantaneous velocity of the particle.

As is the case for any engineering surface, the armature and rails have some surface roughness. As such, asperity-to-asperity contact occurs and deformation results as the armature slides across the rail in the EML. Electromagnetic forces and thermal strains will affect the mechanical deformation taking place as the armature slides. To better understand the physics taking place, an asperity contact model coupling structural, electromagnetic, and thermal effects is necessary.

10.2. Approach and Assumptions

The 3D hemispherical structural model previously presented is the foundation for the coupled model. All the structural assumptions, normalizations, and boundary conditions still apply. Additionally, thermal and electromagnetic boundary conditions must be considered and it should be noted that the air volume surrounding the hemispheres must be modeled in order to correctly predict the magnetic field surrounding the asperities. The thermal and electromagnetic boundary conditions and simplifications are as follows:

- A voltage difference is applied between the top and bottom surfaces of the top and bottom asperities, respectively

- Convection occurs along the curved portions of the asperities
- No heat flux is allowed normal to the plane of symmetry
- Electrical and thermal contact resistance are not considered (perfect contact) on the asperity-to-asperity level
- No temperature dependence of any of the material properties

Figure 81 presents a schematic of the coupled model showing the thermal and electrical boundary conditions.

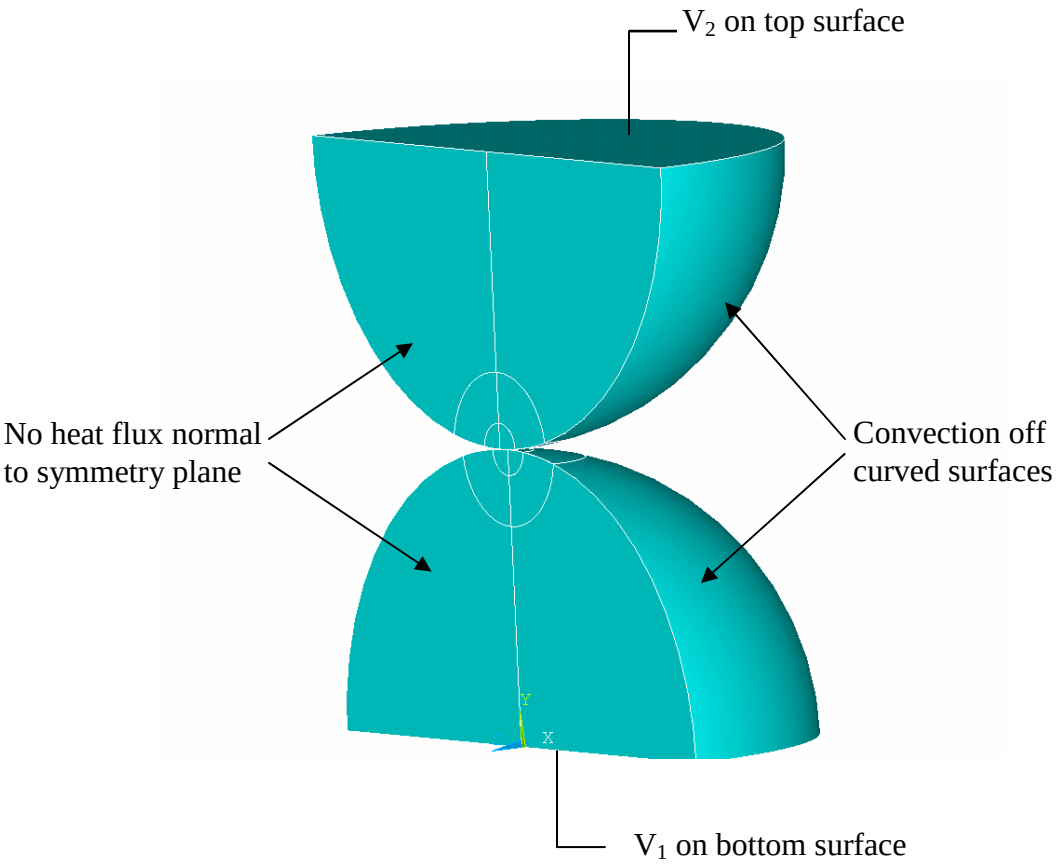

Figure 81: A schematic of the coupled model showing thermal and electrical boundary conditions.

10.3. Preliminary Results

A basic coupled model developed in ANSYS using Solid98 elements yields promising results for the technique outlined in 10.2. The results and trends seen are qualitatively what one would expect in an electrical contact model. However, a mesh convergence study has not been undertaken and these results have not been validated to theory. It is obvious in fact, by looking at the jagged stress contours, that the mesh should be refined to produce more reliable values.

The results discussed in this section are for frictionless aluminum-on-copper contact with an interference of $4\omega_c$. Table 10 presents the electrical and thermal boundary conditions used in this analysis.

Table 12: The electrical and thermal boundary conditions for the discussed results.

Parameter	**Value**
Convection Coefficient	10 W/m2-K
Voltage Difference	20 V
Temperature of Surroundings	20 °C
Initial Temperature of Hemispheres	50 °C

Figure 82 presents the von Mises stress at the point of vertical alignment. As shown in the figure, the maximum von Mises stress at the point of vertical alignment is 1.04 GPa. It is expected that the stress values should increase due to thermal strains induced by Joule heating. This maximum stress value for the coupled model is 315%

greater than the results presented for a structural-only model under the same interference at the point of vertical alignment. It should be noted that both the coupled model and the structural-only model use a material model with 2% strain hardening based on the yield strength. The stress pattern in Figure 82 as well as increased value of the von Mises stress due to thermal strain suggests the method followed in the coupled analysis is correct but should be refined to produce accurate results.

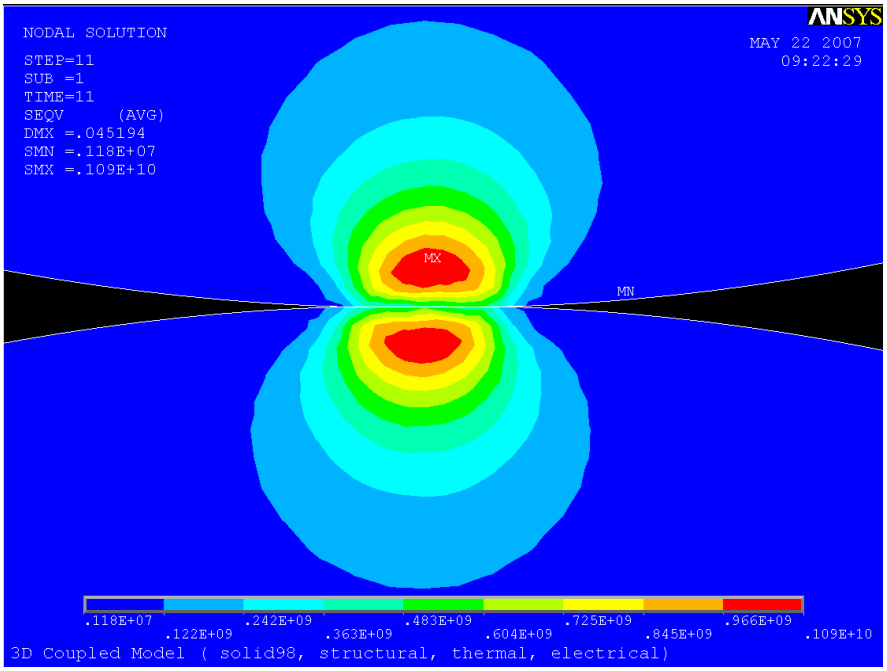

Figure 82: Von Mises stress for aluminum-on-copper contact with an interference of $4\omega_c$ at the point of vertical alignment.

Figure 83 presents the vector sum thermal gradient at the point of vertical alignment for aluminum-on-copper contact with an interference of $4\omega_c$. This is the vector sum of the temperature change in each direction. As shown in the figure, the copper displays the highest gradient which occurs at the contact interface. This is expected as

the material model used for copper has a thermal conductivity of 385 W/m-K versus 210 W/m-K for the material model for aluminum. The convection off the curved surfaces of the hemispheres and the thermal gradients such that the temperature in this analysis has reduced to 42 °C by the first load step and decrease thereafter. By the end of sliding, the temperature has reduced to 22 °C and immediately to 20 °C (the temperature of the surroundings) on the first load step after contact is completed.

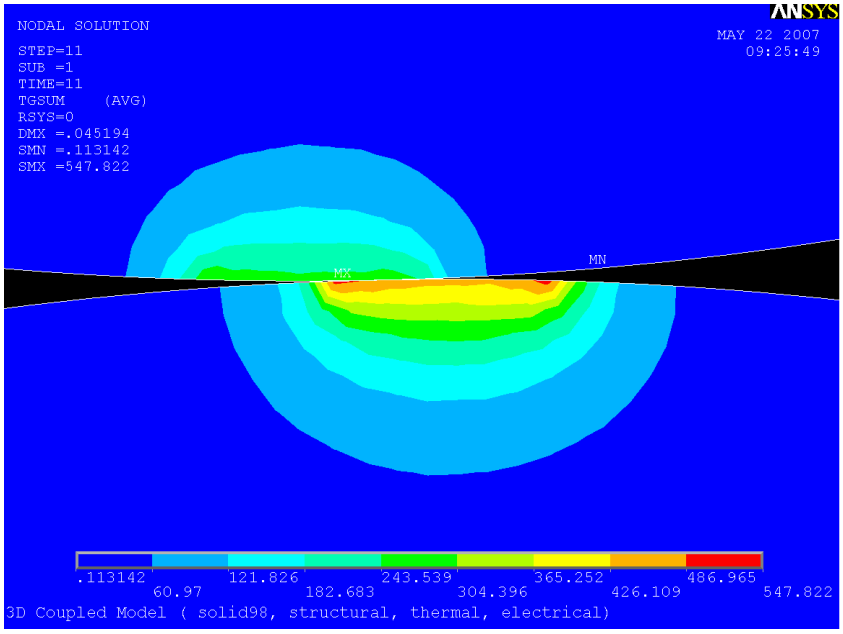

Figure 83: Thermal gradient in aluminum-on-copper contact with an interference of $4\omega_c$.

Figure 84 presents the vector sum of the current density near the contact area for aluminum-on-copper contact with an interference of $4\omega_c$ at the point of vertical alignment. The current is flowing from the aluminum hemisphere, with a voltage of 12V on its top surface, through the contact interface, and into the copper hemisphere. The flow of current is nearly symmetric and highest at the contact interface. The current density is given by:

$$\vec{J} = nq\vec{v_d} \tag{23}$$

where J is the current density, n is the particle density, and q is the charge density, and v_d is the particle drift velocity. Qualitatively, the current density as shown in Figure 73 is correct if one considers that the particle density will be greatest where there is the most compression (near the contact interface in this case) and the cross sectional area through which the current flows will be smallest at the contact interface.

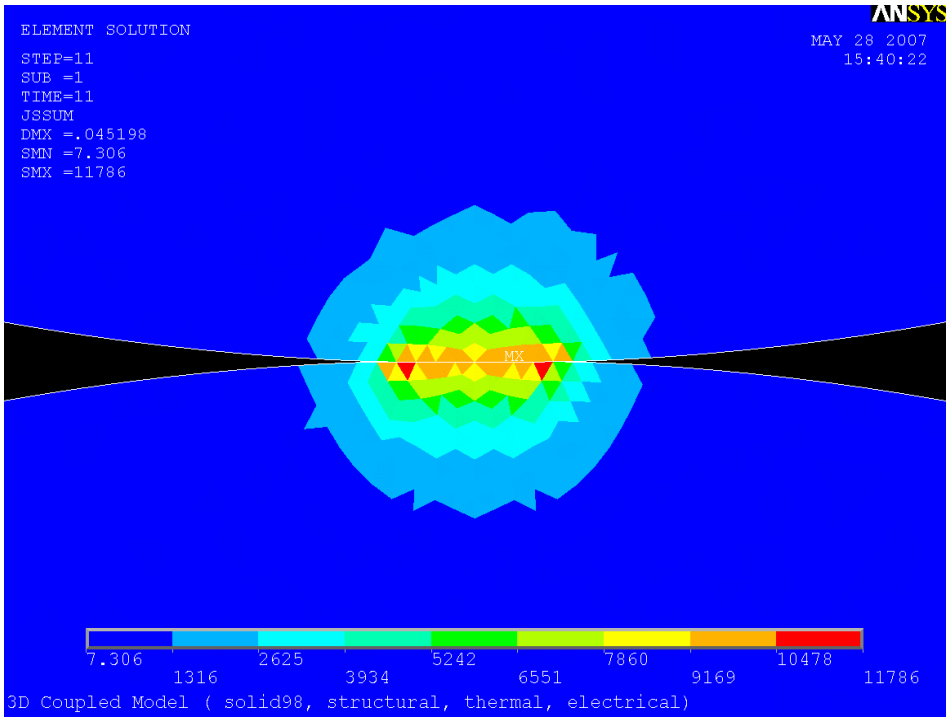

Figure 84: The vector sum of the current density aluminum-on-copper contact with an interference of $4\omega_c$.

10.4. Conclusions

A technique is introduced to perform an FEA on sliding elastic-plastic asperity contact coupling structural, electromagnetic and thermal loads. Sliding electrical contact occurs in many instances including electrical motors, electrical switches, and EMLs. Model assumptions and boundary conditions are introduced. Preliminary results are presented including von Mises stress, thermal gradients, and current density that qualitatively describe the physical phenomenon. These results are presented only to display confidence in the modeling technique, not for actual numerical values as a mesh convergence and validation study remains a task for future work.

Future work with the coupled model should include:

- Temperature dependent material properties
- Meshing the airspace surrounding the asperities in order to account for the magnetic field interaction between particle and surroundings
- Mesh refinement and convergence

CHAPTER XI: CONCLUSIONS AND FUTURE WORK

A method to model, via an FEA, frictionless and frictional sliding elastic-plastic hemispherical contact is discussed. Results are presented for both frictional and frictionless sliding between two steel hemispheres and between an aluminum and a copper hemisphere. The resultant parameters such as deformations, forces, stresses, and energy losses that occur are presented and explained. All the results are presented nondimensionally in order to apply to hemispherical contact at any scale. The development and propagation of stress in the hemispheres as sliding progresses is discussed. It is found that as the interference increases, the stresses in the hemispheres expand and reach the surface at values above the yield strength due to the addition of strain hardening to the material model. The reaction forces required to maintain straight line contact are investigated. A single set of equations is derived to characterize the energy loss due to plastic deformation for both material combinations because the magnitudes of the net energy at the end of sliding are similar. An effective coefficient of friction is introduced in order to help quantify plasticity. This effective coefficient of friction increases faster in steel-on-steel sliding than in aluminum-on-copper sliding. Equations to characterize residual deformations in steel-on-steel contact and aluminum-on-copper contact are derived. It is shown that aluminum shows more deformation than copper throughout the progression of sliding. Contact areas during sliding are presented and it is also found that the normalized dimensions of the contact region are larger in aluminum-on-copper contact.

Comparisons between frictional and frictionless sliding are drawn. The von Mises stresses seen in frictional sliding are higher in magnitude and distributed in a larger

volume than in the frictionless sliding cases. Also, the stress pattern in the frictional sliding cases is symmetric about a line angled in a direction that opposes sliding while in frictionless sliding, the stress pattern is symmetric about the vertical. Frictional contact displays residual stresses lower than in frictionless contact. Forces and contact areas are larger in magnitude for frictional sliding and the horizontal reaction force is completely negative in frictional sliding, while it becomes positive as the hemispheres separate in frictionless sliding. As friction is non-conservative, the energy loss in frictional sliding is much greater than in frictionless sliding. However, the effective coefficient of friction is similar in magnitude for both frictional and frictionless sliding for the cases studied. In steel-on-steel contact, both the residual and maximum deformations seen during sliding are larger for frictional sliding than frictionless sliding. Similarly, in aluminum-on-copper sliding the aluminum results in a larger maximum and residual deformation for frictional sliding compared to frictionless sliding. However, copper shows a smaller maximum deformation and a larger residual deformation for frictional sliding when compared to frictionless sliding.

The results from the FEA are compared to a novel semi-analytical technique (SAM). The SAM and FEA results are nearly identical for frictionless steel-on-steel contact and similar for frictionless aluminum-on-copper contact. There is a slight divergence as preset interference increases for aluminum-on-copper sliding due to the fact that the SAM can only model one body as elastic-plastic with dissimilar materials. The SAM cannot model frictional contact presently. Overall, the SAM helps to validate the FEA results and can be used to adequately model sliding contact situations with drastically reduced run times.

Comparisons between different amounts of strain hardening are drawn in this chapter for a frictional steel-on-steel contact situation with an interference of $12\omega_c$ and a frictionless aluminum-on-copper contact situation with an interference of $15\omega_c$. The magnitudes of the von Mises stress increase with increasing strain hardening. Forces are larger with more strain hardening. The net energy loss is lower with more strain hardening for frictionless sliding because the plastically deformed material will impose more of a rebound (positive) force as the hemispheres are separating. However, in frictional sliding this effect is masked by the increase in shear traction opposing sliding resulting from the imposed coefficient of friction. In steel-on-steel contact both the residual and maximum deformations seen during sliding decrease with increasing strain hardening. Similarly, in aluminum-on-copper sliding the aluminum material has smaller maximum and residual deformations for larger values of strain hardening. On the other hand, copper shows slightly more deformation throughout sliding with increasing strain hardening but slightly less residual deformation.

A technique is introduced to perform an FEA on sliding elastic-plastic asperity contact coupling structural, electromagnetic and thermal loads. Sliding electrical contact occurs in many instances including electrical motors, electrical switches, and EMLs. Model assumptions and boundary conditions are introduced. Preliminary results are presented including von Mises stress, thermal gradients, and current density that qualitatively describe the physical phenomenon. These results are presented only to display confidence in the modeling technique, not for actual numerical values as a mesh convergence and validation study has not been completed.

Future work should include a mesh convergence study of the coupled model to validate the results. Temperature dependent material properties should be implemented and the surrounding air should be meshed in order to account for the material-surroundings magnetic field interaction. A parametric study should be done in order to investigate how the vertical interference influences the parameters of interest (stresses, deformations, contact areas, etc.). Also, as sliding contact of a pair of asperities constitutes the kernel of the solution for a stochastically described rough surface. As such, it should be investigated how to apply the solution of a single pair of asperities to a real rough surface. Another interesting phenomenon that should be investigated is multiple pass sliding to investigate how the residual stresses and strains will affect the results for another pass.

REFERENCES

1. Liu, G., Q.J. Wang, and C. Lin, *A Survey of Current Models for Simulating the Contact between Rough Surfaces.* Tribology Transactions, 1999. **42**: p. 581-591.

2. Thomas, T.R., *Rough Surfaces.* 1982.

3. Greenwood, J.A., *A unified Theory of Surface Roughness.* Proceedings of the Royal Society of London, A, 1984. **393**: p. 133-157.

4. Greenwood, J.A. and J.B.P. Williamson, *Contact of Nominally Flat Surfaces.* Proceedings of the Royal Society of London. Series A, Mathematical and Physical Sciences, 1966. **295**(1442): p. 300-319.

5. Bush, A.W., R.D. Gibson, and T.R. Thomas, *The Elastic Contact of Rough Surfaces.* Wear, 1975. **35**: p. 87-111.

6. Greenwood, J.A. and J.H. Tripp, *The Elastic Contact of Rough Spheres.* ASME Journal of Applied Mechanics, 1967. **34**: p. 153-159.

7. Lo, C.C., *Elastic Contact of Rough Cylinders.* Int. J. Mech. Sci., 1969. **11**: p. 105-115.

8. Tsukizoe, T. and T. Hisakado, *On the Mechanism of Contact between Metal Surfaces: Part 2 - The Real Area and the Number of Contact points.* ASME Journal of Lubrication Tribology, 1968. **F90**: p. 81-90.

9. Whitehouse, D.J. and J.F. Archard, *The Properties of Random Surface of Significance in their Contact.* Proceedings of the Royal Society of London, A316, 1970: p. 97-121.

10. Abbot, E.J. and F.A. Firestone, *Specifying Surface Quality - A Method Based on Accurate Measurement and Comparison.* Mechanical Engineering, 1933. **55**: p. 569.

11. Evseev, D.G., B.M. Medvedev, and G.G. Grigoriyan, *Modification of the Elastic-Plastic Model for the Contact of Rough Surfaces.* Wear, 1991. **150**: p. 79-88.

12. Chang, W.R., *An Elastic-Plastic Contact Model for a Rough Surface with an Ion-Plated Soft metallic Coating.* Wear, 1997. **212**: p. 229-237.

13. Zhao, Y.W., *An Asperity Microcontact Model Incorporating the Transition from Elastic Deformation to Full Plastic Flow.* ASME Journal of Tribology, 2000. **122**: p. 86-93.

14. Vu-Quoc, L., X. Zhang, and L. Lesburg, *A Normal Force-Displacement Model for Contacting Spheres Accounting for Plastic Deformation: Force-Driven Formulation.* ASME Journal of Applied Mechanics, 2000. **67**: p. 363-371.

15. Nosonovsky, M. and G.G. Adams, *Steady-state frictional sliding of two elastic bodies with a wavy contact interface.* Journal of Tribology, Transactions of the ASME, 2000. **122**(3): p. 490.

16. Jackson, R., I. Chusoipin, and I. Green, *A Finite Element Study of the Residual Stress and Deformation in Hemispherical Contacts.* Journal of Tribology, 2005. **127**(3): p. 484.

17. Wang, F. and L.M. Keer, *Numerical simulation for three dimensional elastic-plastic contact with hardening behavior*. Journal of Tribology, 2005. **127**(3): p. 494.

18. Nelias, D., V. Boucly, and M. Brunet, *Elastic-plastic contact between rough surfaces: Proposal for a wear or running-in model.* Journal of Tribology, 2005. **127**(3): p. 494.

19. Green, A.P., *The plastic yielding of metal junctions due to combined shear and pressure.* Journal of Mechanics and Physical Solids, 1954. **2**: p. 197-211.

20. Green, A.P., *Friction between unlubricated metals: a theoretical analysis of the junction medel.* Proceedings of the Royal Society, 1955: p. 191-204.

21. Faulkner, A. and R.D. Arnell, *The development of a finite element model to simulate the sliding interaction between two, three-dimensional, elastoplastic, hemispherical asperities.* Wear, 2000. **242**(1-2): p. 114.

22. Boucly, V., D. Nelias, and I. Green, *Modeling of the Rolling and Sliding contact Between Two Asperities.* In Print, Journal of Tribology, 2007. **Vo. 129**.

23. Johnson, K.L., *Contact Mechanics*. 1985: Cambridge University Press.

24. Green, I., *Poisson Ratio Effects and Critical Values in Spherical and Cylindrical Hertzian Contacts.* International Journal of Applied Mechanics, 2005. **10**(3): p. 451-462.

25. Jackson, R.L. and I. Green. *A finite element study of elasto-plastic hemispherical contact*. 2003. Ponte Vedra Beach, FL, United States: American Society of Mechanical Engineers, New York, NY 10016-5990, United States.

26. Vijaywargiya, R. and I. Green, *A Finite Element Study of the Deformations, Forces, Stress Formations, and Energy Losses in Sliding Cylindrical Contacts.* International Journal of Non-Linear Mechanics, 2007.

27. Jackson, R.L. and I. Green, *A Finite Element Study of Elasto-Plastic Hemispherical Contact Against a Rigid Flat.* Journal of Tribology, 2005. **127**: p. 343-354.